SEMICLASSICAL APPROACHES TO COMPLEX CHEMICAL SIMULATION IN REAL TIME

A Dissertation

Presented to the Faculty of the Graduate School

of Cornell University

in Partial Fulfillment of the Requirements for the Degree of

Doctor of Philosophy

by

Matthew Steven Church

May 2019

SEMICLASSICAL APPROACHES TO COMPLEX CHEMICAL SIMULATION IN REAL TIME

Matthew Steven Church, Ph.D.

Cornell University 2019

Semiclassical (SC) theory offers a pedagogically rich connection between quantum and classical perspectives of nature, and, furthermore, is a promising approach to incorporating quantum effects into molecular dynamics simulations. However, a variety of numerical challenges associated with SC methods, such as the cumbersome search for special trajectories, or the integration of highly oscillatory functions (i.e. the SC "sign problem"), generally renders SC theory impractical for all but very simple, low-dimensional systems. In this dissertation we derive a variety of mixed quantum-classical (MQC) representations of the real-time correlation function within the SC initial value representation (SC-IVR) using the modified Filinov filtration (MFF) technique. The most promising of these methods are subsequently tested on a number of low- and high-dimensional systems. Each of these methods have three significant advantages. (1) They offer a significant improvement upon the SC-IVR "sign problem." (2) They offer mode-specific quantization in a dynamically consistent framework. And (3) they are significantly easier to implement than other leading SC-IVR methodologies. The extension of these methods to nonadiabatic systems is made as well. We conclude that, in future studies of a variety of non-equilibrium molecular systems, particularly those that exhibit strong nuclear quantum effects such as interference, the novel SC-IVR methods presented here should prove to be very powerful.

BIOGRAPHICAL SKETCH

Matthew S. Church was raised in East Providence, Rhode Island, and discovered an interest in the natural world at an early age after reading works by the great popularizers of science such as Hawking and Kaku. As an undergraduate chemistry major at Hobart and William Smith Colleges in Geneva, New York, he was first introduced to computational chemistry when he joined Professor Alan van Giessen's research group to study theoretical biophysics, and later developed a profound interest in quantum theory after taking Chem 320 Physical Chemistry II under the same professor. After joining Professor Nandini Ananth's theoretical chemistry research group at Cornell University in 2014, his graduate work has entailed the development, optimization, and extension of novel semiclassical methods for the simulation of large-scale adiabatic and nonadiabatic chemical systems. In August 2019 he will join the research group of Professor Brenda Rubenstein at Brown University as a postdoctoral researcher.

To anyone who finds this useful.

ACKNOWLEDGEMENTS

If not for the brilliant and supportive people around me my CV would contain mostly whitespace. Professor Nandini Ananth has been a fantastic advisor; her success and expertise as a scientist has supplied me with endless motivation; her active interest in my own success has kept me afloat in challenging times; and her charming sense of humor never fails to spin a moment in a positive direction. The other members of my special committee, Professors Greg Ezra and Roger Loring, have also been a source of sage wisdom along this journey through graduate school.

Of my colleagues I am particularly grateful to have worked with, befriended, and/or made irresponsible decisions with Dr. Tim Hele and Dr. Sergey Antipov, Prashanth Ramesh, Dr. Rachel Kenion-Hanrath, Srinath Ranya, Dr. Jessica Duke, Elliot Eklund, Dr. Sadrach Pierre, Dr. Eric Fuemmeler, Dr. Britta Johnson, Shreyas Malpathak, and other members of the Ananth group.

TABLE OF CONTENTS

Biographical Sketch . . . iii
Dedication . . . iv
Acknowledgements . . . v
Table of Contents . . . vi
List of Tables . . . viii
List of Figures . . . ix

1 Introduction **1**
1.1 The Semiclassical Approach . . . 2
1.1.1 A Brief Survey of Early SC Theories . . . 3
1.1.2 From the Feynman Path Integral to the SC-IVR . . . 7
1.1.3 SC Correlation Functions . . . 15
1.1.4 Leading Approaches to the "Sign Problem" . . . 16
1.1.5 Modified Filinov Filtration . . . 18
1.2 Other Methods . . . 21
1.3 Thesis and Outline . . . 23

2 Variations of the Mixed Quantum-Classical IVR **26**
2.1 The Forward-Backward Implementation . . . 26
2.2 The Double-Forward Implementation . . . 31
2.3 Generalized MQC-IVR . . . 36
2.4 Numerical Tests . . . 37

3 Validating the MFF Approximation **48**

4 The Analytical MQC Limit **56**
4.1 Motivation and Derivation . . . 56
4.2 Separable Prefactor Approximation . . . 61
4.3 Numerical Tests . . . 63

5 Semiclassical Nonadiabatic Dynamics **76**
5.1 MM-ST Hamiltonian . . . 78
5.2 MInt Algorithm . . . 81
5.2.1 Evolution Flow Map . . . 81
5.2.2 Equations of Motion . . . 82
5.2.3 Monodromy Matrix Elements . . . 85
5.2.4 Step-by-step Algorithm . . . 87
5.2.5 Other Properties . . . 88
5.2.6 Numerical Performance . . . 89
5.3 Nonadiabatic Dynamics with MQC-IVR . . . 95

6 The SC Corr-Code Package **104**
6.1 Introduction 104
6.2 Generating and Running a Simulation 106

7 Ongoing Projects and Concluding Remarks **109**
7.1 Nonadiabatic Energy Transfer at Metal Surfaces 109
7.1.1 The Model 110
7.1.2 Numerical Tests 111
7.2 Zero-Point Energy Leakage in MQC-IVR Methods 118
7.2.1 The Model 119
7.2.2 Numerical Tests 120
7.3 General Conclusions 123

A FB MQC-IVR Prefactors **125**
A.1 Simplification of the FB MQC-IVR Prefactor 125
A.2 FB MQC-IVR with Reduced Dimensionality 129

B Simplification of the MQC-IVR Prefactor **134**

C Numerical Parameters for NO/Au System **138**

Bibliography **139**

LIST OF TABLES

2.1 A comparison of CPU time to calculate the MQC-IVR position correlation function with the DF and FB implementations and $c = c_p = c_q = 0.7$. 40

2.2 The number of trajectory pairs ($\times 10^{-3}$) required to converge an MQC-IVR simulation of model 1 in time $t = 55$ as a function of c_p and c_q tuning parameters. 42

2.3 The number of trajectory pairs required for convergence ($\times 10^{-5}$) of $\langle \hat{x} \rangle_t$ under each filtering parameter regime depicted in the previous three figures. Note that $c_x = c_{p_x} = c_{q_x}$ and $c_y = c_{p_y} = c_{q_y}$. . . . 46

4.1 The time-averaged (relative) % error of each AMQC-IVR result. The result in parentheses was obtained after quantizing both the anharmonic and harmonic dofs. 69

4.2 The time-averaged (relative) % error of each AMQC-IVR result with the SP approximation. 69

5.1 The initial phase space points of the test trajectory. 91

5.2 The approximate number of trajectories needed for graphical convergence of the MQC-IVR results appearing in Fig. 5.4(b), where the nuclear and electronic dofs are treated with the same value of tuning parameter. 98

5.3 The approximate number of trajectories needed for graphical convergence of the MQC-IVR results appearing in Fig. 5.4(c), where the nuclear tuning parameter is fixed near the quantum limit, $c_N = 0.01$, and the tuning parameter associated with the mapping variables are varied. 99

5.4 The approximate number of trajectories needed for graphical convergence of the MQC-IVR results appearing in Fig. 5.4(d), where the tuning parameter associated with the mapping variable is fixed near the quantum limit, $c_e = 0.01$, and the tuning parameter associated with the nuclear dof is varied. 100

C.1 Numerical parameters for NO/Au system. 138

LIST OF FIGURES

1.1 The Feynman real time path integral is a continuous sum of phase factors associated with the infinite set of paths (black curves), including classical trajectories (red curves, if they exist), connecting coordinates $\mathbf{q}_0$ and $\mathbf{q}_t$ in time t. 9

1.2 Within the stationary phase approximation to the Feynman path integral, the continuous sum over all paths connecting $\mathbf{q}_0$ and $\mathbf{q}_t$ in time t reduces to a discrete sum over classical trajectories (red curves). A complex prefactor accounts for small fluctuations (black curves) around the classical trajectories. This approximation is exact in the limit that $\hbar \to 0$. 11

1.3 Two trajectories of the 1D harmonic oscillator with spring constant $k = 1$ and initial coordinate $q(0) = 0$. The initial momenta are $p(0) = 2$ (black), $p(0) = -4$ (dashed). We also plot the (a) inverse of $M_{qp}(t)$ (red) associated with the first trajectory as well as $M_{qp}(t)$ (red) in panel (b). 13

2.1 Diagrams showing the implementation strategy of (a) FB MQC-IVR and (b) MQC-IVR. In the former case, one must manually sample the phase space displacements between forward and backward trajectories at all times. In the latter case one simply propagates two forward-moving trajectories independently: a much more efficient approach. 32

2.2 The average position of the anharmonic oscillator as a function of time, as computed with MQC-IVR and $c = c_p = c_q = 0.7$ (red), 1.0 (cyan), 3.0 (orange), 5.0 (blue), 10.0 (green), and 100.0 (purple). Husimi-IVR (yellow) is hidden behind the purple MQC-IVR result. The exact quantum result (black, dashed) is included as well. 39

2.3 The average position of the anharmonic oscillator as a function of time, as computed with MQC-IVR. Different combinations of c_p and c_q are used in each case. Within each panel c_q is held fixed, as indicated in the label. The value of c_p is determined by the color of each curve: $c_p = 0.7$ (red), 1.0 (cyan), 3.0 (orange), 5.0 (blue), 10.0 (green), and 100.0 (purple). 41

2.4 The expectation value of (a) $\langle \hat{x} \rangle_t$ and (b) $\langle \hat{y} \rangle_t$ as a function of time as computed with exact quantum (black, dashed) and MQC-IVR with all tuning parameters set to the same value $c = c_{p_x} = c_{q_x} = c_{p_y} = c_{q_y}$: $c = 0.1$ (blue), $c = 0.7$ (red), $c = 1.0$ (orange), $c = 3.0$ (yellow), $c = 5.0$ (cyan), $c = 10.0$ (magenta), $c = 50.0$ (green), and $c = 100.0$ (purple). The Husimi-IVR result (gold) is beneath the classical limit MQC-IVR result. 43

2.5 The expectation value of (a) $\langle \hat{x} \rangle_t$ and (b) $\langle \hat{y} \rangle_t$ as a function of time as computed with exact quantum (black, dashed) and MQC-IVR with the anharmonic mode fixed near the quantum limit, $c_{p_x} = c_{q_x} = 0.1$, and the harmonic mode treated with different values of $c = c_{p_y} = c_{q_y}$: $c = 0.1$ (blue), $c = 0.7$ (red), $c = 1.0$ (orange), $c = 3.0$ (yellow), $c = 5.0$ (cyan), $c = 10.0$ (magenta), $c = 50.0$ (green), and $c = 100.0$ (purple). The Husimi-IVR result (gold) is beneath the classical limit MQC-IVR result. 44

2.6 The expectation value of (a) $\langle \hat{x} \rangle_t$ and (b) $\langle \hat{y} \rangle_t$ as a function of time as computed with exact quantum (black, dashed) and MQC-IVR with the harmonic mode fixed near the quantum limit, $c_{p_y} = c_{q_y} = 0.1$, and the anharmonic mode treated with different values of $c = c_{p_x} = c_{q_x}$: $c = 0.1$ (blue), $c = 0.7$ (red), $c = 1.0$ (orange), $c = 3.0$ (yellow), $c = 5.0$ (cyan), $c = 10.0$ (magenta), $c = 50.0$ (green), and $c = 100.0$ (purple). The Husimi-IVR result (gold) is beneath the classical limit MQC-IVR result. 45

3.1 The (a) phase and (b) amplitude of the HK-IVR wavepacket integrand as a function of the trajectories' initial position q_0 with fixed $p_0 = 0.0$. Also plotted is the (c) phase and (d) amplitude of the integrand as a function of the trajectories' initial momentum p_0 with fixed $q_0 = 1.0$. In each case we fix the wavepacket position $x = 0.5$ and time $t = 7.5$. 49

3.2 The phase and amplitude of the FB MQC-IVR integrand as a function of the momentum displacement between trajectory pairs at time (a-b) $t = 22$ and (c-d) $t = 61$. The color of each curve corresponds to a different choice of tuning parameter c_p, which varies from $c_p = 10^{-4}$ (purple) to $c_p = 200.0$ (red). The black vertical gridlines enclose the least oscillatory region of the integrand. 52

3.3 The (a) phase and (b) amplitude of the MQC-IVR position correlation function against the momentum displacement between forward-backward trajectories at $t = 22$ a.u. in the quantum limit, as averaged over 1.2×10^3 trajectories (gray), 6.0×10^4 trajectories (red), and 2.4×10^5 trajectories (blue). The black-dashed Gaussian represents a weak filter strength ($c_p = 0.05$) while the green-dashed Gaussian represents an optimal filter strength ($c_p = 0.7$). 54

4.1 The average position of the anharmonic mode in model 1 as a function of time, as computed with exact quantum (black, dashed), Husimi-IVR (black), AMQC-IVR with one quantized mode (blue), AMQC-IVR with one quantized mode under the separable prefactor approximation (red), and AMQC-IVR with two quantized modes (green). Each panel corresponds to a different coupling strength: (a) $k = 0.5$, (b) $k = 1.5$, and (c) $k = 2.0$. The inset in (c) amplifies the correlation function from $t = 55$ to $t = 80$. 68
4.2 The average position of the anharmonic mode in model 2 as computed with AMQC-IVR (blue) and Husimi-IVR (red) with a reduced coupling strength of (a) $\eta/m\omega_1 = 0.001$, (b) $\eta/m\omega_1 = 0.01$, and (c) $\eta/m\omega_1 = 1.0$. The exact quantum result (black, dashed) of the 1D anharmonic oscillator in the absence of coupling to the bath is shown as well. Panel (a) also contains the AMQC-IVR result with the SP approximation (green). 71
4.3 The AMQC-IVR (red) thermal transmission coefficient of model 3 at $T = 300K$ as a function of the reduced coupling strength. Exact path integral results (black) are obtained from a previous study [126]. 73
4.4 The thermal transmission coefficient of model 3 at $T = 300K$ as a function of time, with $\eta/m\omega_b = 0.05$, as computed with AMQC-IVR (black) and with AMQC-IVR with the SP approximation (red). 74

5.1 Elements of the diabatic electronic potential energy matrix are plotted as a function of the nuclear coordinate: $V_{11}(R)$ (black), $V_{22}(R)$ (gray), and $V_{12}(R) = V_{21}(R)$ (red). 90
5.2 A comparison of how (a) the Mint algorithm and (b) the Adams propagator conserves energy along a single trajectory. Each curve corresponds to a different timestep Δt used during the simulation: 0.75 (purple), 1.5 (green), 3.0 (red), and 6.0 (blue). 91
5.3 A comparison of how (a) the MInt algorithm and (b) the Adams propagator conserves the symplecticity criterion δM along a single trajectory. Each curve corresponds to a different timestep Δt used during the simulation: 0.75 (purple), 1.5 (green), 3.0 (red), and 6.0 (blue). 94

5.4 Panel (a) plots the diabatic surfaces and coupling of the model system. Panels (b)-(d) plot the nuclear momentum distribution obtained with exact quantum (black) and MQC-IVR with different sets of tuning parameters. In panel (b) we vary $c_N = c_e$, in (c) we fix $c_N = 0.01$ and vary c_e, and in (d) we fix $c_e = 0.01$ and vary c_N. Each color corresponds to a different value of the varied tuning parameter: 0.01 (red), 0.05 (green), 0.1 (blue), 0.5 (purple), 1.0 (orange), 10.0 (cyan), 100.0 (pink). Panel (b) also contains the Husimi-IVR result (black, dashed). 97
5.5 The populations of both electronic states, as computed with MQC-IVR, are plotted as a function of time. Results in panel (a) are obtained with varied $c_N = c_e$, panel (b) with $c_e = 0.01$ and varied c_N, and panel (c) with $c_N = 0.01$ and varied c_e. Each color corresponds to a different value of the varied tuning parameter: 0.01 (red), 0.05 (purple), 0.1 (yellow), 0.5 (orange), 1.0 (green), 10.0 (blue), and 100.0 (pink). The Husimi-IVR result in panel (a) rests behind the pink curve associated with $c_N = c_e = 100.0$. The exact quantum result (black) is directly beneath the quantum limit MQC-IVR results. 101

7.1 The LSC-IVR results of the (a) survival amplitude of the initial vibrational eigenstate, (b) the average NO bond length, (c) the average NO-metal distance, and (d) the electronic state populations. Each color corresponds to a different initial vibrational eigenstate: $n = 0$ (black), $n = 3$ (red), and $n = 15$ (blue). 114
7.2 The LSC-IVR results of the (a) survival amplitude of the initial vibrational eigenstate, (b) the average NO bond length, (c) the average NO-metal distance, and (d) the electronic state populations. Each color corresponds to a different initial vibrational eigenstate: $n = 0$ (black), $n = 3$ (red), and $n = 15$ (blue). 115
7.3 The Husimi-IVR results of the (a) survival amplitude of the initial vibrational eigenstate, (b) the average NO bond length, (c) the average NO-metal distance, and (d) the electronic state populations. Each color corresponds to a different initial vibrational eigenstate: $n = 0$ (black), $n = 3$ (red), and $n = 15$ (blue). 116
7.4 The Husimi-IVR results of the (a) survival amplitude of the initial vibrational eigenstate, (b) the average NO bond length, (c) the average NO-metal distance, and (d) the electronic state populations. Each color corresponds to a different initial vibrational eigenstate: $n = 0$ (black), $n = 3$ (red), and $n = 15$ (blue). 117

7.5 The extent of energy drift δE_{jt} as a function of time in the high frequency mode (black) and the low frequency mode (red). Each panel contains MQC-IVR results with small tuning parameters $c_{high} = c_{low} = 10^{-5}$ (solid, thick) and Husimi-IVR results (solid, thin). Panel (a) also contains MQC-IVR results with large tuning parameters $c_{high} = c_{low} = 10^{5}$ (dashed). Panel (b) also contains MQC-IVR results with a quantized low frequency mode $c_{low} = 10^{-5}$ and a classical high frequency mode $c_{high} = 10^{5}$ (long, dashed), as well as the reverse (short, dashed). Panel (c) contains the AMQC-IVR result after quantizing only low frequency mode (long, dashed), and after only quantizing the high frequency mode (short, dashed). 122

CHAPTER 1

INTRODUCTION

In order to fully understand a great number of important dynamical processes on the molecular scale, such as in charge and/or energy transfer events and renewable energy capture in chemical and biological systems, we often require a quantum mechanical description of nature [1–12]. This is because, when considering the motion of light masses on the molecular level, the uncertainty relations of quantum theory [13] are imperative, and give rise to the wave-like nature of matter entailing phenomena like tunneling, zero-point energy, and interference, which so seemingly contradict our mundane "classical" experience of the macroscopic world.

An exact quantum mechanical description of a given problem is, however, generally impossible to discern for all but the most trivial systems, and the exponential scaling of a given basis set generally restricts accurate numerical methods to the study of systems with merely a few degrees of freedom (dofs). On the other hand, classical molecular dynamics [14] (MD) has been very successful over the past several decades in simulating very large chemical systems (with as many as 10^7 dofs, for example), but MD methods strictly rely on the classical equations of motion, and therefore necessarily fail whenever quantum mechanical effects play an important role in the dynamics.

For example, one very important scenario in which classical MD methods will surely fail is in the description of the vibrations of a water molecule. At room temperature the amount of zero-point energy stored in the three vibrational modes of a water molecule is roughly $20 \times k_B T$. Since classical MD does not include zero-point energy, a classical simulation of a collection of wa-

ter molecules at room temperature will therefore result in the leakage of vibrational zero-point energy into other modes of motion, causing the system to quickly boil over [15,16]. In certain cases this problem can be avoided, for example, by making a rigid-bond approximation in circumstances where the water molecules serve as a passive solvent, but an accurate description of processes that involve, say, the formation and breaking of OH bonds will certainly require a quantum mechanical description of those vibrations [15].

It is the concern of this dissertation to combine the advantages of the two aforementioned theories into a uniform, dynamically consistent methodology. That is, we wish to exploit the computational efficiency of doing classical MD on highly multidimensional systems, but in a way that includes an accurate description of the quantum effects inherent to many important systems on the molecular level. The foundation on which we build this methodology is the theory of semiclassical (SC) dynamics, which we briefly review in the proceeding sections.

1.1 The Semiclassical Approach

SC approximations [17] to quantum theory are older than quantum theory itself. The general idea is to obtain a description of quantum mechanical effects with the ease of computing classical trajectories. Within SC theory we maintain the quantum mechanical principle of superposition, which allows for an accurate description of tunneling, zero-point energy, and interference, but the quantities comprising the superposition are obtained from classical dynamics. Moreover, SC quantities are rigorously derived in the limit that $\hbar$ tends to zero, or, in other words, the limit that $\hbar$ appears small compared to the values of ac-

tion of the problem at hand. Fortunately, the smallest dofs that are generally considered in MD simulations, such as a proton or an H_2 molecule, typically have values of action that are orders of magnitude greater than $\hbar$, so it is reasonable to expect the SC approximation to be consistently valid for all intents and purposes in doing MD.

The review of SC theory in this chapter is hardly exhaustive, and we refer the reader to the text by Child [17] for a thorough treatise of SC theory, history, and applications; but our intent in the remainder of this chapter is to touch upon some of the more influential results of SC theory over the past century in order to provide context surrounding the new SC methods presented in later chapters, and to motivate the significant computational advantages these new methods contain.

1.1.1 A Brief Survey of Early SC Theories

Asymptotic solutions to Schrödinger's [18] time-independent equation,

$$H\psi(x) = E\psi(x), \tag{1.1}$$

emerged from Wentzel [19], Kramers [20], and Brillouin [21] merely within a year after the publication of Eq. 1.1 and, somewhat remarkably, from Jeffreys [22] in the year prior. In Eq. 1.1, $H = \frac{-\hbar^2}{2m}\frac{d^2}{dx^2} + V(x)$ is the Hamiltonian operator, V is the potential energy function, m is the mass, $\psi(x)$ is the wavefunction at position x, $i = \sqrt{-1}$ is the imaginary unit, and E is the total energy. Here we follow Child [17] and begin a brief derivation of the so-called JWKB

approximation by first rewriting Eq. 1.1 as

$$\left[\hbar^2 \frac{d^2}{dx^2} + p^2(x)\right]\psi(x) = 0, \tag{1.2}$$

with classical momentum

$$p(x) = \{2m[E - V(x)]\}^{\frac{1}{2}}. \tag{1.3}$$

Assuming that changes in $p(x)$ are sufficiently small with respect to changes in x, a general solution to Eq. 1.2 is

$$\psi(x) = Ae^{\pm\frac{i}{\hbar}S(x)}. \tag{1.4}$$

After expanding $S(x)$ in Eq. 1.4 as a power series in $\hbar$,

$$S(x) = S_0(x) + \hbar S_1(x) + \ldots, \tag{1.5}$$

and using the time-independent Schrödinger equation to obtain expressions for S_0 and S_1 in terms of Eq. 1.3,

$$S_0 = \pm\int^x dx'\, p(x'), \tag{1.6}$$

$$S_1 = \frac{i}{2}\ln[p(x)], \tag{1.7}$$

and after removing higher-order powers of $\hbar$ we obtain the general JWKB approximation in the classically allowed region (i.e. where $p^2(x) > 0$),

$$\psi_{JWKB}(x)\Big|_{p^2(x)>0} = \frac{c_+}{p^{\frac{1}{2}}(x)}e^{+\frac{i}{\hbar}\int^x dx'\, p(x')} + \frac{c_-}{p^{\frac{1}{2}}(x)}e^{-\frac{i}{\hbar}\int^x dx'\, p(x')}. \tag{1.8}$$

Furthermore, in the classically forbidden region (i.e. where $p^2(x) < 0$) we have the decaying solution

$$\psi_{JWKB}(x)\Big|_{p^2(x)<0} = \frac{c'_+}{p^{\frac{1}{2}}(x)}e^{+\frac{1}{\hbar}\int^x dx'\, |p(x')|} + \frac{c'_-}{p^{\frac{1}{2}}(x)}e^{-\frac{1}{\hbar}\int^x dx'\, |p(x')|}. \tag{1.9}$$

In Eq. 1.8 and Eq. 1.9 we see the earliest example of an approximate solution to the Schrödinger equation in terms of quantities computable from classical

dynamics. A couple of years later, in the effort to further elucidate the correspondence between quantum and classical expressions for probabilities and averages, Van Vleck [23] generalized the JWKB approach and unearthed the presence of a universal functional determinant Δ given by

$$\Delta = \det \left| \frac{\partial^2 S_0}{\partial q_k \partial \alpha_j} \right|, \tag{1.10}$$

that appears in quantum mechanical quantities the limit that $\hbar$ tends to zero. For example, Van Vleck proved that, as $\hbar \to 0$, the quantum mechanical transition amplitude $\langle q|\alpha\rangle$ to pass from the canonically conjugate set of variables (p, q) to the new set of canonically conjugate variables (α, β) is given by

$$\langle q|\alpha\rangle = A^{\frac{1}{2}} \Delta^{\frac{1}{2}} e^{\frac{i}{\hbar} S_0}, \tag{1.11}$$

where S_0 is the classical action, Δ is the determinant in Eq. 1.10, and A is for normalization [23].

We clearly see from the above results the development of a pedagogically rich connection between classical and quantum perspectives of nature. In subsequent years this picture was further improved upon by significant contributions from Langer [24], Landau [25], Zener [26], and later by Ford and Wheeler [27], Berry and Mount [28], Pechukas [29], Marcus [30], Gutzwiller [31,32], and many others [17].

A particularly enlightening and unifying perspective on quantum-classical correspondence, however, was offered by Miller [33] in terms of the connection between unitary transformations in quantum theory, canonical transformations of classical theory, and the stationary phase approximation (which will be discussed in detail below). For example, consider the quantum mechanical transition element from coordinate q to coordinate Q: $\langle q|Q\rangle = Ae^{i\phi}$. In the limit of

stationary phase, i.e. the limit in which $\hbar$ tends to zero, Miller proved that the phase ϕ and amplitude A of $\langle q|Q\rangle$ are given by

$$\phi = \frac{1}{\hbar} F_1(q, Q), \tag{1.12}$$

$$A = \left[\frac{-1}{2\pi i\hbar} \frac{\partial^2 F_1(q, Q)}{\partial q \partial Q}\right]^{\frac{1}{2}}, \tag{1.13}$$

where $F_1(q, Q)$ is the classical generating function that facilitates the $(q, p) \rightarrow (Q, P)$ canonical transformation using the old coordinate q and new coordinate Q. Similar identities are found by employing different combinations of new and old variables of the two sets of canonically conjugate variables, each combination using a different generating function [33, 34].

We can use Miller's formalism [33] to unify the SC concepts outlined above. For example, we can derive an SC energy eigenstate $\langle q|E\rangle$ with an F_2-type generating function that employs the old coordinate q and new momentum $P = E = \frac{p^2}{2m} + V(q)$. This generating function satisfies

$$p(q, P) = \frac{\partial F_2(q, P)}{\partial q}, \tag{1.14}$$

$$Q(q, P) = \frac{F_2(q, P)}{\partial P}. \tag{1.15}$$

It follows that this F_2 generating function is a solution to the classical Hamilton-Jacobi equation,

$$F_2(q, P) = \pm \int dq \left\{2m\left[E - V(q)\right]\right\}^{\frac{1}{2}}, \tag{1.16}$$

the second derivative of which is

$$\frac{\partial^2 F_2(q, P)}{\partial q \partial P} = \pm \left\{2m\left[E - V(q)\right]\right\}^{-\frac{1}{2}}. \tag{1.17}$$

It therefore follows from Eq. 1.16 and Eq. 1.17 and the forms of Eq. 1.12 and Eq. 1.13 that the SC approximation to the energy eigenstate $\langle q|E\rangle$ is equivalent to the JWKB approximation of Eq. 1.8 [34].

Miller's formalism [33] can also be used to derive the Van Vleck formula for semiclassical time-evolution, i.e. the Van Vleck propagator. The generating function that facilitates the canonical transformation of a set of coordinates and momenta at time zero, (q_0, p_0), to a set of coordinates and momenta at a later time t, (q_t, p_t), by employing the old coordinate q_0 and new coordinate q_t, is an F_1-type generator. It is known from classical mechanics, however, that the generating function of this canonical transformation is, in fact, the classical action. The SC transition amplitude from q_0 to q_t is therefore given by

$$\langle q_t | q_0 (t) \rangle = \left[\frac{-1}{2\pi i\hbar} \frac{\partial^2 S (q_t, q_0, t)}{\partial q_0 \partial q_t} \right]^{\frac{1}{2}} e^{\frac{i}{\hbar} S(q_t, q_0, t)}, \tag{1.18}$$

which is equivalent to the Van Vleck formula of Eq. 1.11 with the two appropriate sets of canonically conjugate variables [34].

1.1.2 From the Feynman Path Integral to the SC-IVR

While they very clearly highlight the correspondence between classical and quantum perspectives of nature, the SC theories presented up to this point have little practical benefit; the application of the JWKB approximation, the Van Vleck formula, Miller's SC matrix elements, and other early SC theories to an arbitrarily large complex chemical system is generally not a computationally feasible endeavor. In this section we begin with a completely different approach to deriving SC quantities (specifically the SC real time propagator), one that begins with the Feynman path integral and smoothly transitions (as the author believes) into the more computationally tractable theories of Heller [35,36], Herman and Kluk [37], Miller [38], and, subsequently, the new methods introduced in this dissertation.

Feynman [39] as well as Feynman and Hibbs [40] showed that the quantum mechanical propagator,

$$K\left(\mathbf{q}_t, \mathbf{q}_0; t\right) = \langle \mathbf{q}_t | e^{-\frac{i}{\hbar}\hat{H}t} | \mathbf{q}_0 \rangle \,, \tag{1.19}$$

i.e. the probability amplitude to evolve from position $|\mathbf{q}_0\rangle$ to position $|\mathbf{q}_t\rangle$ under the influence of Hamiltonian $\hat{H}$ in time t, is exactly represented by a continuous sum over a pure phase associated with each of the infinite number of paths connecting $|\mathbf{q}_0\rangle$ and $|\mathbf{q}_t\rangle$ in time t (see Fig. 1.1):

$$K\left(\mathbf{q}_t, \mathbf{q}_0; t\right) = \int_{\mathbf{q}_0}^{\mathbf{q}_t} \mathcal{D}\left[\mathbf{q}\left(t\right)\right] \; e^{\frac{i}{\hbar} S\left[\mathbf{q}(t)\right]}. \tag{1.20}$$

In Eq. 1.20, $S\left[\mathbf{q}\left(t\right)\right]$ is the action functional associated with path $\mathbf{q}\left(t\right)$, $\mathcal{D}\left[\mathbf{q}\left(t\right)\right]$ is the path differential, and the limits of integration specify that each path originates at position $\mathbf{q}_0$ at time zero and ends at position $\mathbf{q}_t$ at time t. The consequences of the path integral formulation of quantum theory are far reaching, having a profound influence on the development of quantum statistical mechanics, quantum field theory, and a variety of approximations to quantum time-evolution [40], but here we are interested in the behavior of Eq. 1.20 in the semiclassical limit. That is, we proceed by evaluating Eq. 1.20 in the asymptotic limit where $\hbar \to 0$.

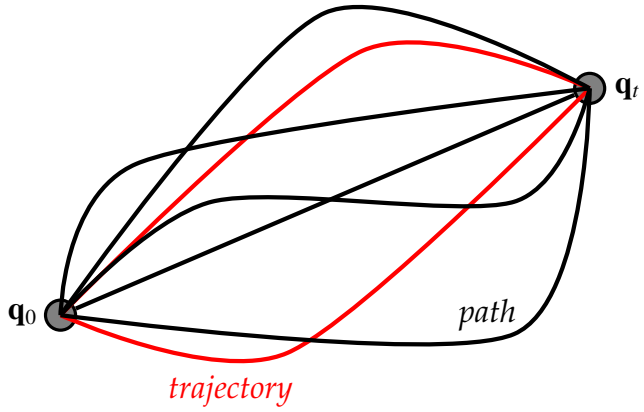

Figure 1.1: The Feynman real time path integral is a continuous sum of phase factors associated with the infinite set of paths (black curves), including classical trajectories (red curves, if they exist), connecting coordinates $\mathbf{q}_0$ and $\mathbf{q}_t$ in time t.

Given that Eq. 1.20 contains an integral over a phase factor that oscillates very quickly as $\hbar$ appears small compared to the action functional, it is reasonable to assume that the largest contributions to the path integral will come from the paths that exist in the vicinity of paths that make the action stationary, and that the contributions from all other paths will cancel each other out on average. Mathematically, this approximation is known as the stationary phase approximation, and here we derive it. Consider an arbitrary oscillatory integral I,

$$I = \int d\mathbf{x}\, g\left(\mathbf{x}\right) e^{\frac{i}{\hbar}\phi(\mathbf{x})}. \tag{1.21}$$

The procedure is to expand the phase $\phi\left(\mathbf{x}\right)$ around the set of its stationary points $\left\{\mathbf{x}_j\right\}$ up to second order,

$$I \approx \sum_j \int d\mathbf{x}\, g\left(\mathbf{x}_j\right) e^{\frac{i}{\hbar}\left[\phi\left(\mathbf{x}_j\right)+\frac{1}{2!}\left(\mathbf{x}-\mathbf{x}_j\right)^{\mathrm{T}}\boldsymbol{\mathcal{H}}_j\left(\mathbf{x}-\mathbf{x}_j\right)\right]}, \tag{1.22}$$

and evaluate the remaining integral analytically to obtain the stationary phase

approximation to the integral I:

$$I_{SPA} = \sum_j \frac{(2\pi i\hbar)^{\frac{N}{2}}}{\det\left[\boldsymbol{\mathcal{H}}_j\right]^{\frac{1}{2}}} g\left(\mathbf{x}_j\right) e^{\frac{i}{\hbar}\phi\left(\mathbf{x}_j\right)}. \tag{1.23}$$

The sum is over each of the stationary points of the phase $\phi(\mathbf{x})$, and elements of the Hessian at each stationary point are given by

$$\left(\mathcal{H}_j\right)_{mn} = \left.\frac{\partial^2\phi(\mathbf{x})}{\partial x_m \partial x_n}\right|_{\mathbf{x}=\mathbf{x}_j}. \tag{1.24}$$

Note that I_{SPA} is an exact representation of I in the semiclassical limit,

$$\lim_{\hbar\to 0} I = I_{SPA}, \tag{1.25}$$

which, as stated before, is not a drastic approximation in typical MD simulations.

To evaluate the Feynman path integral of Eq. 1.20 under the stationary phase approximation, therefore, we expand the action $S[\mathbf{q}(t)]$ in Eq. 1.20 around the set of paths that make the action stationary $\{\mathbf{q}_c(t)\}$. It is known from Hamilton [41] that these paths are, in fact, the solutions to the classical equations of motion, i.e. classical trajectories:

$$\delta S[\mathbf{q}_c(t)] = 0. \tag{1.26}$$

We therefore expand to second-order the action on the right-hand side Eq. 1.20 around the classical trajectories that evolve from position $\mathbf{q}_0$ to position $\mathbf{q}_t$ under the influence of Hamiltonian H in time t, and evaluate the remaining integral analytically to yield the Van Vleck propagator [23, 32, 42, 43],

$$K_{SC}(\mathbf{q}_t, \mathbf{q}_0; t) = \sum_{\text{traj.}} \det\left[2\pi i\hbar\,\mathbf{M}_{qp}\right]^{-\frac{1}{2}} e^{\frac{i}{\hbar}S[\mathbf{q}_t]}. \tag{1.27}$$

Note that it is more computationally convenient to represent the Hessian of the action in terms of elements of the so-called monodromy matrix $\mathbf{M}$: $\mathbf{M}_{\alpha\beta} = \frac{\partial\boldsymbol{\alpha}_t}{\partial\boldsymbol{\beta}_0}$

and $(\alpha, \beta) \in (\mathbf{p}, \mathbf{q})$. That is, we have used the following identity in Eq. 1.27,

$$\mathbf{M}_{qp} = \left[\frac{-\partial^2 S}{\partial \mathbf{q}_0 \partial \mathbf{q}_t} \right]^{-1} . \tag{1.28}$$

In Eq. 1.27 we have also dropped the subscript c from the trajectory, since it is assumed that the sum is strictly over contributions from classical trajectories. The picture associated with Eq. 1.27 [see Fig. 1.2] has changed from a continuous sum over all paths connecting $\mathbf{q}_0$ and $\mathbf{q}_t$ to a discrete sum over the trajectories that connect $\mathbf{q}_0$ and $\mathbf{q}_t$; and each trajectory is weighted by a complex prefactor that captures quadratic fluctuations surrounding it.

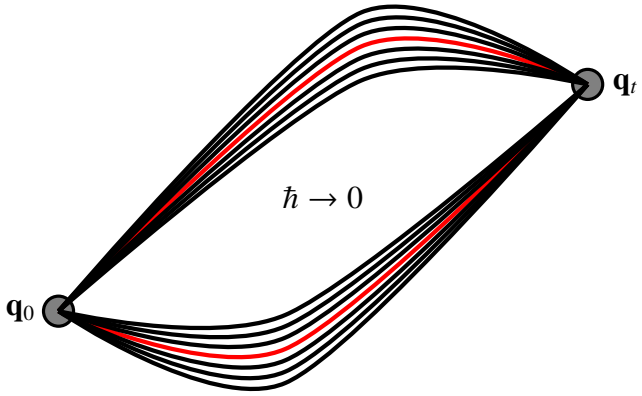

Figure 1.2: Within the stationary phase approximation to the Feynman path integral, the continuous sum over all paths connecting $\mathbf{q}_0$ and $\mathbf{q}_t$ in time t reduces to a discrete sum over classical trajectories (red curves). A complex prefactor accounts for small fluctuations (black curves) around the classical trajectories. This approximation is exact in the limit that $\hbar \to 0$.

For purposes that will arise later when considering the time-correlation function, we proceed by recasting Eq. 1.27 as an SC representation to the time-evolution operator $e^{-\frac{i}{\hbar}\hat{H}t}$, rather than the propagator. Using two resolutions of

the identity we have

$$e^{-\frac{i}{\hbar}\hat{H}t} = \int d\mathbf{q}_0 \int d\mathbf{q}_t \, |\mathbf{q}_t\rangle \langle \mathbf{q}_t| e^{-\frac{i}{\hbar}\hat{H}t} |\mathbf{q}_0\rangle \langle \mathbf{q}_0| \,. \tag{1.29}$$

After inserting Eq. 1.27 into Eq. 1.29 we obtain the SC approximation to $e^{-\frac{i}{\hbar}\hat{H}t}$,

$$e^{-\frac{i}{\hbar}\hat{H}t} \approx \frac{1}{(2\pi i\hbar)^N} \sum_{\text{traj.}} \int d\mathbf{q}_0 \int d\mathbf{q}_t \det\left[\mathbf{M}_{qp}\right]^{-\frac{1}{2}} e^{\frac{i}{\hbar}S[\mathbf{q}(t)]} \, |\mathbf{q}_t\rangle \langle \mathbf{q}_0| \,, \tag{1.30}$$

where N is the full dimensionality of the system. There are two significant computational challenges associated with employing Eq. 1.30 on a general chemical system. First of all, we are required to conduct a numerical search for all trajectories satisfying the double-ended boundary condition, which is particularly inefficient for highly multidimensional systems. Secondly, the prefactor on the right-hand side of Eq. 1.30 can approach infinity at the focal points of an ensemble of trajectories. For example, consider the two trajectories of the 1D harmonic oscillator in Fig. 1.3(a). Each trajectory passes through a focal point at $q(t = \pi)$, at which time the inverse of M_{qp} diverges to infinity.

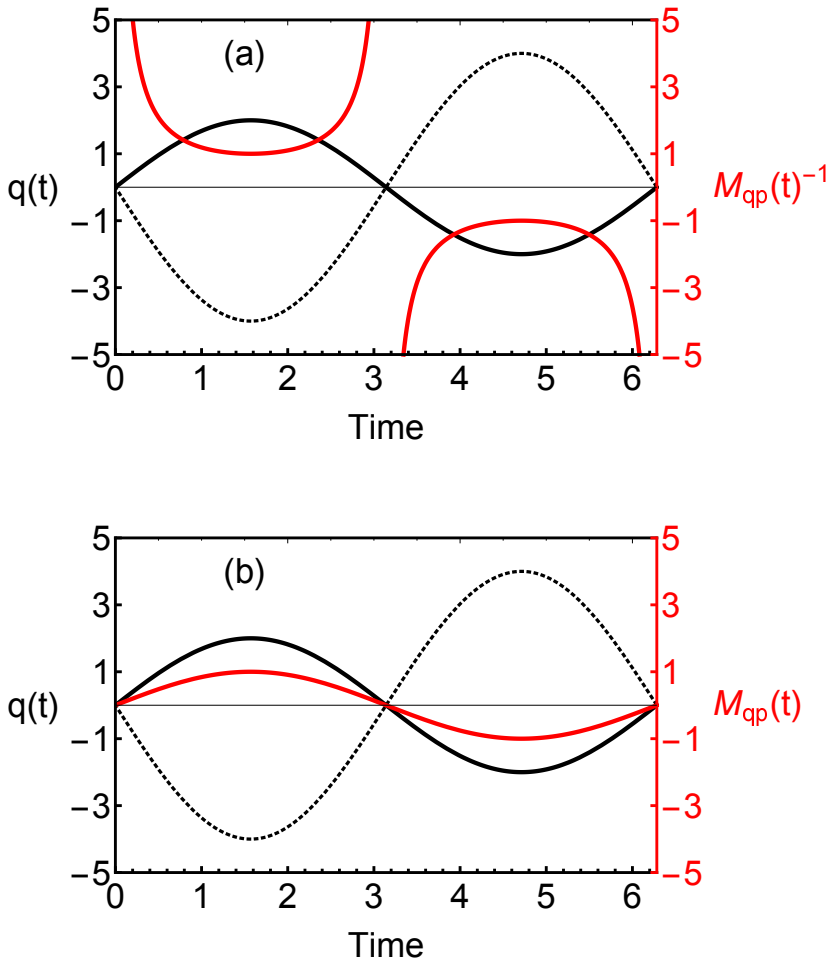

Figure 1.3: Two trajectories of the 1D harmonic oscillator with spring constant $k = 1$ and initial coordinate $q(0) = 0$. The initial momenta are $p(0) = 2$ (black), $p(0) = -4$ (dashed). We also plot the (a) inverse of $M_{qp}(t)$ (red) associated with the first trajectory as well as $M_{qp}(t)$ (red) in panel (b).

Both of these problems can be remedied by employing the so-called "IVR trick" [38, 44] in Eq. 1.30, where the integral over final positions is converted to an integral over initial momenta:

$$\sum_{\text{traj.}} \int d\mathbf{q}_t \equiv \int d\mathbf{p}_0 \det\left[\mathbf{M}_{qp}\right]. \tag{1.31}$$

Using Eq. 1.31 on Eq. 1.30 then gives the Van Vleck initial value representation

[38, 44] (IVR) for the SC time-evolution operator,

$$e^{-\frac{i}{\hbar}\hat{H}t} \approx \frac{1}{(2\pi i\hbar)^N} \int d\mathbf{q}_0 \int d\mathbf{p}_0 \det\left[\mathbf{M}_{qp}\right]^{\frac{1}{2}} e^{\frac{i}{\hbar}S\left[\mathbf{q}(t)\right]} |\mathbf{q}_t\rangle \langle \mathbf{q}_0| \,. \tag{1.32}$$

In employing the "IVR trick" to obtain Eq. 1.32 we have converted the double-ended boundary condition into an average over initial conditions in phase space, which conveniently grants us the ability to implement Monte Carlo (MC) methods to sample unique trajectories rather than conduct an inefficient root-search for special trajectories. We have also shifted the determinant into the numerator, thus avoiding the numerical trouble of coping with infinities [see Fig. 1.3(b)].

While the Van Vleck IVR has been used successfully, such as in the SC calculation of scattering amplitudes [44] and chemical reaction rates [45], a much more computationally efficient, and theoretically equivalent, methodology was introduced by Herman and Kluk [37, 46–49]. With the Herman-Kluk IVR (HK-IVR) a basis of coherent states [50] is employed to represent the SC time-evolution operator. Coherent states are intermediate between position and momentum states. They satisfy minimum uncertainty, and they generally offer a natural means of MC sampling each initial phase space variable. The HK-IVR approximation to the time-evolution operator is given by

$$e^{-i\hat{H}t} \approx \frac{1}{(2\pi)^N} \int d\mathbf{z}_0 \; C_t\left(\mathbf{z}_0, \mathbf{z}_t; \gamma_0, \gamma_t\right) e^{iS_t(\mathbf{z}_0)} |\mathbf{z}_t\rangle \langle \mathbf{z}_0| \,. \tag{1.33}$$

Note that in Eq. 1.33, and throughout the remainder of this dissertation, we take $\hbar = 1$ and use $S_t\left(\mathbf{z}_0\right)$ to represent the classical action of a trajectory originating at phase space point $\mathbf{z}_0 = (\mathbf{q}_0, \mathbf{p}_0)$. We also use $\mathbf{z}_t$ to represent the phase space point of a trajectory at time t, $\mathbf{z}_t = (\mathbf{q}_t, \mathbf{p}_t)$. Depending upon the methodology being considered, and for convenience, we will switch between $\mathbf{z}$ and $(\mathbf{q}, \mathbf{p})$ notation throughout the manuscript. The complex prefactor $C_t\left(\mathbf{z}_0, \mathbf{z}_t; \gamma_0, \gamma_t\right)$ appearing in

Eq. 1.33 is given by

$$C_t(\mathbf{z}_0, \mathbf{z}_t; \gamma_0, \gamma_t) = \det\left[\frac{1}{2}\left(\gamma_t^{\frac{1}{2}}\mathbf{M}_{qq}\gamma_0^{-\frac{1}{2}} + \gamma_t^{-\frac{1}{2}}\mathbf{M}_{pp}\gamma_0^{\frac{1}{2}} + i\gamma_t^{-\frac{1}{2}}\mathbf{M}_{pq}\gamma_0^{-\frac{1}{2}} - i\gamma_t^{\frac{1}{2}}\mathbf{M}_{qp}\gamma_0^{\frac{1}{2}}\right)\right]^{\frac{1}{2}}, \tag{1.34}$$

and the elements of the diagonal matrices γ_0 and γ_t determine the spread of the coherent states $|\mathbf{z}_0\rangle$ and $|\mathbf{z}_t\rangle$ in position and momentum space at time zero and time t, respectively. The position-space wavefunction of the coherent state is given by

$$\langle\tilde{\mathbf{x}}|\mathbf{z}\rangle = \left(\frac{\det[\gamma]}{\pi^N}\right)^{\frac{1}{4}} e^{-\frac{1}{2}(\tilde{\mathbf{x}}-\mathbf{q})^{\mathrm{T}}\boldsymbol{\gamma}(\tilde{\mathbf{x}}-\mathbf{q})+i\mathbf{p}^{\mathrm{T}}(\tilde{\mathbf{x}}-\mathbf{q})}, \tag{1.35}$$

and the momentum-space wavefunction of the coherent state is given by

$$\langle\tilde{\mathbf{p}}|\mathbf{z}\rangle = \left(\frac{1}{\det[\gamma]\,\pi^N}\right)^{\frac{1}{4}} e^{-\frac{1}{2}(\tilde{\mathbf{p}}-\mathbf{p})^{\mathrm{T}}\boldsymbol{\gamma}^{-1}(\tilde{\mathbf{p}}-\mathbf{p})-i\tilde{\mathbf{p}}^{\mathrm{T}}\mathbf{q}}. \tag{1.36}$$

HK-IVR (and variations thereof) have been extensively studied and proven to be very successful at describing quantum effects in both adiabatic and nonadiabatic systems [38,46,49,51–83], and it will serve as the starting point for the new methodologies presented later in this dissertation.

1.1.3 SC Correlation Functions

The quantities of interest when studying molecular systems (such as mechanical properties, chemical reaction rates, and various forms of spectra) can often be expressed in terms of a time-correlation function. The quantum mechanical form of the time-correlation function is given by

$$C_{AB}^{QM}(t) = \mathrm{Tr}\left[\hat{A}e^{i\hat{H}t}\hat{B}e^{-i\hat{H}t}\right], \tag{1.37}$$

with general operators $\hat{A}$ and $\hat{B}$, and $\mathrm{Tr}\,[\Xi]$ is the trace of matrix Ξ. An SC form of Eq. 1.37 is obtained by inserting an SC-IVR of choice in place of the time-evolution operators. For example, this dissertation is concerned with the so-called double Herman-Kluk time-correlation function (DHK-IVR), which is obtained by inserting Eq. 1.33 and its complex conjugate into Eq. 1.37:

$$C_{AB}^{DHK}(t) = \frac{1}{(2\pi)^{2N}} \int d\mathbf{z}_0 \int d\mathbf{z}_t' \, A_{\mathbf{z}_0\mathbf{z}_0'} B_{\mathbf{z}_t'\mathbf{z}_t} e^{i[S_t(\mathbf{z}_0)+S_{-t}(\mathbf{z}_t')]} C_t\,(\mathbf{z}_0, \mathbf{z}_t; \gamma_0, \gamma_t)\, C_{-t}\,(\mathbf{z}_t', \mathbf{z}_0'; \gamma_t, \gamma_0)\,. \tag{1.38}$$

In Eq. 1.38 we have used the following notation to represent the coherent state matrix element of a given operator $\hat{\Omega}$,

$$\Omega_{\mathbf{z}\mathbf{z}'} \equiv \langle \mathbf{z}|\hat{\Omega}|\mathbf{z}'\rangle\,, \tag{1.39}$$

and the primed phase space variables correspond to a trajectory originating at $\mathbf{z}_t'$, which evolves backwards in time t to point $\mathbf{z}_0'$. Though Eq. 1.38 and its variations have been successfully used on a number of interesting systems [56,58,60,63,65,72,75], the oscillatory nature of the integrand generally restricts its application to systems with only a few dofs. In order to contrive an efficient SC-IVR method that is applicable to highly multidimensional systems, and that contains a true description of all quantum mechanical effects, we therefore need additional approximations.

1.1.4 Leading Approaches to the "Sign Problem"

Of the leading approaches to improve upon the "sign problem" of HK-IVR-based methods, one of which is the method of time averaging [68,69] (TA). The TA procedure does not employ additional approximations, but rather relies on

the following feature of a phase space average. That is, given a phase space average I,

$$I = \int d\mathbf{p}_0 \int d\mathbf{q}_0 \, A\left(\mathbf{p}_0, \mathbf{q}_0\right), \tag{1.40}$$

the TA version of I is given by

$$I_{TA} = \int d\mathbf{p}_0 \int d\mathbf{q}_0 \frac{1}{T} \int_0^T dt \, A\left(\mathbf{p}_t, \mathbf{q}_t\right). \tag{1.41}$$

Simply by invoking Liouville's theorem it is easy to show that the TA version of I is, in fact, equal to the original phase space average,

$$I_{TA} = I. \tag{1.42}$$

While the TA version of the integral does require additional effort (an extra 1D integral over time), the amount of effort is reasonably small, and easily carried out in the process of computing individual trajectories [15]. The advantage of using the TA version is that it can smooth out the oscillatory structure of the integrand and, consequently, greatly reduce the number of trajectories required to achieve convergence. This approach has shown great promise in computing the vibrational energy levels of small molecules [68, 69] and in highly multidimensional system-bath models [79, 80, 84].

Another promising approach to alleviating the "sign problem" in HK-IVR-based methods is the forward-backward (FB-IVR) approach [58, 63, 85–87]. This method involves partially combining the two time-evolution operators of the time-correlation function into a single SC propagator; a stationary phase approximation is invoked at each time t, effectively linking the two forward and backward trajectories into a single FB trajectory [15]. Unlike the TA approach, FB-IVR and its variations involve additional approximations on top of the original SC approximation, but, like the TA approach, the advantage is that far fewer

trajectories are required for convergence, and, moreover, convergence of highly multidimensional systems is possible.

The final leading approach to alleviating the SC-IVR "sign problem", and the prevalent theme of this dissertation, is the method of modified Filinov filtration (MFF), which is outlined in detail in the following section.

1.1.5 Modified Filinov Filtration

The method originates with Filinov [88] and the effort to evaluate integrals of complex-valued functions, specifically the Feynman path integral, with MC sampling. Makri and Miller [89] later generalized the procedure and showed that the stationary phase approximation is recovered as an extreme limit of the transformation. Here we follow their derivation. Begin by considering the integral of a pure phase,

$$I = \int dx\, e^{i\phi(x)}, \tag{1.43}$$

where the phase function $\phi(x)$ is, in general, complex. Given that the integrand in Eq. 1.43 is oscillatory, one can assume that the largest contributions to the integral come from regions of x in the vicinity of the stationary points of $\phi(x)$. The goal is to therefore insert a Gaussian filter centered about those regions of stationary phase and effectively damp the oscillatory regions elsewhere. Begin by multiplying Eq. 1.43 by unity in the form of a Gaussian integral,

$$1 = \left(\frac{\Gamma}{2\pi}\right)^{\frac{1}{2}} \int d\bar{x}\; e^{-\frac{1}{2}\Gamma(\bar{x}-x)^2}, \tag{1.44}$$

to obtain

$$I = \left(\frac{\Gamma}{2\pi}\right)^{\frac{1}{2}} \int dx \int d\bar{x}\, e^{i\phi(x)} e^{-\frac{1}{2}\Gamma(x-\bar{x})^2}. \tag{1.45}$$

The constant $\Gamma > 0$ determines the width of the Gaussian. Now expand the phase function $\phi(x)$ to second order around the center of the Gaussian,

$$\phi(x) \approx \phi(\bar{x}) + \phi'(\bar{x})(x - \bar{x}) + \frac{1}{2}\phi''(\bar{x})(x - \bar{x})^2. \tag{1.46}$$

Next, insert Eq. 1.46 into Eq. 1.45,

$$I \approx \left(\frac{\Gamma}{2\pi}\right)^{\frac{1}{2}} \int d\bar{x}\, e^{i\phi(\bar{x})} \int dx\, e^{-\frac{1}{2}\left[\Gamma - i\phi''(\bar{x})\right](x-\bar{x})^2} e^{i\phi'(\bar{x})(x-\bar{x})}, \tag{1.47}$$

and the integral over x can now be evaluated analytically to obtain an approximation to I,

$$I \approx \int d\bar{x} \left(\frac{\Gamma}{\Gamma - i\phi''(\bar{x})}\right)^{\frac{1}{2}} e^{i\phi(\bar{x})} e^{-\frac{\phi'(\bar{x})^2}{2\left[\Gamma - i\phi''(\bar{x})\right]}}. \tag{1.48}$$

Makri and Miller [89] noted that Eq. 1.48 holds even if Γ is complex. One can therefore choose

$$\Gamma = i\phi''(\bar{x}) + \frac{1}{c}, \tag{1.49}$$

with constant $c \geq 0$. Substituting Eq. 1.49 into Eq. 1.48 gives an approximation to the integral I that is parametrized by c,

$$\begin{aligned} I \approx & I_c \\ = & \int d\bar{x} \left[1 + ic\phi''(\bar{x})\right]^{\frac{1}{2}} e^{i\phi(\bar{x})} e^{-\frac{c}{2}\phi'(\bar{x})^2}. \end{aligned} \tag{1.50}$$

The integrand in Eq. 1.50 is recognized as the same integrand in Eq. 1.43 but multiplied by a damping factor $F(x; c)$:

$$I_c = \int dx F(x; c)\, e^{i\phi(x)} \tag{1.51}$$

$$F(x; c) = \left[1 + ic\phi''(x)\right]^{\frac{1}{2}} e^{-\frac{c}{2}\phi'(x)^2}. \tag{1.52}$$

Eq. 1.51 and Eq. 1.52 define the first result of this section; I_c is the MFF transform of the integral I. The generalization of Eq. 1.52 to multiple dofs is straightforward:

$$F(\mathbf{x}; \mathbf{c}) = \det\left[\mathbb{I} + i\mathbf{c}\boldsymbol{\mathcal{H}}\right]^{\frac{1}{2}} e^{-\frac{1}{2}\boldsymbol{\nabla}\phi^{\mathrm{T}}\mathbf{c}\boldsymbol{\nabla}\phi}, \tag{1.53}$$

with elements of the Hessian given by $\mathcal{H}_{ij} = \frac{\partial^2 \phi(\mathbf{x})}{\partial x_i \partial x_j}$, $\mathbb{I}$ is the identity matrix, $\mathbf{c}$ is a diagonal matrix of c parameters, and $\boldsymbol{\nabla}\phi$ is the gradient of ϕ with respect to $\mathbf{x}$.

Note the limiting behavior of the approximate integral I_c in terms of the so-called tuning parameter c. In the limit that c tends to zero, Eq. 1.52 approaches unity and I_c approaches I exactly:

$$\lim_{c \to 0} I_c = I. \tag{1.54}$$

On the other hand, as c tends to infinity, the Gaussian filter surrounding the regions of stationary phase becomes infinitely narrow. Using the following representation of a δ-function,

$$\lim_{a \to \infty} \left(\frac{a}{2\pi} \right)^{\frac{1}{2}} e^{-\frac{a}{2} x^2} = \delta(x), \tag{1.55}$$

the damping factor can be evaluated analytically in this limit:

$$\lim_{c \to \infty} F(x; c) = \left[2\pi i \phi''(x) \right]^{\frac{1}{2}} \delta\left[\phi'(x) \right]. \tag{1.56}$$

The approximate integral I_c is then given by

$$\lim_{c \to \infty} I_c = (2\pi i)^{\frac{1}{2}} \int dx \, \phi''(x)^{\frac{1}{2}} \, \delta\left[\phi'(x) \right] e^{i\phi(x)}. \tag{1.57}$$

Given that the composition of a δ-function $\delta(x)$ with another function $g(x)$ can be written as a weighted sum of δ-functions at each stationary point of $g(x)$,

$$\delta\left[g(x) \right] = \sum_j \frac{\delta\left(x - x_j \right)}{\left| g'\left(x_j \right) \right|}, \tag{1.58}$$

Eq. 1.57 reduces to

$$\begin{aligned} \lim_{c \to \infty} I_c &= \sum_j (2\pi i)^{\frac{1}{2}} \int dx \, \frac{\delta\left(x - x_j \right)}{\phi''(x)^{\frac{1}{2}}} e^{i\phi(x)} \\ &= \sum_j \left[\frac{2\pi i}{\phi''\left(x_j \right)} \right]^{\frac{1}{2}} e^{i\phi(x_j)}, \end{aligned} \tag{1.59}$$

which is precisely the stationary phase approximation to the original integral I,

$$\lim_{c\to\infty} I_c = I_{SPA}. \tag{1.60}$$

The multidimensional generalization of Eq. 1.59 is straightforward:

$$\begin{aligned}\lim_{\mathbf{c}\to\infty} I_{\mathbf{c}} =& \sum_j \det\left[\frac{1}{2\pi i}\boldsymbol{\mathcal{H}}_j\right]^{\frac{1}{2}} e^{i\phi(\mathbf{x}_j)} \\ =& I_{SPA},\end{aligned} \tag{1.61}$$

with elements of the Hessian given by $\left(\mathcal{H}_j\right)_{mn} = \left.\frac{\partial^2\phi(\mathbf{x})}{\partial x_m \partial x_n}\right|_{\mathbf{x}=\mathbf{x}_j}$. We therefore conclude that the tuning parameters of MFF serve as a handle that smoothly interpolates the value of an oscillatory integral between itself and its stationary phase approximation.

Though originally designed to approximate the real time path integral, MFF and variations thereof are applicable to any integral of a complex function, and have proven very useful in approximating SC time-evolution for the computation of tunneling properties [55] as well as absorption and photodissociation spectra in both adiabatic [55, 90–92] and nonadiabatic [61, 93] molecular systems. But MFF can be a powerful theoretical tool as well as a practical tool. For example, Miller [48] has shown that HK-IVR can be derived by using MFF on the Van Vleck-IVR, lending to the previously held notion that HK-IVR is a smooth interpolation between two other theoretically equivalent SC-IVRs: the Van Vleck-IVR and its conjugate in momentum-space.

1.2 Other Methods

Though the central theme of this work is to highlight the powerful advantages of using MFF on DHK-IVR, some of the many other promising approaches to

incorporating quantum effects into MD simulations are worth noting, particularly those that are more efficient when considering specific kinds of systems. For example, path integral-based methods such as ring polymer MD [94–97] and centroid MD [98,99] can accurately describe quantum effects like tunneling and zero-point energy in complex chemical systems, and are particularly powerful in computing chemical rates in the condensed phase. These methods, however, lack phase information, and necessarily fail whenever interference plays an important role in the dynamics.

There is also the extensively used linearized [100–103] (LSC-IVR) representation of the SC-IVR time-correlation function,

$$C_{AB}^{LSC}(t) = \frac{1}{(2\pi)^N} \int d\mathbf{z}_0 \; A_W(\mathbf{z}_0) B_W(\mathbf{z}_t) : \tag{1.62}$$

a phase space average over the Wigner distributions of each operator,

$$\Omega_W(\mathbf{z}_0) = \int d\bar{\mathbf{q}} \, e^{-2i\mathbf{p}^{\mathrm{T}}\bar{\mathbf{q}}} \, \langle \mathbf{q} + \bar{\mathbf{q}} | \hat{\Omega} | \mathbf{q} - \bar{\mathbf{q}} \rangle \, . \tag{1.63}$$

LSC-IVR is, however, a classical limit of SC-IVR theory, and only accurate on short time scales. It also suffers from zero-point energy leakage [16, 83], does not preserve detailed balance, and fails to describe long-time coherence effects [38, 64, 75].

Finally, it is worth noting that there are other promising SC methods such as linearization of the density matrix [104], symmetrical windowing [105], and SC quantization [106] for the calculation of electronic coherence and/or 1D and 2D vibrational and vibronic spectra. Still, however, there is need of practical methods that include a true description of nuclear coherence in real time for longer than ultra-fast timescales. These methods can potentially be used on a wide range of interesting systems such as the generation of hot-electrons at

metal surfaces [8, 107], intramolecular vibrational relaxation [108], and other electronically and vibronically nonadiabatic systems [2,4,5,109].

1.3 Thesis and Outline

The main objective of this dissertation is to show that the use of MFF on DHK-IVR is an incredibly powerful theoretical and practical tool for simulating complex chemical systems in real time–specifically systems that exhibit strong nuclear quantum effects such as interference. With the MFF procedure as described above we derive a variety of mixed quantum-classical (MQC) representations of the DHK-IVR time-correlation function that offer a number of significant advantages over existing methods. Some of the overarching advantages are as follows.

The methods presented here *significantly improve upon the SC-IVR "sign problem*." As will be shown, even small amounts of phase filtration with MFF can reduce the number of trajectories required for convergence by orders of magnitude, and without a significant loss of accuracy. Whereas with DHK-IVR one is restricted to simulating systems with only a few dofs, some of the methods presented here are capable of accurately handling systems with, at least, dozens of dofs (and potentially more) with reasonable computational effort. The validity of that statement is, of course, dependent upon a number of conditions, most of which are system-dependent. But, generally, as we shall see, the statement is increasingly valid when the classical subsystem is larger than the quantum subsystem, when the coupling between classical and quantum subsystems is weaker, and, since SC-IVR methods are exact for harmonic motion, when the

system is weakly anharmonic.

Each of these MQC methods offer *mode-specific quantization* in a *dynamically consistent* framework. Whereas in other standard multiphysics approaches where one must make uncontrolled approximations to contain the inconsistencies that arise from simulating coupled quantum and classical dofs [110], the SC-IVR methods presented here rely only on classical trajectories, and so each dof evolves in a uniform dynamical framework.

Furthermore, as is true with similar SC-IVR methods, our MQC methods are *applicable to nonadiabatic systems*. With the Meyer-Miller-Stock-Thoss (MM-ST) Hamiltonian [53, 111, 112] for vibronic systems, both nuclear and electronic dofs can be evolved classically in terms of continuous variables; with each dof therefore treated on an equal dynamical footing, the SC-IVR methods presented here are readily extended to nonadiabatic systems.

Finally, we note that the new methods presented here are significantly *more efficient to implement* than existing SC-IVR time-correlation functions. Within the leading approximations that ease the convergence of DHK-IVR, specifically the FB methods, is an unfavorable scaling with respect to the effort needed to evolve FB trajectories. The methods presented here overcome this scaling and therefore allow for a drastic reduction in computational expense.

In the remainder of this dissertation, we begin by reviewing an existing FB MQC approach to computing the DHK-IVR time-correlation function (FB MQC-IVR), and then we proceed to build and improve upon FB MQC-IVR in the all-encompassing effort of this dissertation to push the applicability of SC theory to large, complex chemical systems. Chapter 2 is devoted to a review of FB MQC-

IVR as well as the introduction of two vastly more efficient implementations of the same methodology. In Chapter 3 we challenge an existing perspective of the MFF procedure in the effort to validate MFF as a powerful practical tool to alleviate the SC-IVR "sign problem." In Chapter 4 we further improve upon the methodologies of Chapter 2 by deriving a representation of DHK-IVR in an analytical MQC limit. In Chapter 5 we review the MM-ST Hamiltonian for vibronic systems, we outline an exactly symplectic algorithm for evolving classical trajectories and the associated monodromy matrix under the MM-ST Hamiltonian, and we extend one of the methods of Chapter 2 to model nonadiabatic systems. In Chapter 6 we outline the SC Corr-Code Package, a FORTRAN-based program developed in-house for the computation of SC-IVR time-correlation functions under a variety of approximations. Finally, in Chapter 7 we comment upon some ongoing projects and draw our major conclusions.

CHAPTER 2

VARIATIONS OF THE MIXED QUANTUM-CLASSICAL IVR

2.1 The Forward-Backward Implementation

The idea of using MFF as means to tune individual dofs of the SC-IVR time-correlation function between two levels of SC-IVR theory can be traced back to the generalized FB-IVR (GFB-IVR) of Thoss et al. [65] As the tuning parameters of GFB-IVR tend to zero, the effect of MFF is removed and DHK-IVR is recovered. And as the tuning parameters approach infinity, GFB-IVR is equivalent to FB-IVR. With an anharmonic system-bath model it was shown that GFB-IVR does not significantly change when bath modes were treated further from the DHK-IVR limit than the system mode, suggesting that phase contributions from individual dofs can be modified independently to facilitate faster convergence and preserve accuracy [65].

This idea was later modified by Ananth [113] and Antipov et al. [78] so that the stationary phase limit of MFF yields a classical limit time-correlation function similar to LSC-IVR–one in which the forward and backward trajectories are identical and, therefore, phase information is completely canceled. This methodology should be more efficient to implement than GFB-IVR since its stationary phase limit contains less phase information than the stationary phase limit of GFB-IVR. Here we review a general derivation of Ananth and Antipov's method which, as mentioned in the previous chapter, we refer to as FB MQC-IVR.

The goal is to define a phase function ϕ to use in the MFF damping factor

such that the zero and infinite limits of the tuning parameters give DHK-IVR and its linearized counterpart, which we refer to as Husimi-IVR, respectively. By neglecting the contributions from either of the two operators and from the HK-IVR prefactors, we define the phase function ϕ of Eq. 1.38 to be

$$\begin{aligned}\phi =& S_t(\mathbf{p}_0,\mathbf{q}_0) + S_{-t}(\mathbf{p}_t',\mathbf{q}_t') + \frac{i}{4}(\mathbf{p}_0-\mathbf{p}_0')^{\mathrm{T}}\gamma_0^{-1}(\mathbf{p}_0-\mathbf{p}_0') + \frac{i}{4}(\mathbf{q}_0-\mathbf{q}_0')^{\mathrm{T}}\gamma_0(\mathbf{q}_0-\mathbf{q}_0') \\ &+\frac{1}{2}(\mathbf{p}_0+\mathbf{p}_0')^{\mathrm{T}}(\mathbf{q}_0-\mathbf{q}_0') + \frac{i}{4}(\mathbf{p}_t'-\mathbf{p}_t)^{\mathrm{T}}\gamma_t^{-1}(\mathbf{p}_t'-\mathbf{p}_t) + \frac{i}{4}(\mathbf{q}_t'-\mathbf{q}_t)^{\mathrm{T}}\gamma_t(\mathbf{q}_t'-\mathbf{q}_t) \\ &+\frac{1}{2}(\mathbf{p}_t'+\mathbf{p}_t)^{\mathrm{T}}(\mathbf{q}_t'-\mathbf{q}_t). \end{aligned} \tag{2.1}$$

The derivatives of Eq. 2.1 with respect to the variables of integration in Eq. 1.38 are given by

$$\frac{\partial\phi}{\partial\mathbf{q}_t'} = -\frac{1}{2}\left(\mathbf{M}_{pq}^{(b)T} - i\mathbf{M}_{qq}^{(b)T}\gamma_0\right)\boldsymbol{\Delta}_{q_0} + \frac{1}{2}\left(\mathbf{M}_{qq}^{(b)T} + i\mathbf{M}_{pq}^{(b)T}\gamma_0^{-1}\right)\boldsymbol{\Delta}_{p_0} + \frac{i}{2}\gamma_t\boldsymbol{\Delta}_{q_t} - \frac{1}{2}\boldsymbol{\Delta}_{p_t}, \tag{2.2}$$

$$\frac{\partial\phi}{\partial\mathbf{p}_t'} = -\frac{1}{2}\left(\mathbf{M}_{pp}^{(b)T} - i\mathbf{M}_{qp}^{(b)T}\gamma_0\right)\boldsymbol{\Delta}_{q_0} + \frac{1}{2}\left(\mathbf{M}_{qp}^{(b)T} + i\mathbf{M}_{pp}^{(b)T}\gamma_0^{-1}\right)\boldsymbol{\Delta}_{p_0} + \frac{1}{2}\boldsymbol{\Delta}_{q_t} + \frac{i}{2}\gamma_t^{-1}\boldsymbol{\Delta}_{p_t}, \tag{2.3}$$

$$\frac{\partial\phi}{\partial\mathbf{q}_0} = -\frac{i}{2}\gamma_0\boldsymbol{\Delta}_{q_0} + \frac{1}{2}\boldsymbol{\Delta}_{p_0} + \frac{1}{2}\left(\mathbf{M}_{pq}^{(f)T} - i\mathbf{M}_{qq}^{(f)T}\gamma_t\right)\boldsymbol{\Delta}_{q_t} - \frac{1}{2}\left(\mathbf{M}_{qq}^{(f)T} + i\mathbf{M}_{pq}^{(f)T}\gamma_t^{-1}\right)\boldsymbol{\Delta}_{p_t}, \tag{2.4}$$

$$\frac{\partial\phi}{\partial\mathbf{p}_0} = -\frac{1}{2}\boldsymbol{\Delta}_{q_0} - \frac{i}{2}\gamma_0^{-1}\boldsymbol{\Delta}_{p_0} + \frac{1}{2}\left(\mathbf{M}_{pp}^{(f)T} - i\mathbf{M}_{qp}^{(f)T}\gamma_t\right)\boldsymbol{\Delta}_{q_t} - \frac{1}{2}\left(\mathbf{M}_{qp}^{(f)T} + i\mathbf{M}_{pp}^{(f)T}\gamma_t^{-1}\right)\boldsymbol{\Delta}_{p_t}, \tag{2.5}$$

with difference variables $\boldsymbol{\Delta}_x = \mathbf{x}' - \mathbf{x}$. The superscript labels (f) and (b) on each of the monodromy matrix elements assigns that matrix element to the forward or backward trajectory, respectively. Also in Eq. 2.2-Eq. 2.5, we used Hamilton's equations of motion, the definition of the classical action, and integration by parts to evaluate the derivatives of $S_t(\mathbf{p}_0,\mathbf{q}_0)$ and $S_{-t}(\mathbf{p}_t',\mathbf{q}_t')$. That is, for the

forward trajectory we have

$$\begin{aligned}\frac{\partial}{\partial \boldsymbol{\lambda}_0} S_t(\mathbf{p}_0, \mathbf{q}_0) =& \frac{\partial}{\partial \boldsymbol{\lambda}_0} \int_0^t d\tau\, \mathbf{p}^{\mathrm{T}} \dot{\mathbf{q}} - H, \\ =& \int_0^t d\tau\, \frac{\partial \mathbf{p}^{\mathrm{T}}}{\partial \boldsymbol{\lambda}_0} \dot{\mathbf{q}} + \mathbf{p}^{\mathrm{T}} \frac{\partial \dot{\mathbf{q}}}{\partial \boldsymbol{\lambda}_0} + \dot{\mathbf{p}}^{\mathrm{T}} \frac{\partial \mathbf{q}}{\partial \boldsymbol{\lambda}_0} - \dot{\mathbf{q}}^{\mathrm{T}} \frac{\partial \mathbf{p}}{\partial \boldsymbol{\lambda}_0} \\ =& \mathbf{p}^{\mathrm{T}} \frac{\partial \mathbf{q}}{\partial \boldsymbol{\lambda}_0} \Big|_0^t \\ =& \begin{cases} \mathbf{M}_{\mathbf{q}\boldsymbol{\lambda}}^{(f)T} \mathbf{p}_t - \mathbf{p}_0 & \boldsymbol{\lambda} = \mathbf{q} \\ \mathbf{M}_{\mathbf{q}\boldsymbol{\lambda}}^{(f)T} \mathbf{p}_t & \boldsymbol{\lambda} = \mathbf{p}. \end{cases}\end{aligned} \tag{2.6}$$

Similarly, for the backward trajectory we have

$$\begin{aligned}\frac{\partial}{\partial \boldsymbol{\lambda}'_t} S_{-t}(\mathbf{p}'_t, \mathbf{q}'_t) =& \frac{\partial}{\partial \boldsymbol{\lambda}'_t} \int_t^0 d\tau\, \mathbf{p}'^{\mathrm{T}} \dot{\mathbf{q}}' - H, \\ =& \begin{cases} \mathbf{M}_{\mathbf{q}'\boldsymbol{\lambda}}^{(b)T} \mathbf{p}'_0 - \mathbf{p}'_t & \boldsymbol{\lambda} = \mathbf{q}' \\ \mathbf{M}_{\mathbf{q}'\boldsymbol{\lambda}}^{(b)T} \mathbf{p}'_0 & \boldsymbol{\lambda} = \mathbf{p}'. \end{cases}\end{aligned} \tag{2.7}$$

Now we factor the gradient of ϕ into a matrix-vector product $\nabla\phi = \mathbf{K}\mathbf{y}$ with

$$\mathbf{K} = \begin{pmatrix} \mathbf{W} & \mathbf{X} \\ \mathbf{Y} & \mathbf{Z} \end{pmatrix}, \tag{2.8}$$

and $2N \times 2N$ matrices

$$\mathbf{W} = \begin{pmatrix} -\frac{1}{2}\left(\mathbf{M}_{pq}^{(b)T} - i\mathbf{M}_{qq}^{(b)T}\gamma_0\right) & \frac{1}{2}\left(\mathbf{M}_{qq}^{(b)T} + i\mathbf{M}_{pq}^{(b)T}\gamma_0^{-1}\right) \\ -\frac{1}{2}\left(\mathbf{M}_{pp}^{(b)T} - i\mathbf{M}_{qp}^{(b)T}\gamma_0\right) & \frac{1}{2}\left(\mathbf{M}_{qp}^{(b)T} + i\mathbf{M}_{pp}^{(b)T}\gamma_0^{-1}\right) \end{pmatrix}, \tag{2.9}$$

$$\mathbf{X} = \begin{pmatrix} \frac{i}{2}\gamma_t & -\frac{1}{2}\mathbb{I} \\ \frac{1}{2}\mathbb{I} & \frac{i}{2}\gamma_t^{-1} \end{pmatrix}, \tag{2.10}$$

$$\mathbf{Y} = \begin{pmatrix} -\frac{i}{2}\gamma_0 & \frac{1}{2}\mathbb{I} \\ -\frac{1}{2}\mathbb{I} & -\frac{i}{2}\gamma_0^{-1} \end{pmatrix}, \tag{2.11}$$

$$\mathbf{Z} = \begin{pmatrix} \frac{1}{2}\left(\mathbf{M}_{pq}^{(f)T} - i\mathbf{M}_{qq}^{(f)T}\gamma_t\right) & -\frac{1}{2}\left(\mathbf{M}_{qq}^{(f)T} + i\mathbf{M}_{pq}^{(f)T}\gamma_t^{-1}\right) \\ \frac{1}{2}\left(\mathbf{M}_{pp}^{(f)T} - i\mathbf{M}_{qp}^{(f)T}\gamma_t\right) & -\frac{1}{2}\left(\mathbf{M}_{qp}^{(f)T} + i\mathbf{M}_{pp}^{(f)T}\gamma_t^{-1}\right) \end{pmatrix}, \tag{2.12}$$

and displacement vector

$$\mathbf{y} = \begin{pmatrix} \mathbf{\Delta}_{q_0} \\ \mathbf{\Delta}_{p_0} \\ \mathbf{\Delta}_{q_t} \\ \mathbf{\Delta}_{p_t} \end{pmatrix}. \tag{2.13}$$

To simplify the Hessian of ϕ we make the following approximation

$$\begin{aligned} \frac{\partial^2 \phi}{\partial \mathbf{x}^2} \approx & \mathbf{K} \frac{\partial \mathbf{y}}{\partial \mathbf{x}} \\ = & \mathbf{K}\mathbf{J} \\ = & \mathbf{K} \begin{pmatrix} \mathbf{M}^{(b)} & -\mathbb{I} \\ \mathbb{I} & -\mathbf{M}^{(f)} \end{pmatrix}, \end{aligned} \tag{2.14}$$

where $\mathbf{M}^{(f)}$ and $\mathbf{M}^{(b)}$ are the full $2N \times 2N$ monodromy matrices for the forward and backward trajectories, respectively. In Eq. 2.14 the assumption is that the elements of $\mathbf{K}$ vary slowly with respect to the variables of integration. This is a common approximation in SC phase filtration techniques [65, 114–116]. The expression for the MFF damping factor can now be written as

$$F = \frac{\det\left[\mathbf{K}^{\mathrm{T}} + i\tilde{\mathbf{c}}^{\mathrm{T}}\mathbf{J}\right]^{\frac{1}{2}}}{\det\left[\mathbf{K}^{\mathrm{T}}\right]^{\frac{1}{2}}} e^{-\frac{1}{2}\mathbf{y}^{\mathrm{T}}\tilde{\mathbf{c}}\mathbf{y}}, \tag{2.15}$$

with $\tilde{\mathbf{c}} = \mathbf{K}^{\mathrm{T}}\mathbf{c}\mathbf{K}$. By choosing matrix $\mathbf{c}$ such that

$$\tilde{\mathbf{c}} = \begin{pmatrix} \mathbb{O} & \mathbb{O} & \mathbb{O} & \mathbb{O} \\ \mathbb{O} & \mathbb{O} & \mathbb{O} & \mathbb{O} \\ \mathbb{O} & \mathbb{O} & \mathbf{c}_q & \mathbb{O} \\ \mathbb{O} & \mathbb{O} & \mathbb{O} & \mathbf{c}_p \end{pmatrix}, \tag{2.16}$$

where both $\mathbf{c}_p$ and $\mathbf{c}_q$ are $N \times N$, diagonal, and positive semidefinite, the damping factor is now given by

$$F = \frac{\det\left[\mathbf{K}^{\mathrm{T}} + i\tilde{\mathbf{c}}^{\mathrm{T}}\mathbf{J}\right]^{\frac{1}{2}}}{\det\left[\mathbf{K}^{\mathrm{T}}\right]^{\frac{1}{2}}} e^{-\frac{1}{2}\mathbf{\Delta}_{q_t}^{\mathrm{T}}\mathbf{c}_q\mathbf{\Delta}_{q_t}} e^{-\frac{1}{2}\mathbf{\Delta}_{p_t}^{\mathrm{T}}\mathbf{c}_p\mathbf{\Delta}_{p_t}}. \tag{2.17}$$

Inserting Eq. 2.17 into DHK-IVR gives the FB MQC-IVR expression for the time-correlation function:

$$C_{AB}^{FB}(t) = \frac{1}{(2\pi)^{2N}} \int d\mathbf{p}_0 \int d\mathbf{q}_0 \int d\mathbf{p}_t' \int d\mathbf{q}_t' \, \langle \mathbf{p}_0\mathbf{q}_0|\hat{A}|\mathbf{p}_0'\mathbf{q}_0'\rangle \, \langle \mathbf{p}_t'\mathbf{q}_t'|\hat{B}|\mathbf{p}_t\mathbf{q}_t\rangle \\ \times e^{i[S_t(\mathbf{p}_0,\mathbf{q}_0)+S_{-t}(\mathbf{p}_t',\mathbf{q}_t')]} D_t^{FB}\left(\mathbf{p}_0, \mathbf{q}_0, \mathbf{p}_t', \mathbf{q}_t'; \gamma_0, \gamma_t, \mathbf{c}_p, \mathbf{c}_q\right) e^{-\frac{1}{2}\boldsymbol{\Delta}_{q_t}^{\mathrm{T}}\mathbf{c}_q\boldsymbol{\Delta}_{q_t}} e^{-\frac{1}{2}\boldsymbol{\Delta}_{p_t}^{\mathrm{T}}\mathbf{c}_p\boldsymbol{\Delta}_{p_t}}, \quad (2.18)$$

with

$$D_t^{FB}\left(\mathbf{p}_0, \mathbf{q}_0, \mathbf{p}_t', \mathbf{q}_t'; \gamma_0, \gamma_t, \mathbf{c}_p, \mathbf{c}_q\right) = C_t\left(\mathbf{p}_0, \mathbf{q}_0, \mathbf{p}_t, \mathbf{q}_t; \gamma_0, \gamma_t\right) C_{-t}\left(\mathbf{p}_t', \mathbf{q}_t', \mathbf{p}_0', \mathbf{q}_0'; \gamma_t, \gamma_0\right) \frac{\det\left[\mathbf{K}^{\mathrm{T}} + i\tilde{\mathbf{c}}^{\mathrm{T}}\mathbf{J}\right]^{\frac{1}{2}}}{\det\left[\mathbf{K}^{\mathrm{T}}\right]^{\frac{1}{2}}}. \quad (2.19)$$

See Appendix A for a simplification of Eq. 2.19 to a single $N \times N$ determinant. Also contained in Appendix A are two variations of FB MQC-IVR that reduce the dimensionality of the phase space average, depending on the definition of operator $\hat{B}$ [78].

Note the limiting behavior of Eq. 2.18:

$$\lim_{\mathbf{c}_p,\mathbf{c}_q\to 0} C_{AB}^{FB}(t) = C_{AB}^{DHK}(t), \quad (2.20)$$

$$\lim_{\mathbf{c}_p,\mathbf{c}_q\to \infty} C_{AB}^{FB}(t) = C_{AB}^{HUS}(t), \quad (2.21)$$

$$C_{AB}^{HUS}(t) = \frac{1}{(2\pi)^{N}} \int d\mathbf{p}_0 \int d\mathbf{q}_0 \, \langle \mathbf{p}_0\mathbf{q}_0|\hat{A}|\mathbf{p}_0\mathbf{q}_0\rangle \, \langle \mathbf{p}_t\mathbf{q}_t|\hat{B}|\mathbf{p}_t\mathbf{q}_t\rangle \, . \quad (2.22)$$

It is clear from Eq. 2.20 and Eq. 2.21 that FB MQC-IVR is a smooth interpolation between an ensemble average of trajectory pairs, whose phase information interferes with one another, and an ensemble average of single trajectories whose phase information is completely absent. In other words, the tuning parameters control how far trajectories are allowed to displace from one another at each time point along the trajectory. Moreover, since there are tuning parameters associated with each dof, one can choose different values of $c_{p/q}$ for different dofs and therefore control the phase contributions from each dof independently. For this reason we say that FB MQC-IVR offers mode-specific quantization [78].

Ideally one should choose $c_{p/q}$ values that strike a balance between faster convergence and desired accuracy. Unfortunately, in general systems this choice is rather arbitrary. Though Kenion-Hanrath [117] has suggested a numerical optimization approach to this problem, and though we propose yet another approach in Chapter 4 (one in which the $c_{p/q}$ parameters are completely removed), an obvious starting point is to follow Thoss et al. [65] and use smaller tuning parameters for *observed* dofs, i.e. those measured with operator $\hat{B}$, than those associated with the unobserved dofs. Numerical tests with this approach on a 2D model system showed that FB MQC-IVR can accurately describe quantum interference effects and simultaneously accelerate convergence [78].

In summary, the features of FB MQC-IVR make for a very appealing improvement upon the SC-IVR sign problem. But, as will be discussed, the methodologies presented in the remainder of this dissertation, though very similar, offer drastic improvements in efficiency and, in some cases, accuracy.

2.2 The Double-Forward Implementation

Implementing FB SC-IVR time-correlation functions involves an unfavorable quadratic scaling with respect to the effort one must make to evolve trajectories and their associated monodromy matrices. For a simulation of length $N_t\Delta t$, where N_t is the number of timesteps of length Δt, and given an initial phase space point $\mathbf{z}_0$, one first evolves $\mathbf{z}_0$ for N_t timesteps to point $\mathbf{z}_t$. Then, at the n^{th} timestep $\forall\ n \in [1, N_t]$, make a jump from $\mathbf{z}_{n\Delta t} \rightarrow \mathbf{z}'_{n\Delta t}$ and evolve $\mathbf{z}'_{n\Delta t}$ backwards in time for n timesteps to point $\mathbf{z}'_0$ [see the diagram in Fig. 2.1(a)].

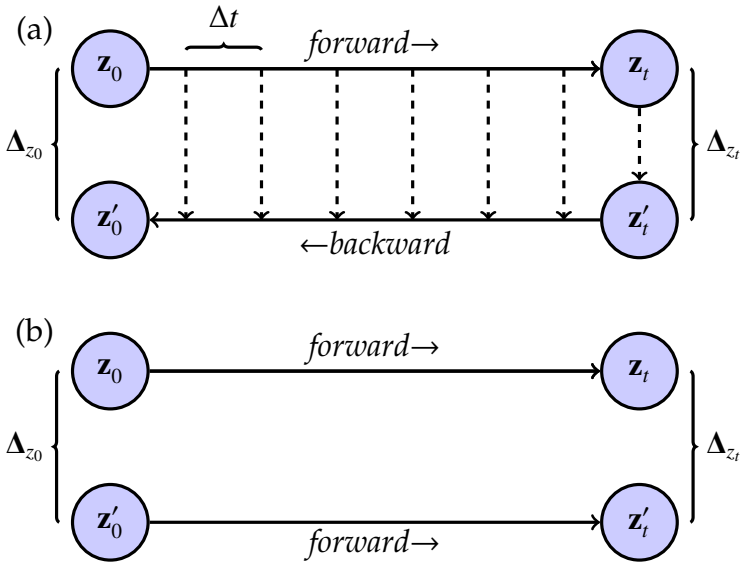

Figure 2.1: Diagrams showing the implementation strategy of (a) FB MQC-IVR and (b) MQC-IVR. In the former case, one must manually sample the phase space displacements between forward and backward trajectories at all times. In the latter case one simply propagates two forward-moving trajectories independently: a much more efficient approach.

Therefore the total number of evolution steps, $\bar{N}$, for a given trajectory pair grows quadratically with N_t:

$$\begin{aligned}\bar{N} =& N_t + \sum_{j}^{N_t} (j+1) \\ =& \frac{1}{2}N_t^2 + \frac{5}{2}N_t. \end{aligned} \tag{2.23}$$

This scaling is even more of a burden in larger systems, where the monodromy matrix becomes very large and expensive to propagate.

This unfortunate scaling of effort to evolve the system is, however, easily remedied in a framework where the unprimed and primed trajectories are propagated forward in time from points $\mathbf{z}_0$ and $\mathbf{z}'_0$ independently, respectively [see Fig. 2.1(b)]. In this framework the scaling of effort increases linearly with N_t

since

$$\bar{N} = 2N_t. \tag{2.24}$$

This offers a drastic reduction in computational expense, particularly when simulating multidimensional systems for longer timescales.

The goal now is to use MFF on DHK-IVR within this so-called "double-forward" (DF) framework in order to exploit the computational savings. The result, hereafter referred to as MQC-IVR, is mathematically similar to FB MQC-IVR, and comparably accurate to FB MQC-IVR, but drastically cheaper to compute. The derivation begins by invoking a statement of Liouville's theorem,

$$d\mathbf{p}_t' d\mathbf{q}_t' = d\mathbf{p}_0' d\mathbf{q}_0', \tag{2.25}$$

to rewrite DHK-IVR in Eq. 1.38 as a phase space average over a pair of trajectories that evolve forward in time independently:

$$\begin{aligned} C_{AB}^{DHK}(t) = &\frac{1}{(2\pi)^{2N}} \int d\mathbf{p}_0 \int d\mathbf{q}_0 \int d\mathbf{p}_0' \int d\mathbf{q}_0' \, \langle \mathbf{p}_0 \mathbf{q}_0 | \hat{A} | \mathbf{p}_0' \mathbf{q}_0' \rangle \, \langle \mathbf{p}_t' \mathbf{q}_t' | \hat{B} | \mathbf{p}_t \mathbf{q}_t \rangle \\ &\times e^{i\left[S_t(\mathbf{p}_0, \mathbf{q}_0) - S_t\left(\mathbf{p}_0', \mathbf{q}_0'\right)\right]} C_t\left(\mathbf{p}_0, \mathbf{q}_0, \mathbf{p}_t, \mathbf{q}_t; \gamma_0, \gamma_t\right) C_t^*\left(\mathbf{p}_0', \mathbf{q}_0', \mathbf{p}_t', \mathbf{q}_t'; \gamma_0, \gamma_t\right). \end{aligned} \tag{2.26}$$

In obtaining Eq. 2.26 we have also used the following relation between forward ($\mathbf{M}$) and backward ($\mathbf{M}^{(b)}$) monodromy matrices,

$$\mathbf{M}^b = (\mathbf{M})^{-1} = \begin{pmatrix} \mathbf{M}_{pp}^T & -\mathbf{M}_{qp}^T \\ -\mathbf{M}_{pq}^T & \mathbf{M}_{qq}^T \end{pmatrix} = \begin{pmatrix} \mathbf{M}_{qq}^{(b)} & \mathbf{M}_{qp}^{(b)} \\ \mathbf{M}_{pq}^{(b)} & \mathbf{M}_{pp}^{(b)} \end{pmatrix}, \tag{2.27}$$

in order to transform the HK-IVR prefactor of the primed trajectory: $C_t\left(\mathbf{p}_t', \mathbf{q}_t', \mathbf{p}_0', \mathbf{q}_0'; \gamma_t, \gamma_0\right) \rightarrow C_t^*\left(\mathbf{p}_0', \mathbf{q}_0', \mathbf{p}_t', \mathbf{q}_t'; \gamma_0, \gamma_t\right)$. We proceed as before with the MFF procedure by defining a phase function ϕ such that the zero and infinite limits of the tuning parameters yield time-correlation functions equivalent to DHK-IVR of Eq. 2.26 and Husimi-IVR of Eq. 2.22, respectively. By neglecting

the two operators as well as any phase contributions from the two HK-IVR prefactors we define ϕ as

$$\begin{aligned}\phi =& S_t(\mathbf{p}_0,\mathbf{q}_0) - S_t(\mathbf{p}_0',\mathbf{q}_0') + \frac{i}{4}(\mathbf{p}_0-\mathbf{p}_0')^{\mathrm{T}}\gamma_0^{-1}(\mathbf{p}_0-\mathbf{p}_0') + \frac{i}{4}(\mathbf{q}_0-\mathbf{q}_0')^{\mathrm{T}}\gamma_0(\mathbf{q}_0-\mathbf{q}_0')\\ &+\frac{1}{2}(\mathbf{p}_0+\mathbf{p}_0')^{\mathrm{T}}(\mathbf{q}_0-\mathbf{q}_0') + \frac{i}{4}(\mathbf{p}_t'-\mathbf{p}_t)^{\mathrm{T}}\gamma_t^{-1}(\mathbf{p}_t'-\mathbf{p}_t) + \frac{i}{4}(\mathbf{q}_t'-\mathbf{q}_t)^{\mathrm{T}}\gamma_t(\mathbf{q}_t'-\mathbf{q}_t)\\ &+\frac{1}{2}(\mathbf{p}_t'+\mathbf{p}_t)^{\mathrm{T}}(\mathbf{q}_t'-\mathbf{q}_t).\end{aligned} \tag{2.28}$$

Components of the gradient of ϕ are then given by

$$\frac{\partial\phi}{\partial\mathbf{q}_0'} = \frac{i}{2}\gamma_0\boldsymbol{\Delta}_{q_0} + \frac{1}{2}\boldsymbol{\Delta}_{p_t} + \frac{1}{2}\left(\mathbf{M}_{pq}'^{T} + i\mathbf{M}_{qq}'^{T}\gamma_t\right)\boldsymbol{\Delta}_{q_t} - \frac{1}{2}\left(\mathbf{M}_{qq}'^{T} - i\mathbf{M}_{pq}'^{T}\gamma_t^{-1}\right)\boldsymbol{\Delta}_{p_t}, \tag{2.29}$$

$$\frac{\partial\phi}{\partial\mathbf{p}_0'} = -\frac{1}{2}\boldsymbol{\Delta}_{q_0} + \frac{i}{2}\gamma_0^{-1}\boldsymbol{\Delta}_{p_0} + \frac{1}{2}\left(\mathbf{M}_{pp}'^{T} + i\mathbf{M}_{qp}'^{T}\gamma_t\right)\boldsymbol{\Delta}_{q_t} - \frac{1}{2}\left(\mathbf{M}_{qp}'^{T} - i\mathbf{M}_{pp}'^{T}\gamma_t^{-1}\right)\boldsymbol{\Delta}_{p_t}, \tag{2.30}$$

$$\frac{\partial\phi}{\partial\mathbf{q}_0} = -\frac{i}{2}\gamma_0\boldsymbol{\Delta}_{q_0} + \frac{1}{2}\boldsymbol{\Delta}_{p_0} + \frac{1}{2}\left(\mathbf{M}_{pq}^{T} - i\mathbf{M}_{qq}^{T}\gamma_t\right)\boldsymbol{\Delta}_{q_t} - \frac{1}{2}\left(\mathbf{M}_{qq}^{T} + i\mathbf{M}_{pq}^{T}\gamma_t^{-1}\right)\boldsymbol{\Delta}_{p_t}, \tag{2.31}$$

$$\frac{\partial\phi}{\partial\mathbf{p}_0} = -\frac{1}{2}\boldsymbol{\Delta}_{q_0} - \frac{i}{2}\gamma_0^{-1}\boldsymbol{\Delta}_{p_0} + \frac{1}{2}\left(\mathbf{M}_{pp}^{T} - i\mathbf{M}_{qp}^{T}\gamma_t\right)\boldsymbol{\Delta}_{q_t} - \frac{1}{2}\left(\mathbf{M}_{qp}^{T} + i\mathbf{M}_{pp}^{T}\gamma_t^{-1}\right)\boldsymbol{\Delta}_{p_t}. \tag{2.32}$$

Now factor $\nabla\phi$ into a matrix-vector product $\nabla\phi = \mathbf{K}\mathbf{y}$, with $\mathbf{K}$ given by

$$\mathbf{K} = \begin{pmatrix} \frac{i}{2}\gamma_0 & \frac{1}{2}\mathbb{I} & \frac{1}{2}\left(\mathbf{M}_{pq}'^{T} + i\mathbf{M}_{qq}'^{T}\gamma_t\right) & -\frac{1}{2}\left(\mathbf{M}_{qq}'^{T} - i\mathbf{M}_{pq}'^{T}\gamma_t^{-1}\right) \\ -\frac{1}{2}\mathbb{I} & \frac{i}{2}\gamma_0^{-1} & \frac{1}{2}\left(\mathbf{M}_{pp}'^{T} + i\mathbf{M}_{qp}'^{T}\gamma_t\right) & -\frac{1}{2}\left(\mathbf{M}_{qp}'^{T} - i\mathbf{M}_{pp}'^{T}\gamma_t^{-1}\right) \\ -\frac{i}{2}\gamma_0 & \frac{1}{2}\mathbb{I} & \frac{1}{2}\left(\mathbf{M}_{pq}^{T} - i\mathbf{M}_{qq}^{T}\gamma_t\right) & -\frac{1}{2}\left(\mathbf{M}_{qq}^{T} + i\mathbf{M}_{pq}^{T}\gamma_t^{-1}\right) \\ -\frac{1}{2}\mathbb{I} & -\frac{i}{2}\gamma_0^{-1} & \frac{1}{2}\left(\mathbf{M}_{pp}^{T} - i\mathbf{M}_{qp}^{T}\gamma_t\right) & -\frac{1}{2}\left(\mathbf{M}_{qp}^{T} + i\mathbf{M}_{pp}^{T}\gamma_t^{-1}\right) \end{pmatrix}, \tag{2.33}$$

and the same $\mathbf{y}$ as in Eq. 2.13. The Hessian of ϕ is evaluated under the same approximation as in the case of FB MQC-IVR,

$$\begin{aligned}\frac{\partial^2\phi}{\partial\mathbf{x}^2} \approx& \mathbf{K}\frac{\partial\mathbf{y}}{\partial\mathbf{x}}\\ =& \mathbf{K}\mathbf{J}\\ =& \mathbf{K}\begin{pmatrix}\mathbb{I} & -\mathbb{I}\\ \mathbf{M}' & -\mathbf{M}\end{pmatrix}.\end{aligned} \tag{2.34}$$

$\mathbf{M}$ and $\mathbf{M}'$ in Eq. 2.34 are the full $2N\times 2N$ (forward) monodromy matrices for the unprimed and primed trajectories, respectively. The matrix of tuning parameters is now chosen so that MFF is applied to the integrand at time $t = 0$ rather

than at every later point in time along the trajectory. The matrix $\tilde{\mathbf{c}}$ that facilitates this is given by

$$\tilde{\mathbf{c}} = \begin{pmatrix} \mathbf{c}_q & \mathbb{O} & \mathbb{O} & \mathbb{O} \\ \mathbb{O} & \mathbf{c}_p & \mathbb{O} & \mathbb{O} \\ \mathbb{O} & \mathbb{O} & \mathbb{O} & \mathbb{O} \\ \mathbb{O} & \mathbb{O} & \mathbb{O} & \mathbb{O} \end{pmatrix}. \tag{2.35}$$

The MFF damping factor is now given by

$$F = \frac{\det\left[\mathbf{K}^{\mathrm{T}} + i\tilde{\mathbf{c}}\mathbf{J}\right]^{\frac{1}{2}}}{\det\left[\mathbf{K}^{\mathrm{T}}\right]^{\frac{1}{2}}} e^{-\frac{1}{2}\boldsymbol{\Delta}_{q_0}^{\mathrm{T}}\mathbf{c}_q\boldsymbol{\Delta}_{q_0} - \frac{1}{2}\boldsymbol{\Delta}_{p_0}^{\mathrm{T}}\mathbf{c}_p\boldsymbol{\Delta}_{p_0}}. \tag{2.36}$$

Inserting Eq. 2.36 into Eq. 2.26 gives the MQC-IVR correlation function,

$$\begin{aligned} C_{AB}^{DF}(t) =& \frac{1}{(2\pi)^{2N}} \int d\mathbf{p}_0 \int d\mathbf{q}_0 \int d\mathbf{p}_0' \int d\mathbf{q}_0' \, \langle \mathbf{p}_0\mathbf{q}_0|\hat{A}|\mathbf{p}_0'\mathbf{q}_0'\rangle \langle \mathbf{p}_t'\mathbf{q}_t'|\hat{B}|\mathbf{p}_t\mathbf{q}_t\rangle \\ & \times D_t^{DF}\left(\mathbf{p}_0, \mathbf{q}_0, \mathbf{p}_0', \mathbf{q}_0'; \gamma_0, \gamma_t, \mathbf{c}_p, \mathbf{c}_q\right) e^{i\left[S_t(\mathbf{p}_0,\mathbf{q}_0) - S_t(\mathbf{p}_0',\mathbf{q}_0')\right]} e^{-\frac{1}{2}\boldsymbol{\Delta}_{q_0}^{\mathrm{T}}\mathbf{c}_q\boldsymbol{\Delta}_{q_0}} e^{-\frac{1}{2}\boldsymbol{\Delta}_{p_0}^{\mathrm{T}}\mathbf{c}_p\boldsymbol{\Delta}_{p_0}}, \end{aligned} \tag{2.37}$$

with prefactor

$$D_t^{DF}\left(\mathbf{p}_0, \mathbf{q}_0, \mathbf{p}_0', \mathbf{q}_0'; \gamma_0, \gamma_t, \mathbf{c}_p, \mathbf{c}_q\right) = C_t(\mathbf{p}_0, \mathbf{q}_0, \mathbf{p}_t, \mathbf{q}_t) C_t^*(\mathbf{p}_0', \mathbf{q}_0', \mathbf{p}_t', \mathbf{q}_t') \frac{\det\left[\mathbf{K}^{\mathrm{T}} + i\tilde{\mathbf{c}}\mathbf{J}\right]^{\frac{1}{2}}}{\det\left[\mathbf{K}^{\mathrm{T}}\right]^{\frac{1}{2}}}. \tag{2.38}$$

A simplification of Eq. 2.38 into an $N \times N$ determinant is provided in Appendix B.

The limiting behavior of MQC-IVR with respect to the tuning parameters is the same as its FB counter-part,

$$\lim_{\mathbf{c}_p, \mathbf{c}_q \to 0} C_{AB}^{DF}(t) = C_{AB}^{DHK}(t), \tag{2.39}$$

$$\lim_{\mathbf{c}_p, \mathbf{c}_q \to \infty} C_{AB}^{DF}(t) = C_{AB}^{HUS}(t), \tag{2.40}$$

save that the DF implementation of DHK-IVR, Eq. 2.26, is recovered on the right-hand side of Eq. 2.39 rather than the FB implementation of DHK-IVR in Eq. 1.38. The limit in Eq. 2.39 is trivial, and the limit in Eq. 2.40 is understood by first noting that

$$\lim_{\mathbf{c}_p,\mathbf{c}_q\to\infty} D_t^{DF}\left(\mathbf{p}_0,\mathbf{q}_0,\mathbf{p}_0',\mathbf{q}_0';\gamma_0,\gamma_t,\mathbf{c}_p,\mathbf{c}_q\right) e^{-\frac{1}{2}\boldsymbol{\Delta}_{q_0}^{\mathrm{T}}\mathbf{c}_q\boldsymbol{\Delta}_{q_0}} e^{-\frac{1}{2}\boldsymbol{\Delta}_{p_0}^{\mathrm{T}}\mathbf{c}_p\boldsymbol{\Delta}_{p_0}} = (2\pi)^N \delta\left(\boldsymbol{\Delta}_{p_0}\right)\delta\left(\boldsymbol{\Delta}_{q_0}\right) D^{\infty}, \tag{2.41}$$

with D^{∞} given by

$$D^{\infty} = \det\left|\frac{1}{2}\gamma_0^{-1}\left[\gamma_0\mathbf{M}_{qq}^{full} + \mathbf{M}_{pp}^{full}\gamma_0 - i\gamma_0\mathbf{M}_{qp}^{full}\gamma_0 + i\mathbf{M}_{pq}^{full}\right]\right|^{\frac{1}{2}}, \tag{2.42}$$

with $\mathbf{M}_{\alpha\beta}^{full} = \frac{\partial\boldsymbol{\alpha}_0'}{\partial\boldsymbol{\beta}_0}$ a monodromy matrix element of the full forward and backward trajectory [78]. Then, after evaluating the integrals over $\mathbf{q}_0'$ and $\mathbf{p}_0'$ in Eq. 2.37, which results in identical trajectory pairs and $\mathbf{M}_{\alpha\beta}^{full} = \delta_{\alpha\beta}\mathbb{I}$, we find that $D^{\infty} = 1$ and Eq. 2.22 is recovered.

2.3 Generalized MQC-IVR

It is possible to generalize the theories of the previous two sections into one method–one in which the displacements between trajectory pairs is tunable at all times, while retaining the computational advantage of the DF implementation. The derivation is identical to the derivation of MQC-IVR up to Eq. 2.34. We diverge from the MQC-IVR derivation by defining the following matrix of tuning parameters,

$$\tilde{\mathbf{c}} = \begin{pmatrix} \mathbf{c}_q & \mathbb{O} & \mathbb{O} & \mathbb{O} \\ \mathbb{O} & \mathbf{c}_p & \mathbb{O} & \mathbb{O} \\ \mathbb{O} & \mathbb{O} & \mathbf{c}_{q_t} & \mathbb{O} \\ \mathbb{O} & \mathbb{O} & \mathbb{O} & \mathbf{c}_{p_t} \end{pmatrix}. \tag{2.43}$$

The MFF damping factor is now given by

$$F = \frac{\det\left[\mathbf{K}^{\mathrm{T}} + i\tilde{\mathbf{c}}\mathbf{J}\right]^{\frac{1}{2}}}{\det\left[\mathbf{K}^{\mathrm{T}}\right]^{\frac{1}{2}}} e^{-\frac{1}{2}\boldsymbol{\Delta}_{q_0}^{\mathrm{T}}\mathbf{c}_q\boldsymbol{\Delta}_{q_0} - \frac{1}{2}\boldsymbol{\Delta}_{p_0}^{\mathrm{T}}\mathbf{c}_p\boldsymbol{\Delta}_{p_0}} e^{-\frac{1}{2}\boldsymbol{\Delta}_{q_t}^{\mathrm{T}}\mathbf{c}_{q_t}\boldsymbol{\Delta}_{q_t} - \frac{1}{2}\boldsymbol{\Delta}_{p_t}^{\mathrm{T}}\mathbf{c}_{p_t}\boldsymbol{\Delta}_{p_t}}. \tag{2.44}$$

Substituting Eq. 2.44 into Eq. 2.26 then gives generalized MQC-IVR (GMQC-IVR):

$$\begin{aligned} C_{AB}^{G}(t) = &\frac{1}{(2\pi)^{2N}} \int d\mathbf{p}_0 \int d\mathbf{q}_0 \int d\mathbf{p}_0' \int d\mathbf{q}_0' \, \langle \mathbf{p}_0\mathbf{q}_0|\hat{A}|\mathbf{p}_0'\mathbf{q}_0'\rangle \langle \mathbf{p}_t'\mathbf{q}_t'|\hat{B}|\mathbf{p}_t\mathbf{q}_t\rangle \\ &\times D_t^{G}\left(\mathbf{p}_0, \mathbf{q}_0, \mathbf{p}_0', \mathbf{q}_0'; \gamma_0, \gamma_t, \mathbf{c}_p, \mathbf{c}_q, \mathbf{c}_{p_t}, \mathbf{c}_{q_t}\right) e^{i\left[S_t(\mathbf{p}_0,\mathbf{q}_0) - S_t(\mathbf{p}_0',\mathbf{q}_0')\right]} \\ &\times e^{-\frac{1}{2}\boldsymbol{\Delta}_{q_0}^{\mathrm{T}}\mathbf{c}_q\boldsymbol{\Delta}_{q_0}} e^{-\frac{1}{2}\boldsymbol{\Delta}_{p_0}^{\mathrm{T}}\mathbf{c}_p\boldsymbol{\Delta}_{p_0}} e^{-\frac{1}{2}\boldsymbol{\Delta}_{q_t}^{\mathrm{T}}\mathbf{c}_{q_t}\boldsymbol{\Delta}_{q_t}} e^{-\frac{1}{2}\boldsymbol{\Delta}_{p_t}^{\mathrm{T}}\mathbf{c}_{p_t}\boldsymbol{\Delta}_{p_t}}, \end{aligned} \tag{2.45}$$

with $D_t^{G}\left(\mathbf{p}_0, \mathbf{q}_0, \mathbf{p}_0', \mathbf{q}_0'; \gamma_0, \gamma_t, \mathbf{c}_p, \mathbf{c}_q, \mathbf{c}_{p_t}, \mathbf{c}_{q_t}\right)$ given by

$$\begin{aligned} D_t^{G}\left(\mathbf{p}_0, \mathbf{q}_0, \mathbf{p}_0', \mathbf{q}_0'; \gamma_0, \gamma_t, \mathbf{c}_p, \mathbf{c}_q, \mathbf{c}_{p_t}, \mathbf{c}_{q_t}\right) = &C_t\left(\mathbf{p}_0, \mathbf{q}_0, \mathbf{p}_t, \mathbf{q}_t; \gamma_0, \gamma_t\right) C_t^{*}\left(\mathbf{p}_0', \mathbf{q}_0', \mathbf{p}_t', \mathbf{q}_t'; \gamma_0, \gamma_t\right) \\ &\times \frac{\det\left[\mathbf{K}^{\mathrm{T}} + i\tilde{\mathbf{c}}\mathbf{J}\right]^{\frac{1}{2}}}{\det\left[\mathbf{K}^{\mathrm{T}}\right]^{\frac{1}{2}}} \\ &\times e^{-\frac{1}{2}\boldsymbol{\Delta}_{q_0}^{\mathrm{T}}\mathbf{c}_q\boldsymbol{\Delta}_{q_0} - \frac{1}{2}\boldsymbol{\Delta}_{p_0}^{\mathrm{T}}\mathbf{c}_p\boldsymbol{\Delta}_{p_0}} e^{-\frac{1}{2}\boldsymbol{\Delta}_{q_t}^{\mathrm{T}}\mathbf{c}_{q_t}\boldsymbol{\Delta}_{q_t} - \frac{1}{2}\boldsymbol{\Delta}_{p_t}^{\mathrm{T}}\mathbf{c}_{p_t}\boldsymbol{\Delta}_{p_t}}. \end{aligned} \tag{2.46}$$

Though an interesting generalization of the MQC-IVR methodology, we have determined with the model systems in the following section of this chapter that GMQC-IVR does not offer any significant computational savings over MQC-IVR. However, since GMQC-IVR offers the ability to down-weight trajectory pairs that diverge over time, it may prove useful in strongly chaotic systems.

2.4 Numerical Tests

Here we apply MQC-IVR to two model systems. Model 1 of this chapter is a 1D anharmonic oscillator with Hamiltonian

$$H = \frac{1}{2}p^2 + x^2 - 0.1x^3 + 0.1x^4. \tag{2.47}$$

The initial state of the system is taken to be a shifted coherent state, whose position space wavefunction is given by

$$\langle x|p_i q_i\rangle = \mathcal{N} e^{-\frac{\gamma}{2}(x-q_i)^2 + i p_i (x-q_i)}, \tag{2.48}$$

with $q_i = 1$, $p_i = 0$, $\gamma = \sqrt{2}$, and $\mathcal{N}$ for normalization. Operator $\hat{A}$ is taken to be a projector of the initial state,

$$\hat{A} = |p_i q_i\rangle \langle p_i q_i| . \tag{2.49}$$

Following Pan and Tao [118] we sample initial conditions from a correlated distribution,

$$\rho\left(\bar{p}, \bar{q}, \Delta_p, \Delta_q\right) = \bar{\mathcal{N}} \left|\langle \bar{p}\bar{q}|p_i q_i\rangle\right| e^{-\frac{c_q}{2}\Delta_q^2} e^{-\frac{c_p}{2}\Delta_p^2}, \tag{2.50}$$

with $\bar{\mathcal{N}}$ for normalization, and the bars represent mean variables,

$$\bar{p} = \frac{1}{2}\left(p_0' + p_0\right) \tag{2.51}$$

$$\bar{q} = \frac{1}{2}\left(q_0' + q_0\right). \tag{2.52}$$

We also take $\hat{B} = \hat{x}$ to compute the average position of the oscillator as a function of time. The coherent state matrix element of $\hat{x}$ is given by

$$\langle p_t' q_t'|\hat{x}|p_t q_t\rangle = \frac{1}{2\gamma}\left[\gamma\left(q_t' + q_t\right) - i\left(p_t' - p_t\right)\right]\langle p_t' q_t'|p_t q_t\rangle . \tag{2.53}$$

Model 2 contains the same anharmonic oscillator of model 1 but now linearly coupled to a heavier harmonic bath mode. The Hamiltonian is

$$H = \frac{1}{2}p_x^2 + \frac{1}{2m}p_y^2 + x^2 - 0.1x^3 + 0.1x^4 + \frac{1}{2}m\omega^2 y^2 + kxy, \tag{2.54}$$

with $m = 25.0$, $\omega = 1/3$, and $k = 1.5$. The initial state is taken to be a product of shifted coherent states, of which the position space wavefunction is

$$\langle \mathbf{x}|\mathbf{p_i q_i}\rangle = \prod_u \left(\frac{\gamma_u}{\pi}\right)^{\frac{1}{4}} e^{-\frac{\gamma_u}{2}(u-q_{iu})^2 + i p_{iu}(u-q_{iu})}, \tag{2.55}$$

with vector $\mathbf{x} = (x, y)$, $u \in (x, y)$, and with $\gamma_x = \sqrt{2}$ as before, $\gamma_y = m\omega$, and $q_{ix} = q_{iy} = 1.0$, and $p_{ix} = p_{iy} = 0.0$. The multidimensional form of Eq. 2.53 is given by

$$\langle \mathbf{p}_t' \mathbf{q}_t' | \hat{u} | \mathbf{p}_t \mathbf{q}_t \rangle = \frac{1}{2\gamma_u} \left[\gamma_u \left(q_{tu}' + q_{tu} \right) - i \left(p_{tu}' - p_{tu} \right) \right] \langle \mathbf{p}_t' \mathbf{q}_t' | \mathbf{p}_t \mathbf{q}_t \rangle \,. \tag{2.56}$$

The position expectation value of the anharmonic oscillator of model 1 is plotted in Fig. 2.2. The MQC-IVR results in Fig. 2.2 are obtained with $c = c_p = c_q$.

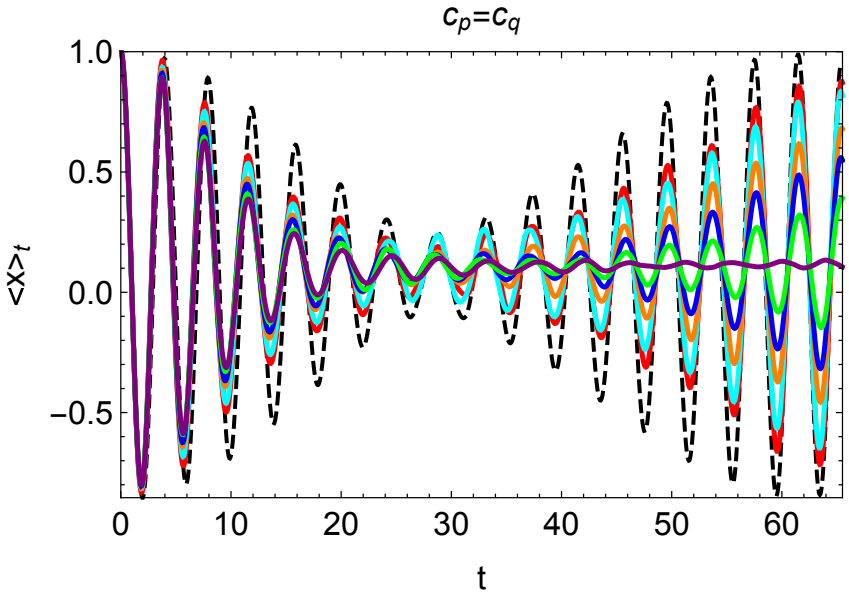

Figure 2.2: The average position of the anharmonic oscillator as a function of time, as computed with MQC-IVR and $c = c_p = c_q = 0.7$ (red), 1.0 (cyan), 3.0 (orange), 5.0 (blue), 10.0 (green), and 100.0 (purple). Husimi-IVR (yellow) is hidden behind the purple MQC-IVR result. The exact quantum result (black, dashed) is included as well.

The amplitude of the classical time-correlation function in Fig. 2.2 is clearly damped relative to the exact quantum result, particularly at longer times. One can rationalize this difference in terms of constructive and destructive interference between the complex expansion coefficients of the quantum mechan-

ical wavepacket, or, equivalently, in terms of constructive and destructive interference between phase contributions from forward and backward paths of the Feynman path integral. In the classical limit, on the other hand, where forward and backward paths lie along an identical trajectory, phase information is canceled along with any interference effects. It is clear from Fig. 2.2 that MQC-IVR smoothly interpolates between the classical and quantum limits of the time-correlation function. The quantum mechanical character of the time-correlation function is well-described when the tuning parameters are close to zero, and MQC-IVR is damped to the classical result when the tuning parameters are much further from zero.

In Table 2.1 we compare the total CPU time needed to compute the position expectation value of the anharmonic oscillator with the DF and FB implementations of MQC-IVR. The same tuning parameter $c = c_p = c_q = 0.7$ is used in each simulation.

Implementation	CPU Time /seconds
DF	2
FB	288

Table 2.1: A comparison of CPU time to calculate the MQC-IVR position correlation function with the DF and FB implementations and $c = c_p = c_q = 0.7$.

Table 2.1 shows that, for the 1D model system considered here, the DF implementation is more than 100× faster than the FB implementation. In simulations involving more dofs and longer timescales than are used here, we expect the computational savings to grow even further.

In Fig. 2.3 we plot the same position expectation value as in Fig. 2.2 but with different combinations of c_p and c_q parameters.

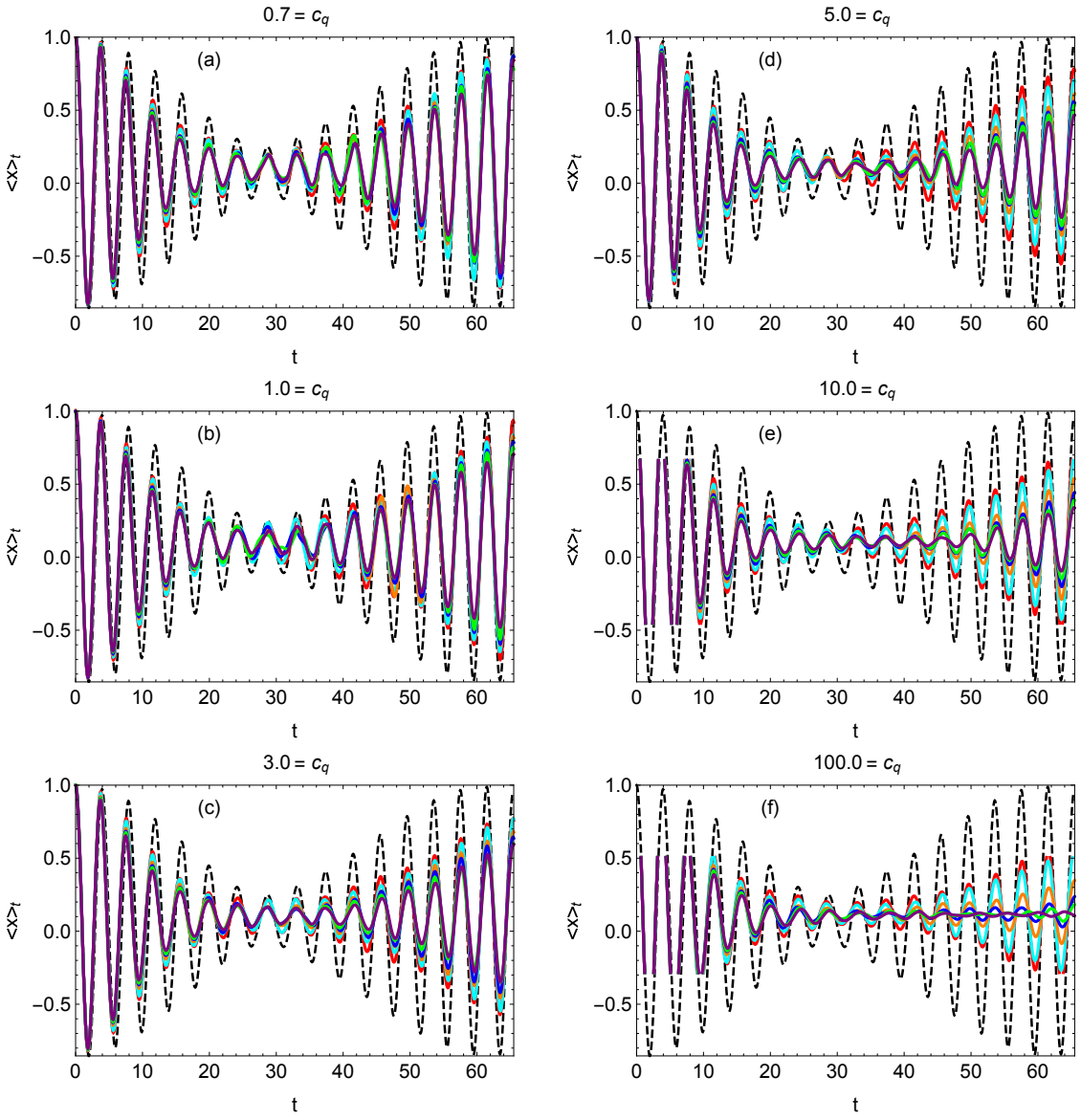

Figure 2.3: The average position of the anharmonic oscillator as a function of time, as computed with MQC-IVR. Different combinations of c_p and c_q are used in each case. Within each panel c_q is held fixed, as indicated in the label. The value of c_p is determined by the color of each curve: c_p = 0.7 (red), 1.0 (cyan), 3.0 (orange), 5.0 (blue), 10.0 (green), and 100.0 (purple).

As expected, the general trend is that larger values of c_p or c_q, with the other held fixed, yields a result that is more damped than otherwise. The interesting

feature of Fig. 2.3 is, however, found in panel (a). MQC-IVR with a small position tuning parameter, $c_q = 0.7$, is not particularly sensitive to changes in c_p, even when c_p is pushed as high as $c_p = 100$. This trend could be due to the fact that the observable $\hat{B}$ is strictly a function of the position operator, and therefore MQC-IVR should be more sensitive to changes in position displacements between trajectory pairs rather than changes in momentum displacements. It is also possible that this trend is dependent upon the initial state of the system as defined in operator $\hat{A}$. However in model 1 the initial state is a coherent state whose width parameter is chosen under a harmonic approximation, $\gamma = m\omega$. This means that the initial wavepacket is equally dispersed in position and momentum space, and so it is unclear how operator $\hat{A}$ could influence this trend. In any case, this analysis suggests that the c_p and c_q parameters of MQC-IVR can be varied independently to facilitate faster convergence (see below) without a significant loss of accuracy.

We have shown that MQC-IVR can smoothly tune between quantum and classical limits of SC theory, but the practical advantage of the method resides in its computational savings. Table 2.2 shows the number of trajectories required to converge MQC-IVR with different combinations of c_p and c_q parameters.

		c_p					
		0.7	1.0	3.0	5.0	10.0	100.0
c_q	0.7	18.0	12.0	10.0	13.0	12.0	11.0
	1.0	14.0	12.0	11.0	15.0	10.0	9.0
	3.0	11.0	7.0	6.0	6.0	6.0	6.0
	5.0	6.0	5.0	3.0	4.0	4.0	5.0
	10.0	7.0	5.0	4.0	3.0	4.0	3.0
	100.0	5.0	4.0	3.0	2.0	3.0	1.0

Table 2.2: The number of trajectory pairs ($\times 10^{-3}$) required to converge an MQC-IVR simulation of model 1 in time $t = 55$ as a function of c_p and c_q tuning parameters.

The general trend in Table 2.2, as expected, is that less computational expense is required with larger tuning parameters. But in some cases, namely in the upper left-hand corner of the table, the decrease in expense does not coincide with a significant loss of accuracy, as compared with the previous two figures. It is also interesting to note that the convergence of $\langle \hat{x} \rangle_t$ is more sensitive to changes in c_q than changes to c_p, lending to the observation in the previous paragraph. For example, more than twice the effort is needed to converge $c_q = 0.7$, $c_p = 100.0$ than to converge when the two values are swapped. This suggests that the phase information as a result of position displacements has a larger contribution to the integral than the phase information from momentum displacements, and that c_p can be assigned a larger value than c_q without a significant loss of accuracy.

The position expectation values of both the anharmonic and harmonic modes of model 2 are plotted in Fig. 2.4. The MQC-IVR results are obtained with equal tuning parameters for each dof: $c = c_{p_x} = c_{q_x} = c_{p_y} = c_{q_y}$.

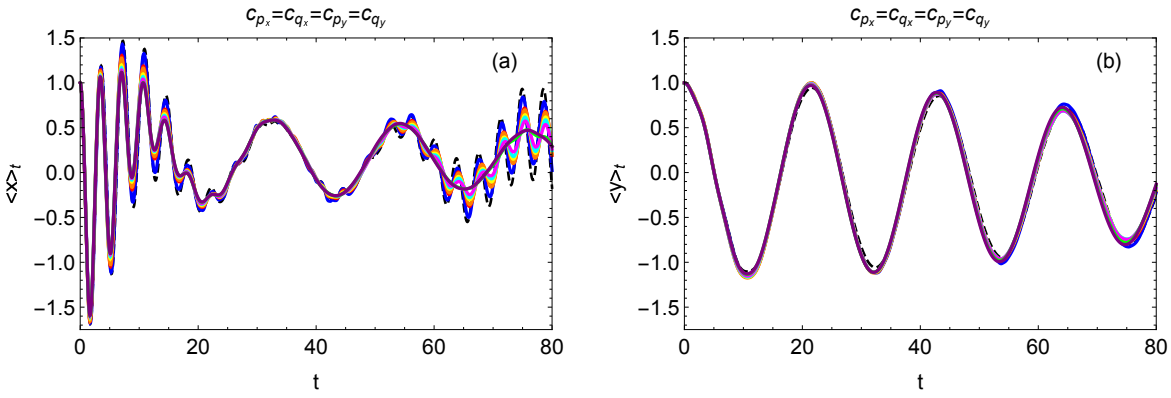

Figure 2.4: The expectation value of (a) $\langle \hat{x} \rangle_t$ and (b) $\langle \hat{y} \rangle_t$ as a function of time as computed with exact quantum (black, dashed) and MQC-IVR with all tuning parameters set to the same value $c = c_{p_x} = c_{q_x} = c_{p_y} = c_{q_y}$: $c = 0.1$ (blue), $c = 0.7$ (red), $c = 1.0$ (orange), $c = 3.0$ (yellow), $c = 5.0$ (cyan), $c = 10.0$ (magenta), $c = 50.0$ (green), and $c = 100.0$ (purple). The Husimi-IVR result (gold) is beneath the classical limit MQC-IVR result.

As seen with model 1, the long-time recurring oscillations in the exact quantum result are due to interference effects, and are therefore absent in the classical limit result. As with model 1 we see that MQC-IVR smoothly interpolates between the quantum and classical results. Note that the classical and quantum limits of the the harmonic mode $\langle \hat{y} \rangle_t$ are nearly identical, which is expected since classical, SC, and quantum correlation functions of the harmonic oscillator are equal, and since the coupling is not strong enough to significantly perturb the motion of the heavier oscillator.

In Fig. 2.5 and Fig. 2.6 we plot the same expectation values as in Fig. 2.4, but with the anharmonic mode fixed near the quantum limit in the former case, and the harmonic mode fixed near the quantum limit in the latter case.

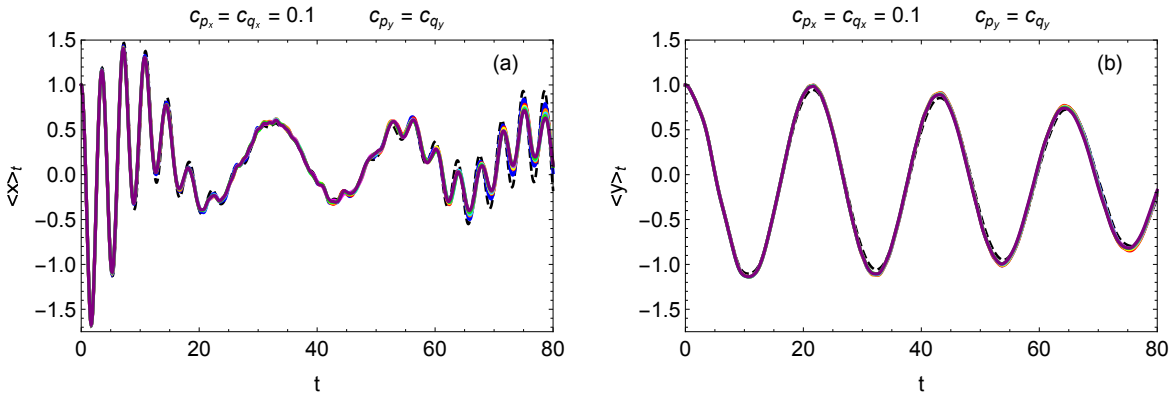

Figure 2.5: The expectation value of (a) $\langle \hat{x} \rangle_t$ and (b) $\langle \hat{y} \rangle_t$ as a function of time as computed with exact quantum (black, dashed) and MQC-IVR with the anharmonic mode fixed near the quantum limit, $c_{p_x} = c_{q_x} = 0.1$, and the harmonic mode treated with different values of $c = c_{p_y} = c_{q_y}$: $c = 0.1$ (blue), $c = 0.7$ (red), $c = 1.0$ (orange), $c = 3.0$ (yellow), $c = 5.0$ (cyan), $c = 10.0$ (magenta), $c = 50.0$ (green), and $c = 100.0$ (purple). The Husimi-IVR result (gold) is beneath the classical limit MQC-IVR result.

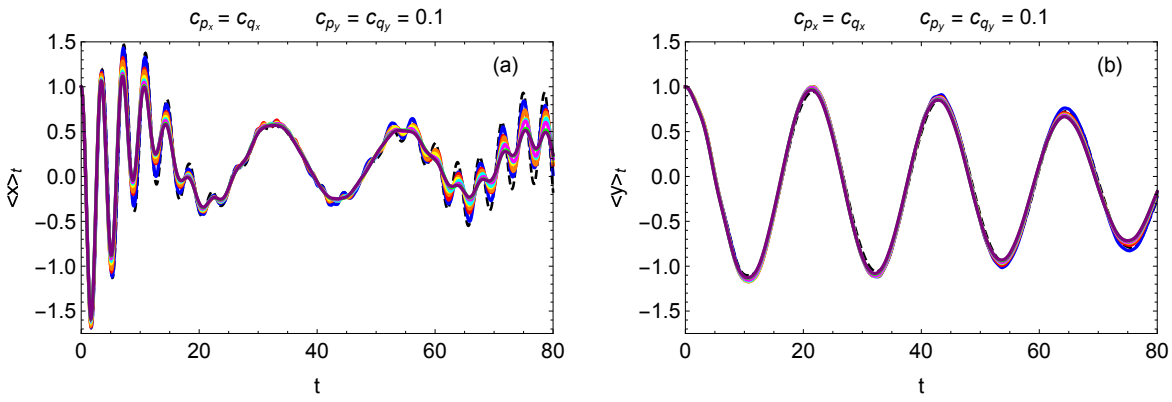

Figure 2.6: The expectation value of (a) $\langle \hat{x} \rangle_t$ and (b) $\langle \hat{y} \rangle_t$ as a function of time as computed with exact quantum (black, dashed) and MQC-IVR with the harmonic mode fixed near the quantum limit, $c_{p_y} = c_{q_y} = 0.1$, and the anharmonic mode treated with different values of $c = c_{p_x} = c_{q_x}$: $c = 0.1$ (blue), $c = 0.7$ (red), $c = 1.0$ (orange), $c = 3.0$ (yellow), $c = 5.0$ (cyan), $c = 10.0$ (magenta), $c = 50.0$ (green), and $c = 100.0$ (purple). The Husimi-IVR result (gold) is beneath the classical limit MQC-IVR result.

We see from Fig. 2.5(a) the appealing result that, when the anharmonic mode is both observed by operator $\hat{B}$ and fixed near the quantum limit with a small tuning parameter, the position expectation value $\langle \hat{x} \rangle_t$ is insensitive to changes in the tuning parameter of the heavier harmonic mode, which is not observed by operator $\hat{B}$. There is a slight damping effect in the MQC-IVR amplitudes of Fig. 2.5(a) at longer times when the value of $c = c_{p_y} = c_{q_y}$ is increased, but the quantum mechanical features are still clearly captured.

As should therefore be expected, we see in Fig. 2.6(a) that, when the anharmonic mode is both observed by operator $\hat{B}$ and treated increasingly closer to the classical limit with larger tuning parameters, the position expectation value $\langle \hat{x} \rangle_t$ is more sensitive to changes in the tuning parameter of the anharmonic mode. Some of the oscillatory features are still captured with, say, $c_{p_x} = c_{q_x} = 100$

in Fig. 2.6(a), but the damping effect is much more significant than in Fig. 2.5(a). This analysis clearly supports the main objective of the MQC-IVR methodology, that the tuning parameters of individual dofs in a multidimensional system can be varied independently to facilitate faster convergence (see below) without a significant loss of accuracy.

Also as expected, we see in Fig. 2.5(b) and Fig. 2.6(b) that the position expectation value of the harmonic mode is fairly insensitive to changes in any of the tuning parameters. With a more strongly coupled system, however, as was studied by Antipov et al. [78] to test FB MQC-IVR, we expect a similar conclusion to that of the previous paragraph.

In Table 2.3 we report the number of trajectory pairs required to converge the MQC-IVR position expectation value of the anharmonic mode with different sets of tuning parameters.

		c_x							
		0.1	0.7	1.0	3.0	5.0	10.0	50.0	100.0
c_y	0.1	29	6.3	8.3	2.2	2.0	2.6	1.8	0.86
	0.7	20	3.1	x	x	x	x	x	x
	1.0	12	x	2.2	x	x	x	x	x
	3.0	7.1	x	x	1.2	x	x	x	x
	5.0	4.5	x	x	x	0.54	x	x	x
	10.0	3.8	x	x	x	x	0.25	x	x
	50.0	7.6	x	x	x	x	x	0.1	x
	100.0	2.7	x	x	x	x	x	x	0.07

Table 2.3: The number of trajectory pairs required for convergence ($\times 10^{-5}$) of $\langle \hat{x} \rangle_t$ under each filtering parameter regime depicted in the previous three figures. Note that $c_x = c_{p_x} = c_{q_x}$ and $c_y = c_{p_y} = c_{q_y}$.

As expected, Table 2.3 shows that an increase in any of the tuning parameters results in less computational expense. The most appealing result of Table 2.3

is, however, found in the first column. Note that the number of trajectories required for convergence drops by more than an order of magnitude in going from $c_y = 0.1$ to $c_y = 100.0$. As compared with Fig. 2.5(a), this drop in computational expense does not coincide with a significant loss of accuracy.

In summary, we have shown that MQC-IVR is capable of both tuning between the quantum and classical limits of the DHK-IVR time-correlation function, and capable of treating different modes of multidimensional systems in different limits to facilitate faster convergence and preserve accuracy. We have also shown that the DF implementation offers a drastic reduction in computational expense as compared to the FB implementation. Finally, we have shown that, for individual dofs, c_p and c_q parameters can also be varied independently to facilitate faster convergence without a significant loss of accuracy.

CHAPTER 3

VALIDATING THE MFF APPROXIMATION

Though Filinov filtration [88] and its modifications [62, 89, 119] have shown promise in accelerating the convergence of oscillatory integrals, namely of the SC-IVR variety [55, 65, 78, 81, 82, 115, 116, 120–122], MFF is the essential approximation of the methods presented in this dissertation, and it is therefore worth our scrutiny. In this chapter we attempt to validate MFF as an extremely powerful theoretical and practical tool for the computation of the DHK-IVR time-correlation function [81]. The motivation of this analysis is driven further by a study from Spanner et al. [123], who examined the phase and amplitude contributions from single trajectories of the HK-IVR wavepacket, and concluded that MFF is generally not particularly effective in the context of HK-IVR wavepacket evolution. However, the phase information in the SC-IVR time-correlation function is significantly different than the phase information contained in the SC-IVR wavepacket; the quantum mechanical character of the SC-IVR time-correlation function arises from interference between the phases of forward-backward trajectory pairs [78, 81] (the double phase space average), a feature that is absent in the single phase space average of the SC-IVR wavepacket. In this chapter we begin by briefly reviewing the analysis of Spanner et al. [123], and then proceed to conduct a similar analysis on the SC-IVR time-correlation function that validates MFF as an extremely effective approximation (as it is made in the methods of this dissertation).

Here we use the 1D model system of the Chapter 2; the Hamiltonian, initial state, and time-dependent observable of which are provided in Eq. 2.47, Eq. 2.48, and Eq. 2.53, respectively. We use the same simulation parameters as

in the previous chapter as well. Following Spanner et al. [123] we begin by considering the phase and amplitude contributions to the time-dependent HK-IVR wavepacket,

$$\Psi(x,t) = \frac{1}{2\pi}\int dq_0 \int dp_0\, C_t(p_0,q_0,p_t,q_t;\gamma_0,\gamma_t)\, e^{iS_t(p_0,q_0)}\, \langle x|p_t q_t\rangle \langle p_0 q_0|p_i q_i\rangle\,, \quad (3.1)$$

from individual trajectories. In Fig. 3.1 we plot the phase ϕ and amplitude A of the entire integrand in Eq. 3.1 for fixed $x = 0.5$ at time $t = 7.5$ as a function of the trajectories' initial position q_0 and the initial momentum p_0.

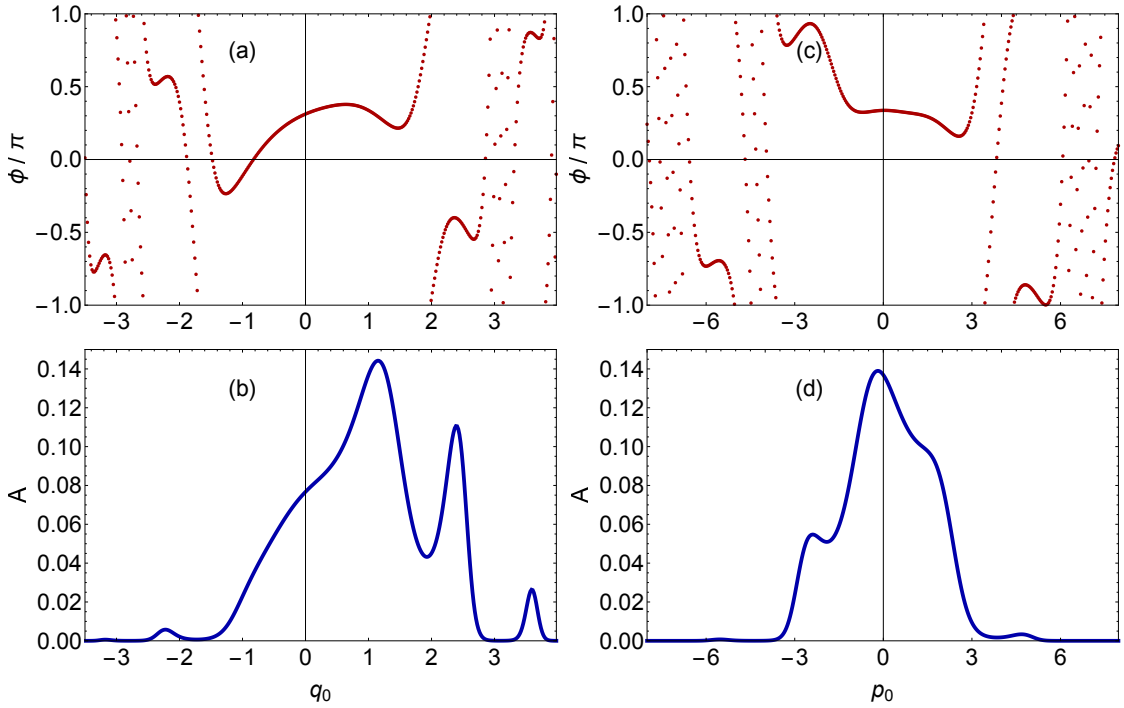

Figure 3.1: The (a) phase and (b) amplitude of the HK-IVR wavepacket integrand as a function of the trajectories' initial position q_0 with fixed $p_0 = 0.0$. Also plotted is the (c) phase and (d) amplitude of the integrand as a function of the trajectories' initial momentum p_0 with fixed $q_0 = 1.0$. In each case we fix the wavepacket position $x = 0.5$ and time $t = 7.5$.

The notable feature of Fig. 3.1, in comparing the phase and amplitude

in Fig. 3.1(a) and Fig. 3.1(b), and in comparing the phase and amplitude in Fig. 3.1(c) and Fig. 3.1(d), is that the most oscillatory regions of phase predominantly overlap with regions of negligibly small amplitude. This is notable because the general purpose of MFF is to down-weight contributions to the integral where the phase oscillates the quickest. Fig. 3.1 suggests, however, that the regions of phase space in the HK-IVR wavepacket integrand where the phase ϕ changes the quickest have a negligible contribution to the integral. We are therefore led to question to effectiveness of implementing MFF to an integral such as in Eq. 3.1 [123].

We now follow Spanner et al. [123] to conduct a similar analysis on the SC-IVR time-correlation function, and draw a more optimistic conclusion on the effectiveness of MFF in the context of the methods presented in this study. Before the analysis, however, it is worth noting that we have already established in Chapter 2, and in previous work by Antipov et al. [78] and Thoss et al. [65], that MFF is a powerful theoretical tool for interpolating between existing limits of SC-IVR theory. The infinite limit of the tuning parameters in MQC-IVR (and its variations) and in GFB-IVR [65] give rise to well-defined, theoretically-sound time-correlation functions (Husmi-IVR in the former case, and FB-IVR in the latter), whereas a stationary phase approximation to the HK-IVR wavepacket in Eq. 3.1 does not, as far as the author can discern, give rise to an approximate wavepacket that is particularly useful or convenient to implement. Therefore, from a theoretical standpoint, we can conclude that MFF is an informative approximation to the SC-IVR time-correlation function. In the proceeding paragraph we show that MFF is, in addition, an extremely practical approximation to the SC-IVR time-correlation function as well.

As it is implemented in the derivation of MQC-IVR and variations thereof, the purpose of MFF is to provide a handle over the extent to which trajectory pairs displace from one another over the course of the simulation. We therefore proceed by examining the contributions to the MQC-IVR time-correlation function from individual trajectory pairs as a function of the displacements between them.

In Fig. 3.2 we plot the phase and amplitude of the integrand of the FB MQC-IVR time-correlation function for the 1D model system [78],

$$\langle \hat{x} \rangle_t = \frac{1}{(2\pi)^2} \int dp_0 \int dq_0 \int d\Delta_{p_t} \langle p_0 q_0 | p_i q_i \rangle \langle p_i q_i | p_0' q_0' \rangle \, e^{i[S_t(p_0,q_0)+S_{-t}(\mathbf{p}_t',\mathbf{q}_t')]} \times \bar{D}_t^{FB}\left(p_0, q_0, \Delta_{p_t}; c_p\right) q_t e^{-\frac{c_p}{2}\Delta_{p_t}^2}, \tag{3.2}$$

as a function of the momentum displacement Δ_{p_t} between the trajectory pairs at time t, and with different values of the tuning parameter c_p. Operationally, we choose a trajectory that originates at the center of the initial wavepacket, $q_0 = 1.0$ and $p_0 = 0.0$, propagate that trajectory for time $t = \tau$, make a jump in momentum from $p_\tau \rightarrow p_\tau' = p_\tau + \Delta_{p_\tau}$, and propagate the resulting phase space point backwards in time to $t = 0$. We then use each trajectory pair to compute and plot the phase and amplitude of the integrand in Eq. 3.2 as a function of Δ_{p_τ} in Fig. 3.2 for two different times τ. The times τ at which we compute the integrand are times at which the quantum and classical correlation functions give significantly different results.

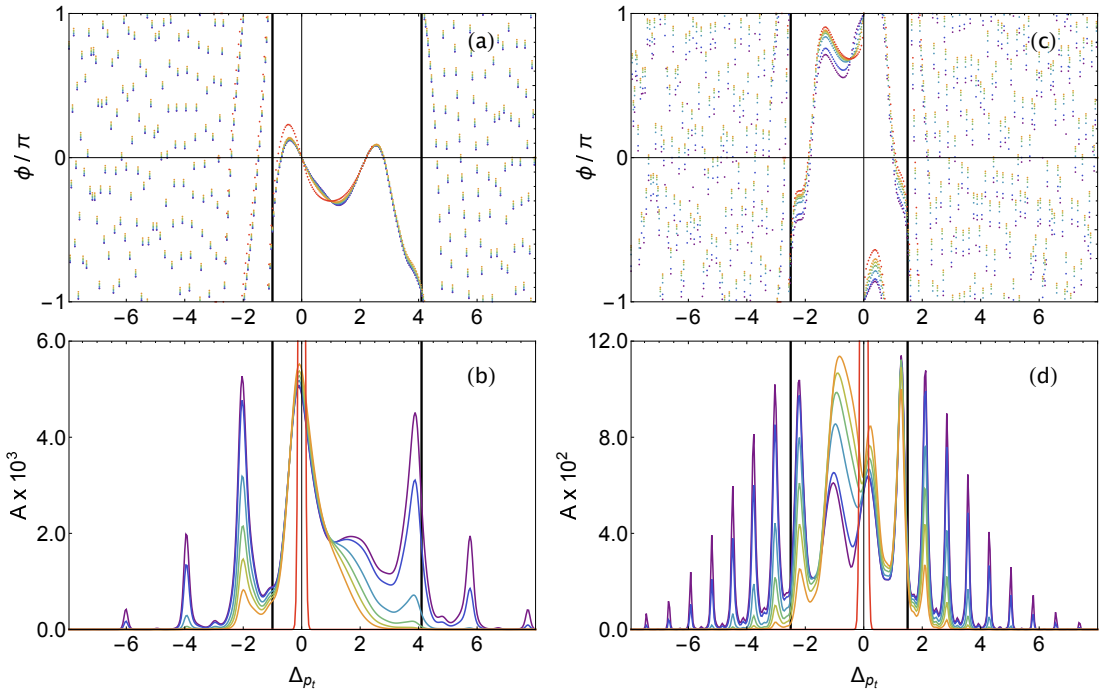

Figure 3.2: The phase and amplitude of the FB MQC-IVR integrand as a function of the momentum displacement between trajectory pairs at time (a-b) $t = 22$ and (c-d) $t = 61$. The color of each curve corresponds to a different choice of tuning parameter c_p, which varies from $c_p = 10^{-4}$ (purple) to $c_p = 200.0$ (red). The black vertical gridlines enclose the least oscillatory region of the integrand.

Consider the phase corresponding to the momentum jump value $\Delta_{p_t} = 0$ in Fig. 3.2(a) and Fig. 3.2(c). At this point, the forward and backward trajectories coincide and the net phase is zero (or $\pm\pi$ due to a phase contribution from operator $\hat{B}$) – these are the trajectory pairs that contribute to the classical-limit Husimi-IVR correlation function in Eq. 2.22, as indicated by the narrow red ($c_p = 200$) peak in the corresponding amplitude plots in Fig. 3.2(b) and Fig. 3.2(d). As the magnitude of Δ_{p_t} increases, the path of the forward and backward trajectories become significantly different, resulting in a net non-zero phase contribution that varies rapidly with small changes in momentum jump. Although the re-

gions of slowly varying phase in Fig. 3.2(a) and Fig. 3.2(c) (enclosed within solid black lines) are relatively invariant to the choice of c_p values, as we go from low c_p values that describe quantum-limit behavior to high c_p values for classical-limit behavior, the amplitude changes significantly, approaching zero for large values of Δ_{p_t}. Our analysis of MFF based on individual trajectory pairs thus suggests that we can eliminate contributions from regions of highly oscillatory phase, $|\Delta_{p_t}| \geq 3$ in both Fig. 3.2(a) and Fig. 3.2(c).

Next we analyze the amplitude and phase of an average integrand obtained by summing over contributions from an ensemble of forward-backward trajectory pairs to verify that, as we approach numerical convergence, regions of highly oscillatory phase do, in fact, have a negligible contribution to the ensemble average time-correlation function. Using a weak filter (quantum-limit, $c_p = 0.05$) and simulation time $t = 22$ a.u., we plot the average phase of the MQC-IVR integrand in Fig. 3.3(a) as a function of the momentum jump.

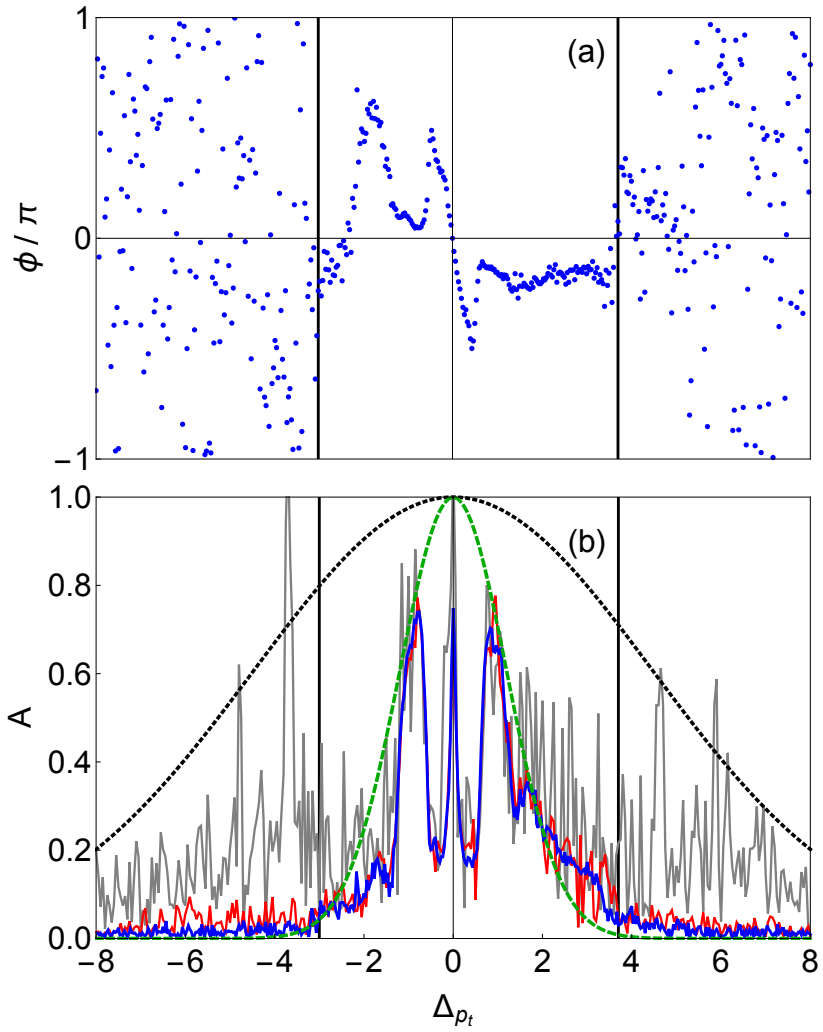

Figure 3.3: The (a) phase and (b) amplitude of the MQC-IVR position correlation function against the momentum displacement between forward-backward trajectories at t = 22 a.u. in the quantum limit, as averaged over 1.2×10^3 trajectories (gray), 6.0×10^4 trajectories (red), and 2.4×10^5 trajectories (blue). The black-dashed Gaussian represents a weak filter strength (c_p = 0.05) while the green-dashed Gaussian represents an optimal filter strength (c_p = 0.7).

In Fig. 3.3(a) we find a region of slowly varying phase corresponding to the region −4 a.u.$\leq \Delta_{p_t} \leq$ 4 a.u (enclosed between two vertical black lines). The average amplitude is plotted in Fig. 3.3(b); we find that as the number of tra-

jectories included in the ensemble average is increased, the amplitude vanishes in regions of highly oscillatory phase. Taken together, these observations suggest that trajectory pairs with Δ_{p_t} values outside the slowly varying phase zone ($|\Delta_{p_t}| \geq 4$ a.u.) contribute very little to the overall time-correlation function and make it difficult to achieve numerical convergence. This makes a strong case for the use of MFF to increase computational efficiency – for instance, with a stronger filter, say $c_p = 0.7$ [green Gaussian in Fig. 3.3(b)], it becomes possible to explicitly exclude trajectory pairs that contribute only noise by making the amplitude zero. In fact, it was shown in Fig. 2.2 of the previous chapter that an MQC-IVR simulation employing $c = 0.7$ does indeed recover quantum mechanical features in the position correlation function at long times, and with significantly fewer trajectories than is needed in DHK-IVR: 3×10^6 are needed for DHK-IVR and only 1.8×10^4 are needed for MQC-IVR with $c = 0.7$.

CHAPTER 4

THE ANALYTICAL MQC LIMIT

4.1 Motivation and Derivation

An existing challenge with MQC-IVR is determining the optimal set of $2N$ tuning parameters such that both computational cost and loss of quantum mechanical accuracy are minimized. Without a systematic procedure to address this challenge the choice of tuning parameters is rather arbitrary, and refined only by trial and error. We have seen in Chapter 3 that computing the integrand of MQC-IVR as a function of the trajectory pair displacement variables can inform this choice, and Kenion-Hanrath [117] has suggested a promising numerical optimization procedure, but the former option is hardly systematic, and both options may be difficult (particularly the former) to implement in multidimensional systems.

The biggest problem in trying to envision a numerical optimization procedure that minimizes error with respect to changes in the tuning parameters is that, in terms of accuracy alone, the optimal choice of tuning parameter is already known to be zero for all dofs. And the choice of zero for each tuning parameter, of course, leads to DHK-IVR which is generally computationally intractable. Therefore, since the correlation between accuracy and computational cost is not well-defined, an efficient numerical optimization procedure would be difficult to devise.

Yet another approach to this challenge, and the subject of this chapter, is to choose a subset of dofs to be treated in the quantum limit and evaluate

MQC-IVR analytically in the limit that the tuning parameters associated with the quantum dofs go to zero, and the limit that the tuning parameters associated with the remaining classical dofs go to infinity. The result, which we call analytical MQC-IVR (AMQC-IVR), treats each dof in the extreme classical or quantum limits of MQC-IVR theory, and the burden of having to choose a set of $2N$ tuning parameters is removed. In addition, as we will see, AMQC-IVR is the starting point for a variety of additional approximations that could prove extremely useful when simulating complex molecular systems.

We now proceed to the derivation of AMQC-IVR. First, as a matter of bookkeeping, we consider a general system consisting of N dofs, F of which will be treated in the quantum limit, and $N - F$ of which will be treated in the classical limit. We also order all vectors and matrices in this chapter so that the elements associated with the quantum dofs are listed before the elements associated with the classical dofs.

The derivation starts by considering the $\mathbf{c}$-dependence of the MQC-IVR integrand,

$$G_t\left(\mathbf{z}_0, \mathbf{z}_0'; \mathbf{c}\right) = D_t^{DF}\left(\mathbf{z}_0, \mathbf{z}_0'; \mathbf{c}\right) e^{-\frac{1}{2}\boldsymbol{\Delta}^{\mathrm{T}}\mathbf{c}\boldsymbol{\Delta}}, \tag{4.1}$$

with $D_t^{DF}\left(\mathbf{z}_0, \mathbf{z}_0'; \mathbf{c}\right)$ provided in Eq. 2.38, and a $2N$-dimensional collective phase space displacement vector given by

$$\boldsymbol{\Delta} = \begin{pmatrix} \boldsymbol{\Delta}_{\mathbf{q}} \\ \boldsymbol{\Delta}_{\mathbf{p}} \end{pmatrix}. \tag{4.2}$$

We now evaluate Eq. 4.1 in the limit that the tuning parameters associated with the quantum dofs go to zero, and the limit that the tuning parameters associated with the remaining classical dofs go to infinity. Using the following δ-function

identity for the classical dofs,

$$\delta(x) = \lim_{a\to\infty} \left(\frac{a}{\pi}\right)^{\frac{1}{2}} e^{-\frac{a}{2}x^2}, \tag{4.3}$$

the limit is given by

$$\lim_{\substack{c_{\text{quantum}}\to 0 \\ c_{\text{classical}}\to\infty}} G_t(\mathbf{z}_0, \mathbf{z}_0'; \mathbf{c}) = (2\pi)^{N-F}\, \bar{D}_t(\mathbf{z}_0, \mathbf{z}_0') \prod_{\substack{j=F+1 \\ j=N+F+1}}^{\substack{2N \\ N}} \left[\delta\left(\Delta_j\right)\right], \tag{4.4}$$

with

$$\bar{D}_t(\mathbf{z}_0, \mathbf{z}_0') = \lim_{\substack{c_{\text{quantum}}\to 0 \\ c_{\text{classical}}\to\infty}} \prod_{\substack{j=F+1 \\ j=N+F+1}}^{\substack{2N \\ N}} \left[\frac{1}{c_{jj}}\right]^{\frac{1}{2}} \det\left[\mathbf{K}^{\mathrm{T}} + i\tilde{\mathbf{c}}\mathbf{J}\right]^{\frac{1}{2}}. \tag{4.5}$$

The transpose of matrix $\mathbf{K}^{\mathrm{T}}$ is provided in Eq. 2.33, matrix $\mathbf{J}$ is provided in Eq. 2.34, and recall from Eq. 2.35 that $\tilde{\mathbf{c}}$ is given by

$$\tilde{\mathbf{c}} = \begin{pmatrix} \mathbf{c} & \mathbb{O} \\ \mathbb{O} & \mathbb{O} \end{pmatrix}, \tag{4.6}$$

$$\mathbf{c} = \begin{pmatrix} \mathbf{c}_q & \mathbb{O} \\ \mathbb{O} & \mathbf{c}_p \end{pmatrix}. \tag{4.7}$$

The goal from here is to expand the determinant in Eq. 4.5 and evaluate the limit term-by-term. Using the definition of the determinant of a $4N \times 4N$ matrix $\boldsymbol{\Xi}$,

$$\det[\boldsymbol{\Xi}] = \sum_{i_1,\ldots,i_{4N}}^{4N} \epsilon_{i_1\ldots i_{4N}} \prod_{j=1}^{4N} \Xi_{ji_j}, \tag{4.8}$$

and after noting that the lower half of $\tilde{\mathbf{c}}$ contains only zeros, an expansion of the determinant in Eq. 4.5 gives

$$\bar{D}_t(\mathbf{z}_0, \mathbf{z}_0') = \lim_{\substack{c_{\text{quantum}}\to 0 \\ c_{\text{classical}}\to\infty}} \left\{ \prod_{\substack{j=F+1 \\ j=N+F+1}}^{\substack{2N \\ N}} \left[\frac{1}{c_{jj}}\right] \sum_{i_1,\ldots,i_{4N}}^{4N} \epsilon_{i_1\ldots i_{4N}} \prod_{j=1}^{2N} \left[K^{\mathrm{T}}_{ji_j} + ic_{jj}J_{ji_j}\right] \prod_{j=2N+1}^{4N} \left[K^{\mathrm{T}}_{ji_j}\right] \right\}^{\frac{1}{2}}. \tag{4.9}$$

After the leading product on the right-hand side Eq. 4.9 is carried through the summation, the only terms that survive the limit are those that are independent of the elements of $\mathbf{c}$. Every other term will either contain a parameter in the numerator that tends to zero, or a parameter in the denominator that tends to infinity. Evaluating the limit therefore gives

$$\bar{D}_t\left(\mathbf{z}_0, \mathbf{z}_0'\right) = \left\{ \sum_{i_1,\ldots,i_{4N}}^{4N} \epsilon_{i_1 \ldots i_{4N}} \prod_{\substack{j=F+1 \\ j=N+F+1}}^{\substack{2N \\ N}} \left[i J_{j i_j} \right] \prod_{\substack{j=1 \\ j=N+1 \\ j=2N+1}}^{\substack{4N \\ N+F \\ F}} \left[K^{\mathrm{T}}_{j i_j} \right] \right\}^{\frac{1}{2}} . \tag{4.10}$$

Eq. 4.10 is equivalent to the determinant of matrix $\mathbf{K}^{\mathrm{T}}$ plus an additional matrix $\boldsymbol{\Sigma}$. The addition of $\boldsymbol{\Sigma}$ to $\mathbf{K}^{\mathrm{T}}$ effectively replaces j rows of matrix $\mathbf{K}^{\mathrm{T}}$ with the corresponding rows of matrix $i\mathbf{J}$ $\forall\ j \in [F+1, N]$ and $\forall\ j \in [N+F+1, 2N]$,

$$\bar{D}_t\left(\mathbf{z}_0, \mathbf{z}_0'\right) = \det\left[\mathbf{K}^{\mathrm{T}} + \boldsymbol{\Sigma}\right], ^{\frac{1}{2}} \tag{4.11}$$

$$\boldsymbol{\Sigma} = \begin{pmatrix} \boldsymbol{\Omega} & \boldsymbol{\Omega}^{*} \\ \mathbb{O} & \mathbb{O} \end{pmatrix}, \tag{4.12}$$

$$\boldsymbol{\Omega}_{jk} = \begin{cases} i\left(1 - \frac{1}{2}\gamma_{jk}\right)\delta_{jk} & F < j,k \leq N \\ i\left(1 - \frac{1}{2}\gamma_{jk}^{-1}\right)\delta_{jk} & N+F < j,k < 2N \\ -\frac{1}{2}\delta_{j-N,k} & N+F < j < 2N, F < k \leq N \\ \frac{1}{2}\delta_{j,k-N} & F < j \leq N, N+F < k \leq 2N \\ 0 & \text{else.} \end{cases} \tag{4.13}$$

Given that $\mathbf{K}^{\mathrm{T}}$ is invertible, Eq. 4.10 can equivalently be written as

$$\bar{D}_t\left(\mathbf{z}_0, \mathbf{z}_0'\right) = \det\left[\mathbf{K}^{\mathrm{T}}\right]^{\frac{1}{2}} \det\left[\mathbb{I} + \boldsymbol{\Sigma}\left(\mathbf{K}^{\mathrm{T}}\right)^{-1}\right]^{\frac{1}{2}} . \tag{4.14}$$

As shown in Appendix B, the leading term on the right-hand side of Eq. 4.14 is

proportional to the product of HK prefactors. We therefore have

$$\begin{aligned}\bar{D}_t(\mathbf{z}_0, \mathbf{z}_0') =& (-1)^{\frac{N}{2}} C_t(\mathbf{z}_0) C_t^*(\mathbf{z}_0') \det\left[\mathbb{I} + \boldsymbol{\Sigma}\left(\mathbf{K}^{\mathrm{T}}\right)^{-1}\right]^{\frac{1}{2}} \\ =& C_t(\mathbf{z}_0) C_t^*(\mathbf{z}_0') \Lambda_t(\mathbf{z}_0, \mathbf{z}_0'). \end{aligned} \tag{4.15}$$

Now substitute Eq. 4.15 into Eq. 4.4, and then substitute Eq. 4.4 into the MQC-IVR time-correlation function. After evaluating the integrals over the primed phase space variables associated with the classical dofs, i.e. over each $z_j' \ \forall \ j \in [F+1, N]$, we obtain AMQC-IVR:

$$\begin{aligned} C_{AB}(t) =& \frac{1}{(2\pi)^{N+F}} \int d\mathbf{z}_0 \int dz_1' \ldots \int dz_F' \, \langle \mathbf{z}_0 | \hat{A} | z_1' \ldots z_F' z_{F+1} \ldots z_N \rangle \, B_{\mathbf{z}_t' \mathbf{z}_t} \\ & \times C_t(\mathbf{z}_0) C_t^*(z_1', \ldots, z_F', z_{F+1}, \ldots, z_N) \, e^{i\left[S_t(\mathbf{z}_0) - S_t(z_1', \ldots, z_F', z_{F+1}, \ldots, z_N)\right]} \\ & \times \Lambda_t(\mathbf{z}_0, z_1', \ldots, z_F'). \end{aligned} \tag{4.16}$$

In obtaining Eq. 4.16 from DHK-IVR we have reduced the dimensionality of the double phase space integral from $4N$ to $2(N+F)$. The initial phase space points of the classical dofs are the same in each trajectory pair of the ensemble average, i.e. $\Delta_j = 0 \ \forall \ j \in [F+1, N]$ and $\forall \ j \in [N+F+1, 2N]$, and the initial phase space points of the quantum dofs are generally different. Using similar initial conditions in this way ensures that, on average, the displacements between trajectory pairs at later times, $\boldsymbol{\Delta}_t = \mathbf{z}_t' - \mathbf{z}_t$, are much smaller than would otherwise be without MFF. This can cause significant phase cancellation, and therefore accelerate convergence, but the remaining displacements among the quantum dofs can give rise to enough phase information to preserve quantum mechanical accuracy. One would therefore expect AMQC-IVR to be most efficient when the ratio of classical to quantum dofs is large. One would also expect, in terms of accuracy, that the AMQC-IVR approximation is more reliable when the coupling between quantum and classical dofs is weak, since the phase contributions from

classical dofs are less important when the classical dofs have a weaker influence on the motion of the quantum dofs.

Like MQC-IVR, AMQC-IVR is a uniform SC-IVR method that offers mode-specific quantization without any uncontrolled approximations in the feedback forces between quantum and classical subsystems. In AMQC-IVR, however, the dimensionality of the double phase space integral is significantly smaller and there is no need to choose an optimal set of $2N$ tuning parameters. Additionally, AMQC-IVR treats each dof in the extreme classical or quantum limits of SC-IVR theory, which is more satisfying than MQC-IVR where each dof is arbitrarily treated somewhere in between the extreme limits.

4.2 Separable Prefactor Approximation

For a system of non-interacting particles AMQC-IVR has a very appealing analytical form that is much cheaper to compute than otherwise. This form can also be the starting point for a variety of other useful methods and approximations. Given that, in an uncoupled system, the HK-IVR phase and prefactor are separable,

$$C_t(\mathbf{z}_0)\, e^{iS_t(\mathbf{z}_0)} = \prod_{j=1}^{N} \left[C_t\left(z_{0j}\right) e^{iS_t\left(z_{0j}\right)} \right], \tag{4.17}$$

where $C_t\left(z_{0j}\right)$ and $S_t\left(z_{0j}\right)$ are the 1D HK-IVR prefactor and classical action for the j^{th} dof, respectively, one can use the stationary phase limit of MFF on each classical dof independently in DHK-IVR, evaluate the integrals over $z'_j \;\forall\; j \in$

$[F+1, N]$, and obtain the uncoupled equivalent of AMQC-IVR:

$$C_{AB}(t) = \frac{1}{(2\pi)^{N+F}} \int d\mathbf{z}_0 \int dz'_1 \ldots \int dz'_F \, \langle \mathbf{z}_0 | \hat{A} | z'_1 \ldots z'_F z_{F+1} \ldots z_N \rangle \, B_{\mathbf{z}'_t \mathbf{z}_t} \times \prod_{j=1}^{F} \left[C_t\left(z_j\right) C_t^*\left(z'_j\right) e^{i\left[S_t\left(z_j\right) - S_t\left(z'_j\right)\right]} \right]. \tag{4.18}$$

A comparison of Eq. 4.16 with Eq. 4.18 shows that Λ_t in AMQC-IVR is equal to unity in uncoupled systems,

$$\Lambda_t\left(\mathbf{z}_0, z'_1, \ldots, z'_F, z_{F+1}, \ldots, z_N\right) = 1. \tag{4.19}$$

This shows that uncoupled AMQC-IVR does not contain any multidimensional determinants, which is a very significant computational advantage since Λ_t is the most expensive component of AMQC-IVR to compute. For this reason one might expect that Eq. 4.19 can serve as a very efficient approximation to use in Eq. 4.16 when simulating systems with weak coupling between quantum and classical subsystems. We will refer to this as the separable prefactor (SP) approximation, and its efficiency should grow with larger system sizes, i.e. where the cost of computing determinants is most expensive.

There are several other practical benefits of the SP approximation. One can reduce computation time even further by propagating only a subset of the monodromy matrix elements, i.e. those corresponding to the quantum dofs, albeit approximately, rather than the entire $2N \times 2N$ monodromy matrix. Like the SP approximation itself, this additional approximation is increasingly valid as the coupling between quantum and classical dofs tends to zero, and increasingly efficient with a larger ratio of classical to quantum dofs. Furthermore, since the SP approximation only contains HK-IVR prefactors it can utilize the (more efficient) log-derivative form of Eq. 1.34 as well as a variety of approximations to Eq. 1.34 that may prove useful in complex systems [124, 125].

4.3 Numerical Tests

In this section we use three multidimensional model systems to showcase the accuracy of AMQC-IVR. We begin by considering the 2D oscillator system of Section 2.4. When the anharmonic mode is treated in the quantum limit and the harmonic mode is treated in the classical limit, initial conditions are sampled from

$$\rho_1\left(z_1, z_1'\right) = \mathcal{N}_1 \left|\langle z_1|z_{i_1}\rangle \langle z_{i_1}|z_1'\rangle\right|, \tag{4.20}$$

$$\rho_2\left(z_2\right) = \mathcal{N}_2 \left|\langle z_2|z_{i_2}\rangle\right|^2, \tag{4.21}$$

respectively. When both modes are treated in the quantum limit initial conditions are sampled from

$$\rho\left(\mathbf{z}_0, \mathbf{z}_0'\right) = \mathcal{N}_1^2 \left|\langle \mathbf{z}_0|\mathbf{z}_i\rangle \langle \mathbf{z}_i|\mathbf{z}_0\rangle\right|. \tag{4.22}$$

And when both modes are treated in the classical limit with Husimi-IVR, initial conditions are sampled from

$$\rho\left(\mathbf{z}_0\right) = \mathcal{N}_2^2 \left|\langle \mathbf{z}_0|\mathbf{z}_i\rangle\right|^2. \tag{4.23}$$

Constants $\mathcal{N}_1$ and $\mathcal{N}_2$ are for normalization.

The second model contains the same anharmonic mode of the previous model, but now coupled to a bath of $N-1$ harmonic oscillators. The Hamiltonian is given by

$$\begin{aligned}\hat{H} =& \frac{\hat{p}_1^2}{2m_1} + \frac{1}{2}m_1\omega_1^2\hat{q}_1^2 - 0.1\hat{q}_1^3 + 0.1\hat{q}_1^4 \\ &+ \sum_{j=2}^{N}\left[\frac{\hat{p}_j^2}{2m_j} + \frac{1}{2}m_j\omega_j^2\left(\hat{q}_j - \frac{c_j\hat{q}_1}{m_j\omega_j^2}\right)^2\right],\end{aligned} \tag{4.24}$$

An Ohmic spectral density with an exponential cutoff is used for the bath,

$$J(\omega) = \eta\omega e^{-\omega/\omega_1}, \tag{4.25}$$

with coupling strength η. Again, the initial state of the system is a product of N coherent states,

$$\Psi(\mathbf{x}, 0) = \langle \mathbf{x}|\mathbf{z}_i\rangle \tag{4.26}$$

$$= \mathcal{N} \prod_{j=1}^{N} e^{-\frac{\gamma_j}{2}(x_j - q_j)^2 + ip_j(x_j - q_j)}, \tag{4.27}$$

with $\mathcal{N}$ for normalization. The initial coherent states are centered at $q_{i_1} = 1.0$, $p_{i_1} = 0.0$, and $q_{i_j} = p_{i_j} = 0.0 \; \forall \; j \in [2, N]$. And the coherent state width parameter of the j^{th} dof is given by $\gamma_j = m_j\omega_j \; \forall \; j$. When the anharmonic mode is treated in the quantum limit and all the bath modes are treated in the classical limit, Eq. 4.20 and Eq. 4.21 are used to sample initial conditions, respectively. When all dofs are treated in the classical limit with Husimi-IVR, we use Eq. 4.23 to sample initial conditions. We use a bath of 12 oscillators and we take $\hat{B} = \hat{x}_1$ to compute the position expectation value of the anharmonic mode as a function of time.

The third model system is the widely used symmetric double well potential coupled to a thermal bath of $N - 1$ harmonic oscillators at $T = 300K$. The Hamiltonian is given by

$$\begin{aligned}\hat{H} =& \frac{\hat{p}_1^2}{2m_1} - \frac{1}{2}m_1\omega_b^2\hat{q}_1^2 + \frac{m_1^2\omega_b^4}{16V_0^{\ddagger}}\hat{q}_1^4 \\ &+ \sum_{j=2}^{N}\left[\frac{\hat{p}_j^2}{2m_j} + \frac{1}{2}m_j\omega_j^2\left(\hat{q}_j - \frac{c_j\hat{q}_1}{m_j\omega_j^2}\right)^2\right].\end{aligned} \tag{4.28}$$

The form of the spectral density is the same as in Eq. 4.25, and all numerical parameters as well as the bath discretization scheme are specified elsewhere

[126]. With this model we compute the thermal transmission coefficient of the symmetric double-well, $\kappa(T)$, by means of a flux-side correlation function [127],

$$\kappa(T) = \frac{k(T)}{k_{\mathrm{cl}}^{\mathrm{TST}}(T)} \tag{4.29}$$

$$= \frac{1}{k_{\mathrm{cl}}^{\mathrm{TST}}(T) Q_r(T)} \lim_{t\to\infty} C_{fs}(t), \tag{4.30}$$

where $k_{\mathrm{cl}}^{\mathrm{TST}}(T)$ is the classical transition state theory result, $Q_r(T)$ is the partition function in the reactant well, and $C_{fs}(t)$ is the flux-side correlation function characterized by

$$\hat{A} = e^{-\beta\hat{H}/2}\hat{F}e^{-\beta\hat{H}/2}, \tag{4.31}$$

$$\hat{B} = \hat{h}. \tag{4.32}$$

Eq. 4.31 contains the flux operator, $\hat{F} = i\left[\hat{H}, \hat{h}\right]$, and $\beta = 1/kT$ with Boltzmann constant k. In Eq. 4.32 $\hat{h}$ is the unit step function specifying the dividing surface. We take the symmetric double-well to be the only quantum dof, and we take the remaining 12 harmonic bath modes to be classical dofs. In order to evaluate the coherent state matrix element of $\hat{A}$ in Eq. 4.31 we make a normal-mode approximation at the transition state [58] so that the Hamiltonian is approximately separable:

$$\hat{H} \approx \hat{H}_1 + \sum_{j=2}^{N} \hat{H}_j, \tag{4.33}$$

$$\hat{H}_1 = \frac{\hat{p}_1^2}{2m} - \frac{1}{2}m\lambda^{\ddagger 2}\hat{x}_1^2 + V_0^{\ddagger}, \tag{4.34}$$

$$\hat{H}_j = \frac{\hat{p}_j^2}{2m_j} + \frac{1}{2}m_j\lambda_j^2\hat{x}_j^2. \tag{4.35}$$

Frequencies $\lambda^{\ddagger}$ and λ_j are the imaginary and real normal-mode frequencies at the transition state, respectively. Under this approximation, the coherent state

matrix element of $\hat{A}$ in Eq. 4.31 is given by

$$A_{\mathbf{z}_0\mathbf{z}'_0} = \mathcal{F}_{z_1 z'_1} \prod_{j=2}^{N} \mathcal{B}_{z_j z'_j}, \tag{4.36}$$

$$\begin{aligned}\mathcal{F}_{z_1 z'_1} =& \frac{\gamma_1}{8 m_1 \sqrt{\pi} \cos^2 u^{\ddagger}} \\ & \times \left[\left(p'_1 + p_1\right) / \sqrt{\gamma_1} - i \sqrt{\gamma_1} \left(q'_1 - q_1\right) \right] \\ & \times e^{-\frac{\gamma_1}{4}\left(q'^2_1 + q^2_1\right)} e^{-\frac{1}{4\gamma_1}\left(p'^2_1 + p^2_1\right)} \\ & \times e^{\frac{i}{2}\left(p_1 + p'_1\right)\left(q_1 - q'_1\right)} e^{-\beta V_0^{\ddagger}},\end{aligned} \tag{4.37}$$

$$\begin{aligned}\mathcal{B}_{z_j z'_j} =& e^{-\frac{\gamma_j}{4}\left(q^2_j + q'^2_j\right)} e^{-\frac{1}{4\gamma_j}\left(p^2_j + p'^2_j\right)} e^{\frac{i}{2}\left(p_j q_j - p'_j q'_j\right)} \\ & \times e^{\frac{1}{2} e^{-2u_j}\left[\gamma_j q_j q'_j + p_j p'_j / \gamma_j + i\left(p'_j q_j - p_j q'_j\right)\right]} e^{-u_j},\end{aligned} \tag{4.38}$$

with $u_1 = \beta \left|\lambda^{\ddagger}\right| / 2$, $u_j = \beta \lambda_j / 2 \ \forall \ j = 2 \ldots N$, and we choose $\gamma_1 = m_1 |\lambda^{\ddagger}| \cot u^{\ddagger}$ as well as $\gamma_j = m_j \lambda_j \ \forall \ j = 2 \ldots N$. With AMQC-IVR, however, only the diagonal elements of Eq. 4.38 are needed:

$$\langle \mathbf{z}_0 | \hat{A} | z'_1 \ldots z'_F z_{F+1} \ldots z_N \rangle = \mathcal{F}_{z_1 z'_1} \prod_{j=2}^{N} \mathcal{B}_{z_j z_j}, \tag{4.39}$$

$$\mathcal{B}_{z_j z_j} = e^{-\frac{\gamma_j}{2}\left(1 - e^{-2u_j}\right) q^2_j} e^{-\frac{1}{2\gamma_j}\left(1 - e^{-2u_j}\right) p^2_j} e^{-u_j}. \tag{4.40}$$

Initial conditions for the quantum and classical dofs are sampled from the following distributions,

$$\begin{aligned}\rho_1\left(z_1, z'_1\right) = & N_1 e^{-\frac{\gamma_1}{4}\left(q'^2_1 + q^2_1\right)} \\ & \times e^{-\frac{1}{4\gamma_1}\left(p'^2_1 + p^2_1\right)}\end{aligned} \tag{4.41}$$

$$\rho_j\left(z_j\right) = N_j \mathcal{B}_{z_j z_j} e^{u_j}, \tag{4.42}$$

respectively. Constants N_1 and $N_j \ \forall \ j \in (2, 13)$ are for normalization. The coherent state matrix element of $\hat{h}$ at time t is given by

$$h_{\mathbf{z}'_t \mathbf{z}_t} = \frac{1}{2}\left[\mathrm{Erf}\left(\frac{1}{2}\alpha_t\right) + 1 \right] \langle \mathbf{z}'_t | \mathbf{z}_t \rangle, \tag{4.43}$$

$$\alpha_t = \sqrt{\gamma_1}\left(q_{t_1} + q'_{t_1}\right) - i\left(p'_{t_1} - p_{t_1}\right) / \sqrt{\gamma_1}, \tag{4.44}$$

where Erf (x) is the error function of x.

The position expectation value of the anharmonic mode in model 1 is plotted as a function of time in Fig. 4.1 with three different coupling strengths.

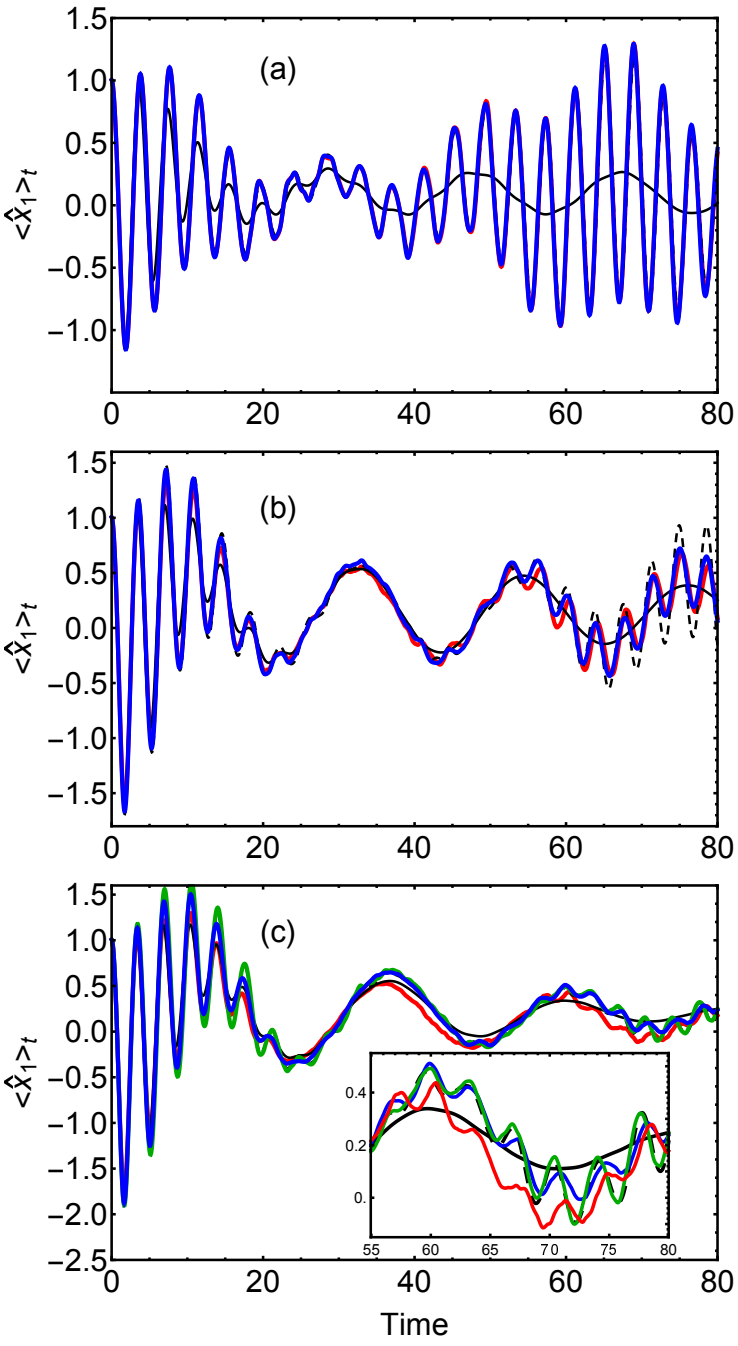

Figure 4.1: The average position of the anharmonic mode in model 1 as a function of time, as computed with exact quantum (black, dashed), Husimi-IVR (black), AMQC-IVR with one quantized mode (blue), AMQC-IVR with one quantized mode under the separable prefactor approximation (red), and AMQC-IVR with two quantized modes (green). Each panel corresponds to a different coupling strength: (a) $k = 0.5$, (b) $k = 1.5$, and (c) $k = 2.0$. The inset in (c) amplifies the correlation function from $t = 55$ to $t = 80$.

The rapid oscillations in the exact quantum results at long times are a result of nuclear coherence, a feature that is clearly absent in the classical limit Husimi-IVR results. AMQC-IVR does well in describing the quantum mechanical oscillations in each coupling region, and with consistent accuracy (see Table 4.1), even when the quantum and classical modes are more strongly coupled. In some cases the AMQC-IVR result is slightly damped relative to the exact result, but the quantum mechanical features are still captured.

k	0.5	1.0	1.5	2.0
Avg. % Error	1.0	1.07	0.96	0.91(0.31)

Table 4.1: The time-averaged (relative) % error of each AMQC-IVR result. The result in parentheses was obtained after quantizing both the anharmonic and harmonic dofs.

Also plotted in Fig. 4.1 are the AMQC-IVR results obtained with the SP approximation of Sec. 4.2. In Fig. 4.1(a) and (b) these results are nearly identical to the AMQC-IVR results without an approximate prefactor. Some of the long-time oscillations are captured by the SP approximation in Fig. 4.1(c), where the coupling is strongest, but the result is clearly less accurate (see Table 4.2). Though the SP approximation appears to be accurate in this model system, its efficiency should proliferate in larger systems where the computational cost of computing prefactors grows quickly.

k	0.5	1.0	1.5	2.0
Avg. % Error	0.81	1.06	1.53	1.85

Table 4.2: The time-averaged (relative) % error of each AMQC-IVR result with the SP approximation.

Fig. 4.1(c) also shows $\langle \hat{x}_1 \rangle_t$ as computed with AMQC-IVR when all modes are treated in the quantum limit. Since all dofs are quantized here, this is formally

equivalent to using DHK-IVR of Eq. 2.26, but the AMQC-IVR prefactor was used during computation. The result is nearly identical to the exact quantum result at all times. This reveals that unobserved dofs, i.e. those not measured by operator $\hat{B}$, contribute important phase information to the correlation function when more strongly coupled to the observed dofs. This is intuitive since, in a more strongly coupled system, the dynamics of unobserved dofs should more strongly influence the dynamics of observed dofs. This analysis suggests that AMQC-IVR can be systematically improved toward the DHK-IVR limit in multidimensional systems.

The average position of the anharmonic mode of the system-bath model characterized by the Hamiltonian in Eq. 4.24 is plotted in Fig. 4.2 as a function of time. Each panel corresponds to a different coupling strength η between the anharmonic dof and the harmonic bath.

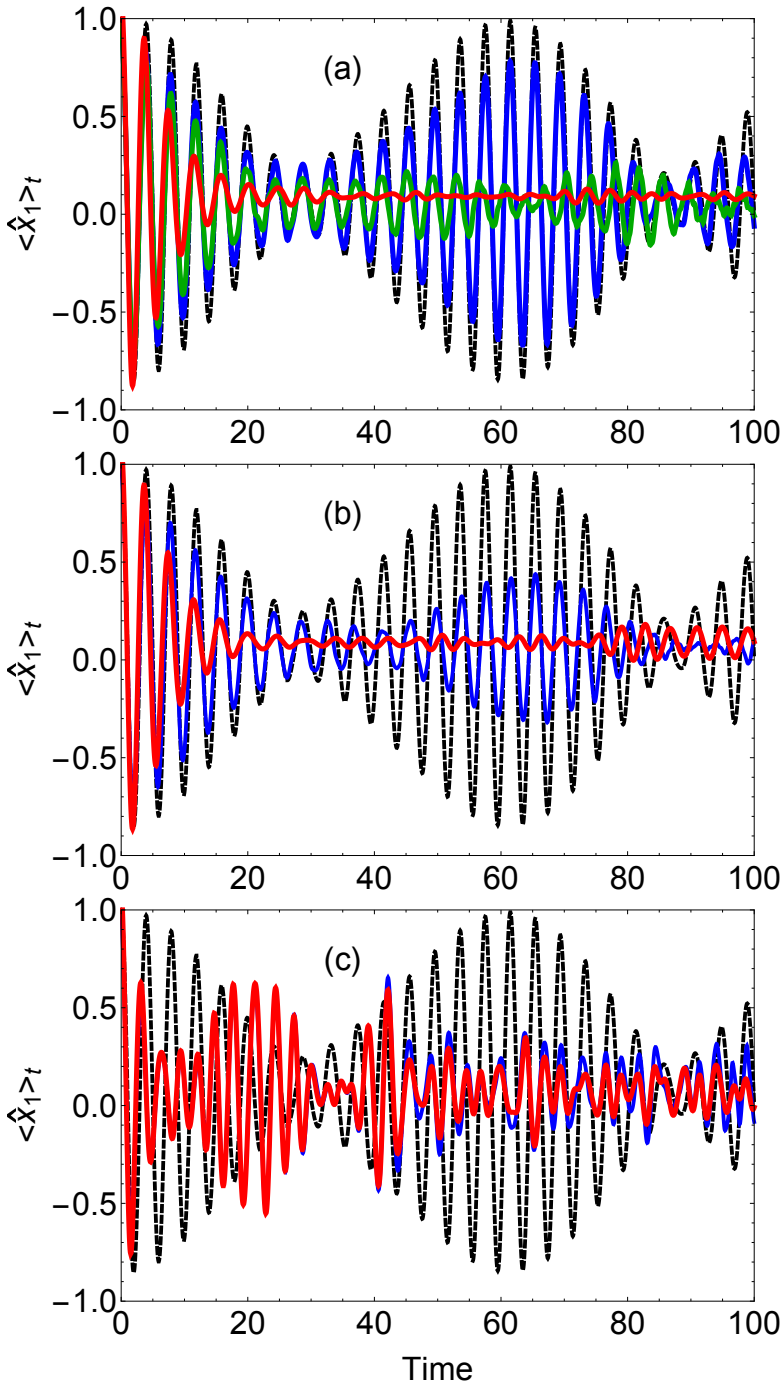

Figure 4.2: The average position of the anharmonic mode in model 2 as computed with AMQC-IVR (blue) and Husimi-IVR (red) with a reduced coupling strength of (a) $\eta/m\omega_1 = 0.001$, (b) $\eta/m\omega_1 = 0.01$, and (c) $\eta/m\omega_1 = 1.0$. The exact quantum result (black, dashed) of the 1D anharmonic oscillator in the absence of coupling to the bath is shown as well. Panel (a) also contains the AMQC-IVR result with the SP approximation (green).

In Fig. 4.2(a), where the coupling between the system and bath is very weak, the AMQC-IVR result is very similar to the exact quantum result of the uncoupled anharmonic oscillator. The slight damping effect seen in the amplitudes is likely attributable to the influence of the harmonic environment. The classical Husimi-IVR result, on the other hand, appears to fail at all but very short times. This suggests that AMQC-IVR is accurate when the coupling between quantum and classical dofs is sufficiently weak. This is a very appealing result since a full SC treatment of such a highly multidimensional system, such as with DHK-IVR, is generally impossible. Furthermore, only about 10^5 trajectory pairs (or fewer in the strong coupling case) were required to converge the results in Fig. 4.2.

In Fig. 4.2(b), where the coupling is $10\times$ stronger than in Fig. 4.2(a), the oscillatory features of the AMQC-IVR result are still similar to that of the exact uncoupled result, but with significantly more damping. Again, the damping effect is likely attributable to a stronger influence from the harmonic bath. In Fig. 4.2(c), where the coupling is $10^3\times$ stronger than in Fig. 4.2(a), the AMQC-IVR result more closely resembles the classical Husimi-IVR result, with slight deviations from about $t = 30$ and beyond. The similarity between AMQC-IVR and Husimi-IVR results in Fig. 4.2(c) is expected considering that a strong influence from the bath should damp away interference effects contained in the system.

Also plotted in Fig. 4.2(a) is the AMQC-IVR result with the SP approximation. Computation under this approximation was approximately $4\times$ faster than without. In this model system, however, even when the coupling strength is as weak as $\eta = 0.001$, the SP approximation appears to be only valid at short-times. And though some oscillatory behavior is present at later times, the SP

approximation only offers marginal improvement to the classical limit result.

The thermal transmission coefficient of the system-bath model characterized by the Hamiltonian in Eq. 4.28 is plotted in Fig. 4.3 as a function of the reduced coupling strength $\eta/m\omega_b$.

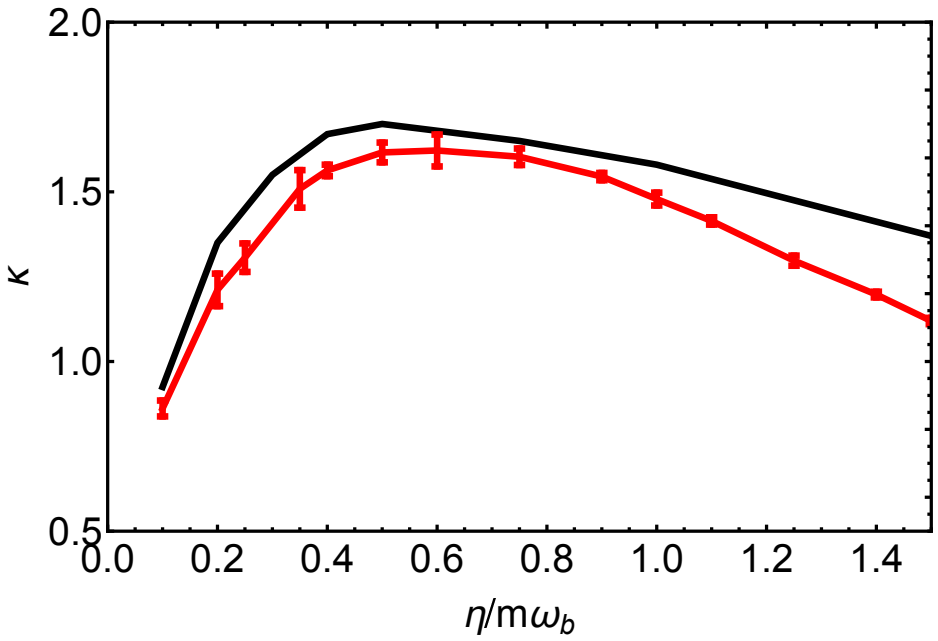

Figure 4.3: The AMQC-IVR (red) thermal transmission coefficient of model 3 at $T = 300K$ as a function of the reduced coupling strength. Exact path integral results (black) are obtained from a previous study [126].

Fig. 4.3 shows that AMQC-IVR is quantitatively accurate in the weak coupling regime and it nicely captures the turn-over region around $\eta/m\omega_b = 0.6$, but begins to increasingly underestimate κ in the strong coupling regime for $\eta/m\omega_b > 0.8$. The failure of AMQC-IVR in the strong coupling regime is most likely due to the removal of important phase contributions from bath dofs by MFF. This can be rationalized by noting that FB-IVR [58], which contains more phase contributions from bath dofs than in AMQC-IVR, has shown to be consis-

tently accurate across all coupling regimes when applied to this model system. However, as mentioned in Chapter 2, FB implementations are far more cumbersome to implement as opposed to DF implementations like AMQC-IVR. In a weak-coupling limit, therefore, the latter methodology is the favorable choice. Furthermore, as suggested in Fig. 4.1(c), it is possible that the AMQC-IVR results in Fig. 4.3 can be systematically improved toward the DHK-IVR limit by quantizing well-chosen bath modes, but a systematic procedure to achieve this is ongoing work.

Fig. 4.4 plots the thermal transmission coefficient in a weak coupling limit, $\eta/m\omega_b = 0.05$, as a function of time with AMQC-IVR as well as AMQC-IVR with the SP approximation.

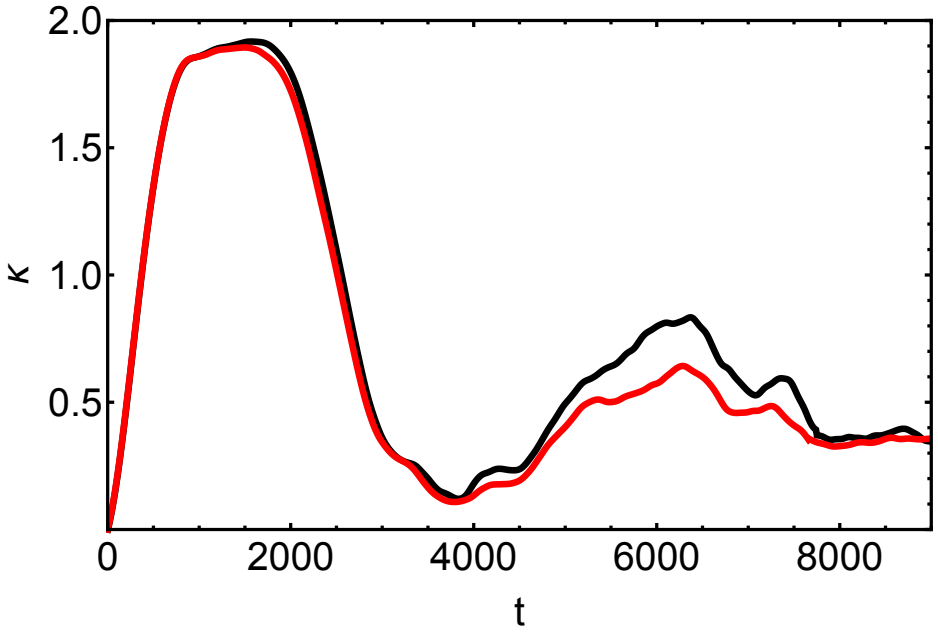

Figure 4.4: The thermal transmission coefficient of model 3 at $T = 300K$ as a function of time, with $\eta/m\omega_b = 0.05$, as computed with AMQC-IVR (black) and with AMQC-IVR with the SP approximation (red).

The latter is slightly damped relative to the former, particularly in the second peak around $t = 6000$, but the two results converge to the same rate in the long-time limit. Since the AMQC-IVR prefactor includes a large determinant in this model, the SP approximation offers a large reduction in computational expense here. When using 12 classical bath modes, as is used to generate Fig. 4.4, the SP approximation is about 4× faster than without. When doubling the number of classical bath modes to 24, which does not visibly effect the rate, the SP approximation is about 7× faster than without. This analysis shows that the SP approximation can be very reliable and efficient in large systems when the coupling between quantum and classical subsystems is weak.

CHAPTER 5

SEMICLASSICAL NONADIABATIC DYNAMICS

Many dynamical problems in chemical physics are greatly simplified under the Born-Oppenheimer approximation [128] (BOA), where it assumed that nuclear and electronic motion occurs on very different timescales. Under this approximation we state that the wavefunction Ψ describing the entire vibronic system is separable into a nuclear component ψ_N and an electronic component ψ_e,

$$\Psi = \psi_N \otimes \psi_e. \tag{5.1}$$

Evolution of the nuclear system is therefore carried out on a single adiabatic electronic potential energy surface, without the concern of coupling and transitions to different surfaces.

There are, however, a variety of interesting chemical problems where nuclear and electronic motion occurs on similar time-scales. This kind of motion can be common in systems with narrowly-separated electronic surfaces and a large number of nuclear dofs, in photochemical problems with large molecules, in hot-electron generation at metal surfaces, charge transfer processes, proton-coupled electron transfer reactions, and any process in the vicinity of a conical intersection [2, 4, 5, 8, 109, 129–131]. In such electronically nonadiabatic systems, where nuclear motion now occurs on multiple adiabatic electronic potential energy surfaces, the BOA is no longer valid.

A variety of methods have therefore been developed over the past few decades in order to study electronically nonadiabatic systems. Some notable approaches are based on exact quantum time-propagation [132–135], symmet-

rical quasi-classical windowing [136], MQC Liouville methods [137–139], the Ehrenfest model [129, 140], surface hopping [141–146], partial linearization of the density matrix [147], and path-integral based methods like RPMD and CMD [95, 97, 148–153]. Of these methods, however, those based on exact quantum evolution are generally limited to a small number of dofs, and the more approximate methods generally fail at describing nuclear coherence. The various SC-IVR methods mentioned earlier in this study have also shown promise in describing aspects of nonadiabatic systems [54, 59, 75, 154–156], but these methods also tend to either fail at describing nuclear coherence, are limited to small systems, or are slow to implement (as compared to the DF methods presented in Chapter 2 and Chapter 4).

In this chapter we showcase the applicability of MQC-IVR to the study of nonadiabatic systems. As with several of the methods mentioned in the previous paragraph, we use the Meyer-Miller-Stock-Thoss (MM-ST) Hamiltonian for vibronic systems in order to represent discrete electronic state information in terms of continuous cartesian variables, granting the ability evolve the entire vibronic system with the classical equations of motion in a dynamically consistent way. We begin by reviewing the MM-ST Hamiltonian as well as a symplectic integration algorithm for propagating trajectories under its influence. Finally, we compute nuclear and electronic properties of a nonadiabatic model system using MQC-IVR with various sets of tuning parameters.

5.1 MM-ST Hamiltonian

Meyer and Miller [111] originally devised the so-called classical analog of the electronic Hamiltonian as a means to treat both nuclear and electronic dofs on the same dynamical footing. Begin by considering the full quantum mechanical Hamiltonian of an F-level system,

$$H = \sum_j \frac{P_j^2}{2m_j} + H_{el}, \tag{5.2}$$

$$H_{el} = \sum_{n,m}^{F} |n\rangle V_{nm}(\mathbf{R}) \langle m|, \tag{5.3}$$

where H_{el} is the electronic Hamiltonian and $V_{nm}(\mathbf{R})$ are elements of the diabatic electronic potential energy matrix parametrized by the nuclear coordinates $\mathbf{R}$. When written in the basis of electronic states $\{|n\rangle\}$, the total wavefunction is given by

$$|\psi(t)\rangle = \sum_n^F c_n(t)|n\rangle. \tag{5.4}$$

Equations of motion for the complex expansion coefficients $\{c_n(t)\}$ in Eq. 5.4 can be derived from the time-dependent Schrödinger equation,

$$i\dot{c}_n(t) = \sum_m^F V_{nm}(\mathbf{R}) c_m(t). \tag{5.5}$$

Now define the complex expansion coefficients in terms of real classical action-angle variables $\{\eta_n\}$ and $\{q_n\}$,

$$c_n(t) = \sqrt{\eta_n(t)} e^{-iq_n(t)}. \tag{5.6}$$

It follows that the expectation value of the electronic Hamiltonian is given by

$$\langle H_{el}\rangle_\psi = \langle\psi(t)|H_{el}|\psi(t)\rangle \tag{5.7}$$

$$= \sum_{nm}^F \sqrt{\eta_n \eta_m} e^{i(q_n - q_m)} V_{nm}(\mathbf{R}). \tag{5.8}$$

When $\langle H_{el} \rangle_\psi$ is considered as a classical electronic Hamiltonian, it follows that the action-angle variables $\{\eta_n\}$ and $\{q_n\}$ evolve according to Hamilton's equations of motion,

$$\dot{q}_n(t) = \frac{\partial}{\partial \eta_n} \langle H_{el} \rangle_\psi , \tag{5.9}$$

$$\dot{\eta}_n(t) = -\frac{\partial}{\partial q_n} \langle H_{el} \rangle_\psi : \tag{5.10}$$

a set of $2F$ equations that are identical to the F equations of Eq. 5.5. Meyer and Miller [111] therefore established a classical Hamiltonian for the complete vibronic system. After making a canonical transformation from action-angle variables to cartesian coordinates in phase space, and after including the nuclear kinetic energy term, this classical Hamiltonian can be written as

$$H = \sum_j \frac{P_j^2}{2m_j} + \frac{1}{2}\mathbf{x}^{\mathrm{T}}\mathbf{V}\mathbf{x} + \frac{1}{2}\mathbf{p}^{\mathrm{T}}\mathbf{V}\mathbf{p} - \frac{1}{2}\mathrm{Tr}\left[\mathbf{V}\right]. \tag{5.11}$$

A given vector in phase space, $\mathbf{z}$, containing both nuclear and electronic dofs will therefore evolve according to

$$\dot{\mathbf{z}} = \mathbf{J}\boldsymbol{\nabla}_{\mathbf{z}} H, \tag{5.12}$$

where $\mathbf{J}$ is the structure matrix,

$$\mathbf{J} = \begin{pmatrix} \mathbb{O} & \mathbb{I} \\ -\mathbb{I} & \mathbb{O} \end{pmatrix}, \tag{5.13}$$

and $\boldsymbol{\nabla}_{\mathbf{z}}$ is the gradient with respect to the phase space variables.

Several years later, Stock and Thoss [53, 112] devised a mapping procedure that confirmed the Meyer-Miller approximation as mathematically rigorous. The idea is to map the diabatic states on the right-hand side of Eq. 5.3 onto the singly-excited harmonic oscillator basis with the following mapping relations,

$$|n\rangle\langle m| \mapsto a_n^\dagger a_m, \tag{5.14}$$

$$|n\rangle \mapsto |0_1 \ldots 1_n \ldots 0_F\rangle , \tag{5.15}$$

where a_m and $a_n^\dagger$ are creation and annihilation operators of the harmonic oscillator, respectively, and $|0_1 \ldots 1_n \ldots 0_F\rangle$ is a state of $F-1$ harmonic oscillators in their ground state and a single excitation in the n^{th} oscillator. After using the mapping procedure on Eq. 5.3, and after expressing the harmonic oscillator creation and annihilation operators in terms of position and momentum operators, we recover the Meyer-Miller Hamiltonian of Eq. 5.11. Eq. 5.11 is therefore referred to as the MM-ST Hamiltonian.

Though the MM-ST Hamiltonian of Eq. 5.11 can be used to evolve classical trajectories in vibronic systems in a completely dynamically consistent manner, we desire an integration algorithm that satisfies the facets of classical mechanics (such as conservation of energy, Liouville's theorem, etc.). Namely, we wish to conserve the symplecticity criterion given by

$$\mathbf{M}^{\mathrm{T}}\mathbf{J}^{-1}\mathbf{M} = \mathbf{J}^{-1}, \tag{5.16}$$

where $\mathbf{M}$ is the full $2N \times 2N$ monodromy matrix of a given trajectory. Commonly used integration schemes such as the Runge-Kutta method and predictor-corrector algorithms do not satisfy Eq. 5.16. The difficulty in defining an integration algorithm that satisfies Eq. 5.16 is mainly due to the coupling between the electronic phase space variables ($\mathbf{x}$ and $\mathbf{p}$), which we will refer to as the mapping variables, with the nuclear positions $\mathbf{R}$. In the following section we review an integration algorithm, which we call the MInt algorithm [82, 157], that is exactly symplectic.

5.2 MInt Algorithm

5.2.1 Evolution Flow Map

The MInt algorithm [82, 157] relies on the following feature of classical mechanics: when the total Hamiltonian is decomposed into a sum of sub-Hamiltonians, a symmetric composition of exact evolutions under the sub-Hamiltonians results in an approximate evolution under the total Hamiltonian that is exactly symplectic [158]. The MM-ST Hamiltonian is therefore divided into two sub-Hamiltonians H_1 and H_2:

$$H = H_1 + H_2, \tag{5.17}$$

$$H_1 = \sum_j \frac{P_j^2}{2m_j}, \tag{5.18}$$

$$H_2 = \frac{1}{2}\mathbf{x}^{\mathrm{T}}\mathbf{V}\mathbf{x} + \frac{1}{2}\mathbf{p}^{\mathrm{T}}\mathbf{V}\mathbf{p} - \frac{1}{2}\mathrm{Tr}\left[\mathbf{V}\right]. \tag{5.19}$$

We now define a symmetric composition of evolutions under the two sub-Hamiltonians,

$$\Psi_{H,\Delta t} = \Phi_{H_1,\Delta t/2} \circ \Phi_{H_2,\Delta t} \circ \Phi_{H_1,\Delta t/2}. \tag{5.20}$$

In Eq. 5.20, $\Psi_{H,\Delta t}$ is an approximate flow map for evolution under the total Hamiltonian H for time Δt, and $\Phi_{H_i,\Delta t}$ is an exact flow map for evolution under sub-Hamiltonian H_i for time Δt. A flow map is a function which takes in a phase space point $\mathbf{z}_0$ and returns the time-evolved point $\mathbf{z}_t$ under a specified dynamics: $\mathbf{z}_t = \Phi_{H,\Delta t}\left(\mathbf{z}_0\right)$. The empty circles on the right-hand side of Eq. 5.20 signify the composition operation: $f \circ g\left(\mathbf{z}_0\right) = f\left(g\left(\mathbf{z}_0\right)\right)$. In words, Eq. 5.20 describes the evolution of the system under H_1 for half a time step, followed by evolution under H_2 for a full time step, and evolution under H_1 again for half

a time step. And since each evolution under the sub-Hamiltonians is exactly symplectic, the total evolution under the full Hamiltonian is exactly symplectic as well [82, 158].

It is possible to swap the sub-Hamiltonians H_1 and H_2 in Eq. 5.20 and define a similar symplectic algorithm for time evolution under the MM-ST Hamiltonian. But the equations of motion for evolution under H_1, i.e. free particle motion for the nuclear dofs, are much cheaper to solve than those corresponding to H_2. Therefore the sequence of evolutions described in Eq. 5.20 requires the least amount of work. The following section derives the equations of motion in detail.

5.2.2 Equations of Motion

As mentioned above, evolution under sub-Hamiltonian H_1 is equivalent to free particle motion for the nuclei,

$$\begin{aligned} \dot{R}_j =& \frac{\partial H}{\partial P_j} \\ =& P_j / m_j, \end{aligned} \tag{5.21}$$

$\forall\ j$ nuclear dofs, and all other phase space variables held constant. Integration of Eq. 5.21 for half a time step gives

$$R_j\left(\Delta t/2\right) = R_j\left(0\right) + P_j\left(0\right)\frac{\Delta t}{2m_j}. \tag{5.22}$$

Most SC quantities also require evolution of the classical action. Integration of the classical action for half a time step under H_1 evolution gives

$$S\left(\Delta t/2\right) = S\left(0\right) + \sum_j \frac{P_j^2 \Delta t}{4m_j}. \tag{5.23}$$

The sum on the right-hand side of Eq. 5.23 is over all nuclear dofs, and m_j are the corresponding masses. Hamilton's equations of motion for evolution under H_2 are given by the following,

$$\begin{aligned}\dot{\mathbf{x}} =& \frac{\partial H_2}{\partial \mathbf{p}} \\ =& \mathbf{V}(\mathbf{R})\,\mathbf{p}, \end{aligned} \tag{5.24}$$

$$\begin{aligned}\dot{\mathbf{p}} =& -\frac{\partial H_2}{\partial \mathbf{x}} \\ =& -\mathbf{V}(\mathbf{R})\,\mathbf{x}, \end{aligned} \tag{5.25}$$

$$\begin{aligned}\dot{P}_j =& -\frac{\partial H_2}{\partial R_j} \\ =& -\frac{1}{2}(\mathbf{x} - i\mathbf{p})\,\mathbf{V}_j(\mathbf{R})\,(\mathbf{x} + i\mathbf{p}) + \frac{1}{2}\mathrm{Tr}\left[\mathbf{V}_j(\mathbf{R})\right], \end{aligned} \tag{5.26}$$

with fixed $\mathbf{R}$. Note that we define $\mathbf{V}_j(\mathbf{R})$ as the derivative of the diabatic electronic potential energy matrix with respect to the position of the j^{th} nuclear dof: $\mathbf{V}_j(\mathbf{R}) := \frac{\partial}{\partial R_j}\mathbf{V}(\mathbf{R})$.

Since there is no nuclear momenta dependence in the equations of motion for the mapping variables in Eq. 5.24 and Eq. 5.25, the approach from here is to first solve for $\mathbf{x}$ and $\mathbf{p}$, and then use those solutions to compute P_j analytically. Combining and solving Eq. 5.24 and Eq. 5.25 gives [134, 159]

$$\left[\mathbf{x}(\Delta t) + i\mathbf{p}(\Delta t)\right] = e^{-i\mathbf{V}(\mathbf{R})\Delta t}\left[\mathbf{x}(0) + i\mathbf{p}(0)\right]. \tag{5.27}$$

For computational purposes, however, it is more convenient to rotate $\mathbf{V}(\mathbf{R})$ into the adiabatic basis, $\mathbf{S}^{\mathrm{T}}\mathbf{V}\mathbf{S} = \mathbf{\Lambda}$, and write Eq. 5.27 equivalently as

$$\mathbf{x}(\Delta t) = \mathbf{C}\mathbf{x}(0) - \mathbf{D}\mathbf{p}(0), \tag{5.28}$$

$$\mathbf{p}(\Delta t) = \mathbf{C}\mathbf{p}(0) + \mathbf{D}\mathbf{x}(0) \tag{5.29}$$

with

$$\mathbf{C} := \mathbf{S} \cos\left(\mathbf{\Lambda} \Delta t\right) \mathbf{S}^{\mathrm{T}}, \tag{5.30}$$

$$\mathbf{D} := \mathbf{S} \sin\left(-\mathbf{\Lambda} \Delta t\right) \mathbf{S}^{\mathrm{T}}. \tag{5.31}$$

For convenience we remove from the notation the $\mathbf{R}$-dependence of $\mathbf{V}$, $\mathbf{S}$, $\mathbf{\Lambda}$, and related matrices. We can now use the solutions for the mapping variables to solve for the nuclear momenta. Integration of Eq. 5.26 for a full time step, and using Eq. 5.27 gives

$$P_j\left(\Delta t\right) = P_j\left(0\right) - \frac{1}{2} \int_0^{\Delta t} dt \left\{ \left[\mathbf{x}\left(0\right) - i\mathbf{p}\left(0\right) \right] e^{+i\mathbf{V}\Delta t} \mathbf{V}_j e^{-i\mathbf{V}\Delta t} \left[\mathbf{x}\left(0\right) + i\mathbf{p}\left(0\right) \right] - \mathrm{Tr}\left[\mathbf{V}_j\right] \right\}. \tag{5.32}$$

We proceed by rotating the two matrix exponentials on the right-hand side of Eq. 5.32 into the adiabatic basis. And after defining

$$\mathbf{W}_j := \mathbf{S}^{\mathrm{T}} \mathbf{V}_j \mathbf{S}, \tag{5.33}$$

Eq. 5.32 then reduces to

$$\begin{aligned} P_j\left(\Delta t\right) =& P_j\left(0\right) - \frac{1}{2} \left[\mathbf{x}\left(0\right) - i\mathbf{p}\left(0\right) \right] \mathbf{S} \left[\int_0^{\Delta t} dt e^{+i\mathbf{\Lambda}\Delta t} \mathbf{W}_j e^{-i\mathbf{\Lambda}\Delta t} \right] \mathbf{S}^{\mathrm{T}} \left[\mathbf{x}\left(0\right) + i\mathbf{p}\left(0\right) \right] \\ &+ \frac{1}{2} \mathrm{Tr}\left[\mathbf{V}_j\right] \Delta t. \end{aligned} \tag{5.34}$$

The integral in Eq. 5.34 can now be evaluated analytically,

$$\int_0^{\Delta t} dt e^{+i\mathbf{\Lambda}\Delta t} \mathbf{W}_j e^{-i\mathbf{\Lambda}\Delta t} = \mathbf{\Gamma}_j + i\mathbf{\Xi}_j, \tag{5.35}$$

$\forall$ j nuclear dofs. The elements of the real-symmetric matrix $\mathbf{\Gamma}_j$ and the real skew-symmetric matrix $\mathbf{\Xi}_j$ are given by

$$\left(\Gamma_j\right)_{mn} = \begin{cases} \left(W_j\right)_{mn} \Delta t & m = n \\ \frac{1}{\lambda_{mn}} \sin\left(\lambda_{mn} \Delta t\right) \left(W_j\right)_{mn} & m \neq n, \end{cases} \tag{5.36}$$

$$\left(\Xi_j\right)_{mn} = \begin{cases} 0 & m = n \\ \frac{1}{\lambda_{mn}} \left[1 - \cos\left(\lambda_{mn} \Delta t\right)\right] \left(W_j\right)_{mn} & m \neq n, \end{cases} \tag{5.37}$$

respectively. Using the right-hand side of Eq. 5.35 in Eq. 5.34, and after defining matrices

$$\mathbf{E}_j := \mathbf{S}\boldsymbol{\Gamma}_j\mathbf{S}^{\mathrm{T}}, \tag{5.38}$$

$$\mathbf{F}_j := \mathbf{S}\boldsymbol{\Xi}_j\mathbf{S}^{\mathrm{T}}, \tag{5.39}$$

$\forall$ j nuclear dofs, we obtain the solution for nuclear momenta under H_2 evolution for time Δt:

$$P_j(\Delta t) = P_j(0) - \frac{1}{2}\mathbf{x}^{\mathrm{T}}(0)\,\mathbf{E}_j\mathbf{x}(0) - \frac{1}{2}\mathbf{p}^{\mathrm{T}}(0)\,\mathbf{E}_j\mathbf{p}(0) + \mathbf{x}^{\mathrm{T}}(0)\,\mathbf{F}_j\mathbf{p}(0) + \frac{1}{2}\mathrm{Tr}\left[\mathbf{V}_j\right]\Delta t. \tag{5.40}$$

The classical action is then completely evolved for time Δt with

$$S(\Delta t) = S(\Delta t/2) + \left[\mathbf{p}^{\mathrm{T}}\dot{\mathbf{x}} - H_2\right]\Delta t + \sum_j \frac{P_j^2\Delta t}{4m_j}. \tag{5.41}$$

5.2.3 Monodromy Matrix Elements

Most SC methods that contain complex prefactors also contain elements of the monodromy matrix. In this section we derive the monodromy matrix elements corresponding to evolution described in the approximate flowmap of Eq. 5.20. For free particle evolution under sub-Hamiltonian H_1 for half a time step, the monodromy matrix $\mathbf{M}_{H_1}$ is sparse. The diagonal elements of $\mathbf{M}_{H_1}$ are unity, and all off-diagonal elements are equal to zero save the following,

$$(M_{H_1})_{R_jP_k} = \frac{\Delta t}{2m_j}\delta_{jk}, \tag{5.42}$$

$\forall$ j, k nuclear dofs. Due to the coupling between the mapping variables and nuclear positions, the monodromy matrix $\mathbf{M}_{H_2}$ corresponding to evolution under

sub-Hamiltonian H_2 is more complicated. But analytical solutions are obtainable. First, using the mapping variable solutions of Eq. 5.28 and Eq. 5.29 it is trivial to show that

$$\mathbf{M}_{\mathbf{xx}}(\Delta t) = \mathbf{C}, \tag{5.43}$$

$$\mathbf{M}_{\mathbf{xp}}(\Delta t) = -\mathbf{D}, \tag{5.44}$$

$$\mathbf{M}_{\mathbf{px}}(\Delta t) = \mathbf{D}, \tag{5.45}$$

$$\mathbf{M}_{\mathbf{pp}}(\Delta t) = \mathbf{C}. \tag{5.46}$$

Note that the monodromy matrix elements described in Eq. 5.43-Eq. 5.46, and the monodromy matrix elements described in the following equations, Eq. 5.47-Eq. 5.53, apply only to $\mathbf{M}_{H_2}$. We drop the H_2 subscript from the notation for simplicity, then replace it later in Eq. 5.57. Next, taking the derivatives of Eq. 5.40 with respect to the initial mapping variables gives

$$\mathbf{M}_{P_j\mathbf{x}}(\Delta t) = -\left[\mathbf{x}^{\mathrm{T}}(0)\,\mathbf{E}_j + \mathbf{p}^{\mathrm{T}}(0)\,\mathbf{F}_j\right], \tag{5.47}$$

$$\mathbf{M}_{P_j\mathbf{p}}(\Delta t) = -\left[\mathbf{p}^{\mathrm{T}}(0)\,\mathbf{E}_j - \mathbf{x}^{\mathrm{T}}(0)\,\mathbf{F}_j\right]. \tag{5.48}$$

Taking the derivatives of Eq. 5.28 and Eq. 5.29 with respect to the position of the j^{th} nuclear dof then gives

$$\mathbf{M}_{\mathbf{x}R_j}(\Delta t) = \mathbf{C}_j\mathbf{x}(0) - \mathbf{D}_j\mathbf{p}(0), \tag{5.49}$$

$$\mathbf{M}_{\mathbf{p}R_j}(\Delta t) = \mathbf{C}_j\mathbf{p}(0) + \mathbf{D}_j\mathbf{x}(0), \tag{5.50}$$

$\forall\ j$ nuclear dofs. In Eq. 5.49 and Eq. 5.50 we also define

$$\begin{aligned}\mathbf{C}_j &:= \frac{\partial}{\partial R_j}\mathbf{C} \\ &= \mathbf{S}_j\cos(\mathbf{\Lambda}\Delta t)\,\mathbf{S}^{\mathrm{T}} - \mathbf{S}\sin(\mathbf{\Lambda}\Delta t)\,\mathbf{\Lambda}_j\Delta t\mathbf{S}^{\mathrm{T}} + \left[\mathbf{S}_j\cos(\mathbf{\Lambda}\Delta t)\,\mathbf{S}^{\mathrm{T}}\right]^{\mathrm{T}},\end{aligned} \tag{5.51}$$

$$\begin{aligned}\mathbf{D}_j &:= \frac{\partial}{\partial R_j}\mathbf{D} \\ &= -\mathbf{S}_j\sin(\mathbf{\Lambda}\Delta t)\,\mathbf{S}^{\mathrm{T}} - \mathbf{S}\cos(\mathbf{\Lambda}\Delta t)\,\mathbf{\Lambda}_j\Delta t\mathbf{S}^{\mathrm{T}} - \left[\mathbf{S}_j\sin(\mathbf{\Lambda}\Delta t)\,\mathbf{S}^{\mathrm{T}}\right]^{\mathrm{T}}.\end{aligned} \tag{5.52}$$

Finally, there is the derivative of Eq. 5.40 with respect to the j^{th} nuclear position,

$$\mathbf{M}_{P_j R_k}(\Delta t) = -\frac{1}{2}\left[\mathbf{x}^{\mathrm{T}}(0)\,\mathbf{E}_{jk}\mathbf{x}(0) + \mathbf{p}^{\mathrm{T}}(0)\,\mathbf{E}_{jk}\mathbf{p}(0) - 2\mathbf{x}^{\mathrm{T}}(0)\,\mathbf{F}_{jk}\mathbf{p}(0)\right] + \frac{1}{2}\mathrm{Tr}\left[\mathbf{V}_{jk}\right]\Delta t, \tag{5.53}$$

$\forall$ j nuclear dofs. In Eq. 5.53 we also define

$$\mathbf{V}_{jk} := \frac{\partial}{\partial R_k}\mathbf{V}_j \tag{5.54}$$

$$\begin{aligned}\mathbf{E}_{jk} :=& \frac{\partial}{\partial R_k}\mathbf{E}_j \\ =& \mathbf{S}_k\boldsymbol{\Gamma}_j\mathbf{S}^{\mathrm{T}} + \mathbf{S}\boldsymbol{\Gamma}_{jk}\mathbf{S}^{\mathrm{T}} + \left(\mathbf{S}_k\boldsymbol{\Gamma}_j\mathbf{S}^{\mathrm{T}}\right)^{\mathrm{T}}\end{aligned} \tag{5.55}$$

$$\begin{aligned}\mathbf{F}_{jk} :=& \frac{\partial}{\partial R_k}\mathbf{F}_j \\ =& \mathbf{S}_k\boldsymbol{\Xi}_j\mathbf{S}^{\mathrm{T}} + \mathbf{S}\boldsymbol{\Xi}_{jk}\mathbf{S}^{\mathrm{T}} + \left(\mathbf{S}_k\boldsymbol{\Xi}_j\mathbf{S}^{\mathrm{T}}\right)^{\mathrm{T}}.\end{aligned} \tag{5.56}$$

All of the remaining off-diagonal elements of $\mathbf{M}_{H_2}$ are equal to zero, and the remaining diagonal elements are equal to unity. With all of the elements of $\mathbf{M}_{H_1}$ and $\mathbf{M}_{H_2}$ defined, the entire monodromy matrix can be evolved under the full MM-ST Hamiltonian for time Δt with the following,

$$\mathbf{M}(\Delta t) = \mathbf{M}_{H_1}\mathbf{M}_{H_2}\mathbf{M}_{H_1}. \tag{5.57}$$

5.2.4 Step-by-step Algorithm

In this section we use the flowmap of Eq. 5.20 and the previously derived solutions to the equations of motion to outline the steps of the MInt algorithm in detail.

1. Initialize the full monodromy matrix to unity, $\mathbf{M}(0) = \mathbb{I}$, and the classical action to zero, $S(0) = 0$. Set the monodromy matrix for H_1 evolution $\mathbf{M}_{H_1}$

to the identity matrix plus off-diagonal elements given by Eq. 5.42. $\mathbf{M}_{H_1}$ remains in this form $\forall\ t$.

2. Evolve nuclear positions and the classical action for half a timestep with Eq. 5.22 and Eq. 5.23, respectively.
3. With the updated nuclear positions compute $\mathbf{V}$ as well as its eigenvalues, eigenvectors, derivative eigenvalues, and derivative eigenvectors.
4. Evolve the mapping variables with Eq. 5.28 and Eq. 5.29, and the nuclear momenta with Eq. 5.40.
5. Use Eq. 5.42-Eq. 5.50 and Eq. 5.53 to define the monodromy matrix for evolution under H_2, $\mathbf{M}_{H_2}$. The remaining diagonal elements are unity and all other elements are zero. Evolve the entire monodromy matrix with Eq. 5.57.
6. Evolve the classical action with Eq. 5.41.
7. Evolve the nuclear positions again for half a timestep with Eq. 5.22.
8. Repeat steps 2-7 as needed.

5.2.5 Other Properties

It can also be shown [82] that the MInt algorithm is symmetric and time reversible, both properties of exact Hamiltonian evolution. Like the velocity Verlet algorithm, it is second order in time step Δt and will therefore conserve energy with fluctuations of $O\left(\Delta t^2\right)$ without drifting. The algorithm is also explicit and, being symplectic, automatically satisfies Liouville's theorem. In addition, as noted for exact evolution under the MM-ST Hamiltonian [111], the MInt algorithm exactly conserves $\mathcal{G} := \mathbf{x}^{\mathrm{T}}\mathbf{x} + \mathbf{p}^{\mathrm{T}}\mathbf{p}$ and is therefore unitary, i.e., conserves

total electronic probability

$$\sum_{n=1}^{F} \mathcal{P}_n = \frac{1}{2} \sum_{n=1}^{F} x_n^2 + p_n^2 - 1, \tag{5.58}$$

for any length of time step. It is also invariant to the overall phase (or angle) of the mapping variables, i.e., the transformation

$$(\tilde{\mathbf{x}} + i\tilde{\mathbf{p}}) = e^{-i\theta} (\mathbf{x} + i\mathbf{p}), \tag{5.59}$$

where θ is a scalar. We note that this algorithm immediately extends to Hamiltonians containing a sum of Meyer-Miller-like terms such as the ring polymer Hamiltonians [82].

5.2.6 Numerical Performance

Here we test the numerical performance of the MInt algorithm on a two-state model system with one nuclear dof. Elements of the diabatic electronic potential energy matrix for this system are given by

$$V_{11}(R) = V_1 (1 + \tanh[R]), \tag{5.60}$$

$$V_{22}(R) = V_2 (1 - \tanh[R]), \tag{5.61}$$

$$V_{12}(R) = a e^{-(R+b)^2}, \tag{5.62}$$

and R is the nuclear coordinate. We choose $V_1 = 0.04$, $V_2 = 0.01$, $a = 0.005$, and $b = 0.7$. The surfaces and coupling provided in Eq. 5.60 through Eq. 5.62 are plotted in Fig. 5.1 as a function of the nuclear coordinate.

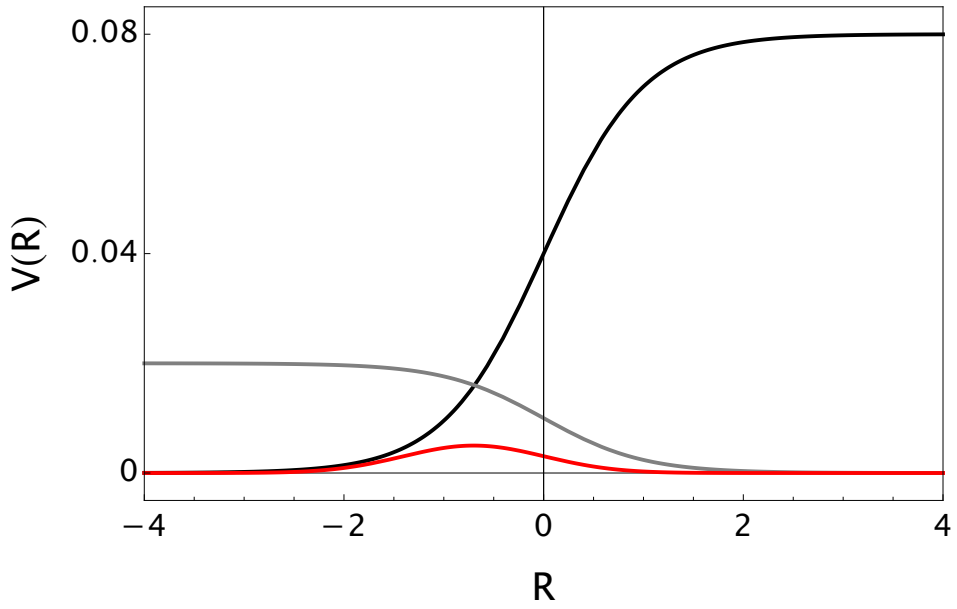

Figure 5.1: Elements of the diabatic electronic potential energy matrix are plotted as a function of the nuclear coordinate: $V_{11}(R)$ (black), $V_{22}(R)$ (gray), and $V_{12}(R) = V_{21}(R)$ (red).

In Fig. 5.2 we compare how the energy of a single trajectory behaves when computed with the MInt algorithm and when computed with a non-symplectic Adams predictor-corrector algorithm.

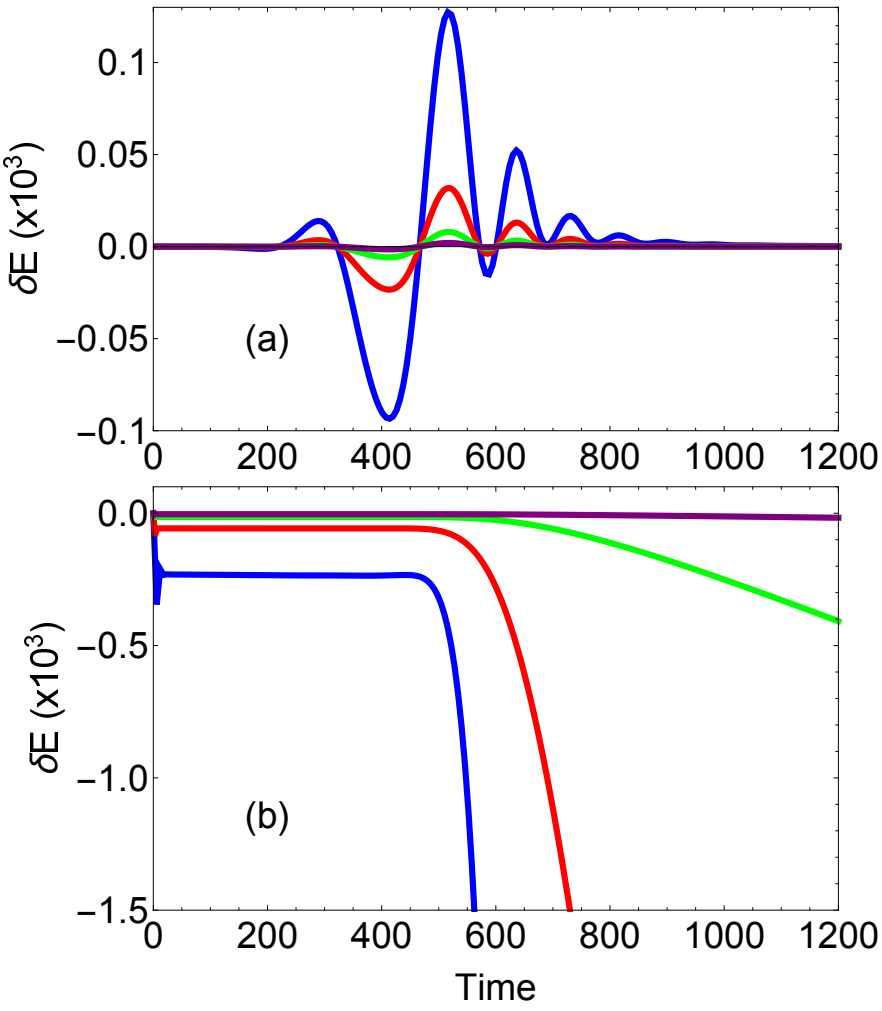

Figure 5.2: A comparison of how (a) the Mint algorithm and (b) the Adams propagator conserves energy along a single trajectory. Each curve corresponds to a different timestep Δt used during the simulation: 0.75 (purple), 1.5 (green), 3.0 (red), and 6.0 (blue).

The initial conditions of the trajectory are provided in Table 5.1.

Dof	Initial Position	Initial Momentum
Nuclear	−5.0	19.9
MV1	$-\sqrt{3}$	0.0
MV2	1.0	0.0

Table 5.1: The initial phase space points of the test trajectory.

We chose a trajectory whose nuclear component originates at the center of the nuclear wavepacket. The initial phase space points of the mapping variables were chosen so that the population estimators $\mathcal{P}_n = \frac{1}{2}\left(x_n^2 + p_n^2 - 1\right)$ for the lower and upper electronic states (to the left of the crossing) are equal to one and zero, respectively. The quantity we use to compare energy conservation between the two integration schemes is defined as

$$\delta E = 1 - E(0)/E(t). \tag{5.63}$$

Ideally δE should be zero at all times, but it is characteristic of a symplectic algorithm that δE oscillates about zero and does not drift over time [158], and the deviations of δE from zero are generally smaller with smaller time steps. It is clear from Fig. 5.2(a) that the MInt algorithm exhibits each of these characteristics; δE clearly oscillates around zero, particularly in the interaction region from time $t = 200$ to $t = 1000$, it does not drift, and its oscillations are diminished with smaller time steps. Note that the oscillations in δE are far less pronounced outside the interaction region, but this is intuitive considering that the potential energy surfaces of this model are flat and practically decoupled outside the interaction region.

Fig. 5.2(b) also plots δE as a function of time, but now computed with the Adams propagator. Clearly the Adams propagator does not exhibit characteristics of a symplectic integrator. Particularly for longer time steps, δE in Fig. 5.2(b) starts to dramatically drift from zero around the middle of the interaction region at $t = 500$, and does not return. And while the curve in Fig. 5.2(b) that corresponds to the smallest time step appears to be satisfactory, it still exhibits a subtle drifting effect.

Our second numerical test is for symplecticity, so we define the follow-

ing quantity to compare conservation of symplecticity between integration schemes,

$$\delta M = \text{maxval}\left[\mathbf{M}^{\mathrm{T}}\mathbf{J}^{-1}\mathbf{M} - \mathbf{J}^{-1}\right]. \tag{5.64}$$

By computing Eq. 5.64 along the trajectory we can determine the extent to which the given algorithm conserves the symplecticity criterion of Eq. 5.16. For the same trajectory as before we plot δM in Fig. 5.3(a) as computed with the MInt algorithm, and in Fig. 5.3(b) as computed with the Adams propagator.

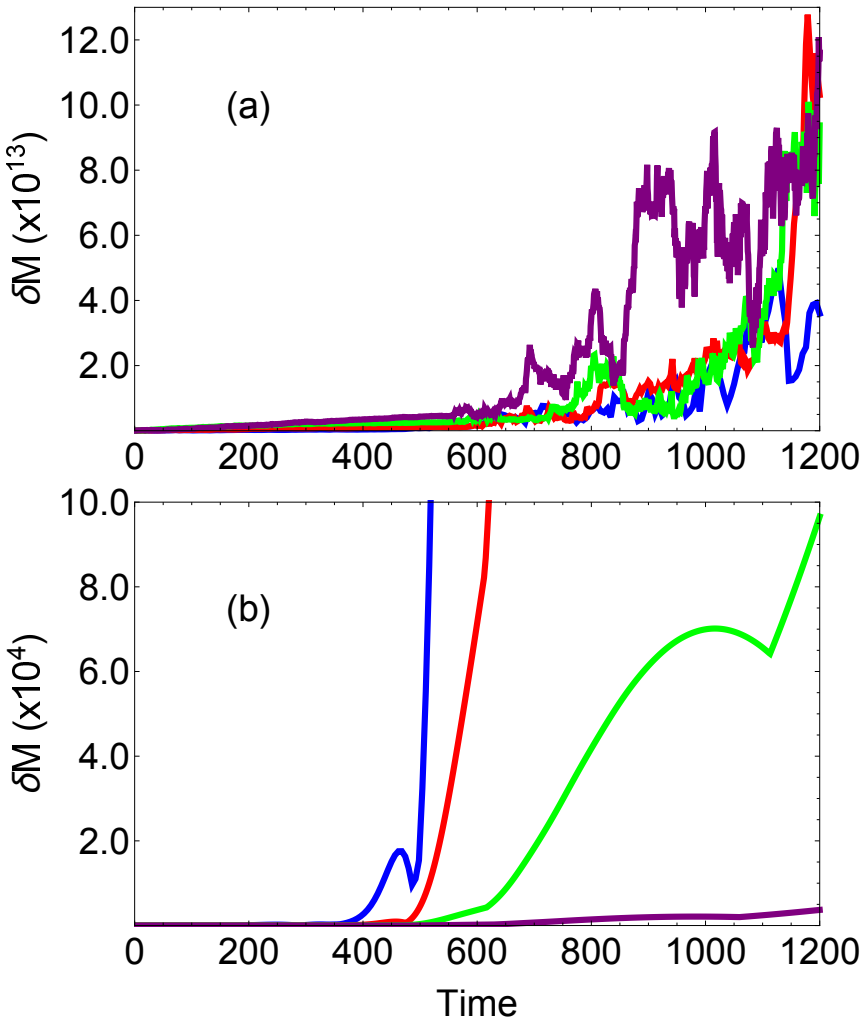

Figure 5.3: A comparison of how (a) the MInt algorithm and (b) the Adams propagator conserves the symplecticity criterion δM along a single trajectory. Each curve corresponds to a different timestep Δt used during the simulation: 0.75 (purple), 1.5 (green), 3.0 (red), and 6.0 (blue).

We see in Fig. 5.3(a) that deviations in δM from zero are on the order of machine precision for each time step used. This likely explains why the largest deviations occur when using a smaller time step, since more arithmetic is required when using a finer time grid. In any case, Fig. 5.3(a) shows that the MInt algorithm can sufficiently conserve the symplecticity criterion over a variety of

time steps. This is a much more appealing result than is shown in Fig. 5.3(b) where the Adams propagator is used to compute δM. In this case, a smaller time step gives a better result but the deviations of δM from zero are on the order of 10^{-3} through 10^{-5}, much larger than those found with the MInt algorithm in Fig. 5.3(a).

5.3 Nonadiabatic Dynamics with MQC-IVR

In this section we apply MQC-IVR and the MInt algorithm to the model nonadiabatic system described in Sec. 5.2.6. The initial state of the system is taken to be a nuclear coherent state that completely populates the lower electronic surface to the left of the interaction region. The upper surface to the left of the interaction region is initially unoccupied. The initial position-space wavefunction is therefore given by

$$\begin{aligned}\Psi_0(R, x_1, x_2) &= \langle R|R_i P_i\rangle \langle x_1|1_1\rangle \langle x_2|0_2\rangle \\ &= \left(\frac{\gamma}{\pi}\right)^{\frac{1}{4}} e^{-\frac{\gamma}{2}(R-R_i)^2 + iP_i(R-R_i)} \\ &\times \left(\frac{2}{\pi}\right)^{\frac{1}{2}} x_2 e^{-\frac{1}{2}x_1^2 - \frac{1}{2}x_2^2},\end{aligned} \tag{5.65}$$

and we choose $R_i = -5.0$, $P_i = 19.9$, and $\gamma = 0.25$. Operator $\hat{A}$ is then taken to be $\hat{A} = |R_i P_i 1_1 0_2\rangle \langle R_i P_i 1_1 0_2|$. In this section we take $\mathbf{c}_p = \mathbf{c}_q = \mathbf{c}$ in all simulations. When using elements of $\mathbf{c}$ less than 0.5, initial conditions are sampled from the following distribution,

$$\begin{aligned}\rho_1(\mathbf{z}_0, \mathbf{z}_0') =& N_1 e^{-\frac{\gamma}{4}(R_0-R_i)^2 - \frac{\gamma}{4}(R_0'-R_i)^2} e^{-\frac{1}{4\gamma}(P_0-P_i)^2 - \frac{1}{4\gamma}(P_0'-P_i)^2} \\ &\times e^{-\frac{1}{6}(x_{10}^2 + x_{10}'^2)} e^{-\frac{1}{6}(p_{10}^2 + p_{10}'^2)} e^{-\frac{1}{4}(x_{20}^2 + x_{20}'^2)} e^{-\frac{1}{4}(p_{20}^2 + p_{20}'^2)},\end{aligned} \tag{5.66}$$

and for all other choices of tuning parameters the initial conditions are sampled from a correlated sampling distribution,

$$\begin{aligned}\rho_2\left(\mathbf{z}_0,\mathbf{z}_0'\right) =& N_2 e^{-\frac{\gamma}{4}\left(\bar{R}_0-R_i\right)^2-\frac{1}{4\gamma}\left(\bar{P}_0-P_i\right)^2} e^{-\frac{c_N}{2}\Delta_R^2-\frac{c_N}{2}\Delta_P^2} \\ &\times e^{-\frac{1}{6}\bar{x}_{10}^2-\frac{1}{6}\bar{p}_{10}^2} e^{-\frac{c_1}{2}\Delta_{x_1}^2-\frac{c_1}{2}\Delta_{p_1}^2} e^{-\frac{1}{4}\bar{x}_{20}^2-\frac{1}{4}\bar{p}_{20}^2} e^{-\frac{c_2}{2}\Delta_{x_2}^2-\frac{c_2}{2}\Delta_{p_2}^2}. \end{aligned} \tag{5.67}$$

Constants N_1 and N_2 are for normalization. We take c_N to be the tuning parameter associated with the nuclear dof, and parameters c_1 and c_2 are the tuning parameters associated with the two mapping variables. In each simulation of this section we take $c_1 = c_2 = c_e$. With operator $\hat{B}$ defined as $\hat{B} = \delta\left(P_f - \hat{P}\right)$, we compute the particle's nuclear momentum distribution after the particle traverses the interaction region. The coherent state matrix element of operator $\hat{B}$ is

$$\begin{aligned}\left\langle \mathbf{z}_t'\right|\delta\left(P_f-\hat{P}\right)\left|\mathbf{z}_t\right\rangle &= \left\langle \mathbf{z}_t'\right|P_f\rangle\left\langle P_f\right|\mathbf{z}_t\rangle \\ &= \left(\frac{1}{\gamma\pi}\right)^{\frac{1}{2}} e^{-\frac{1}{2\gamma}\left(P_f-P_t'\right)^2+iP_fR_t'} e^{-\frac{1}{2\gamma}\left(P_f-P_t\right)^2-iP_fR_t} \\ &\times \prod_{j=1}^{2} e^{-\frac{1}{4}\left(x_{tj}'-x_{tj}\right)^2-\frac{1}{4}\left(p_{tj}'-p_{tj}\right)^2+\frac{i}{2}\left(x_{tj}'+x_{tj}\right)\left(p_{tj}'-p_{tj}\right)}. \end{aligned} \tag{5.68}$$

When using MQC-IVR to compute the population of the k^{th} electronic state we define operator $\hat{B}$ as $\hat{B} = \left|1_k 0_j\right\rangle\left\langle 1_k 0_j\right|$ with $k \neq j$. The matrix element of operator $\hat{B}$ in this case is given by

$$\begin{aligned}\left\langle \mathbf{z}_t'\right|1_k 0_j\rangle\left\langle 1_k 0_j\right|\mathbf{z}_t\rangle =& \frac{1}{2}\left(x_{tk}+ip_{tk}\right)\left(x_{tk}'-ip_{tk}'\right) \\ &\times e^{-\frac{1}{4}\left(x_{t1}^2+p_{t1}^2+x_{t2}^2+p_{t2}^2\right)} e^{-\frac{i}{2}\left(p_{t1}x_{t1}+p_{t2}x_{t2}\right)} \\ &\times e^{-\frac{1}{4}\left(x_{t1}'^2+p_{t1}'^2+x_{t2}'^2+p_{t2}'^2\right)} e^{+\frac{i}{2}\left(p_{t1}'x_{t1}'+p_{t2}'x_{t2}'\right)} \\ &\times \left\langle R_t'P_t'\right|R_tP_t\rangle. \end{aligned} \tag{5.69}$$

Fig. 5.4(a) plots the diabatic surfaces and the coupling between them. And

in Fig. 5.4(b)-(d) we plot the nuclear momentum distribution of the particle in the long-time limit, each with a different set of tuning parameters.

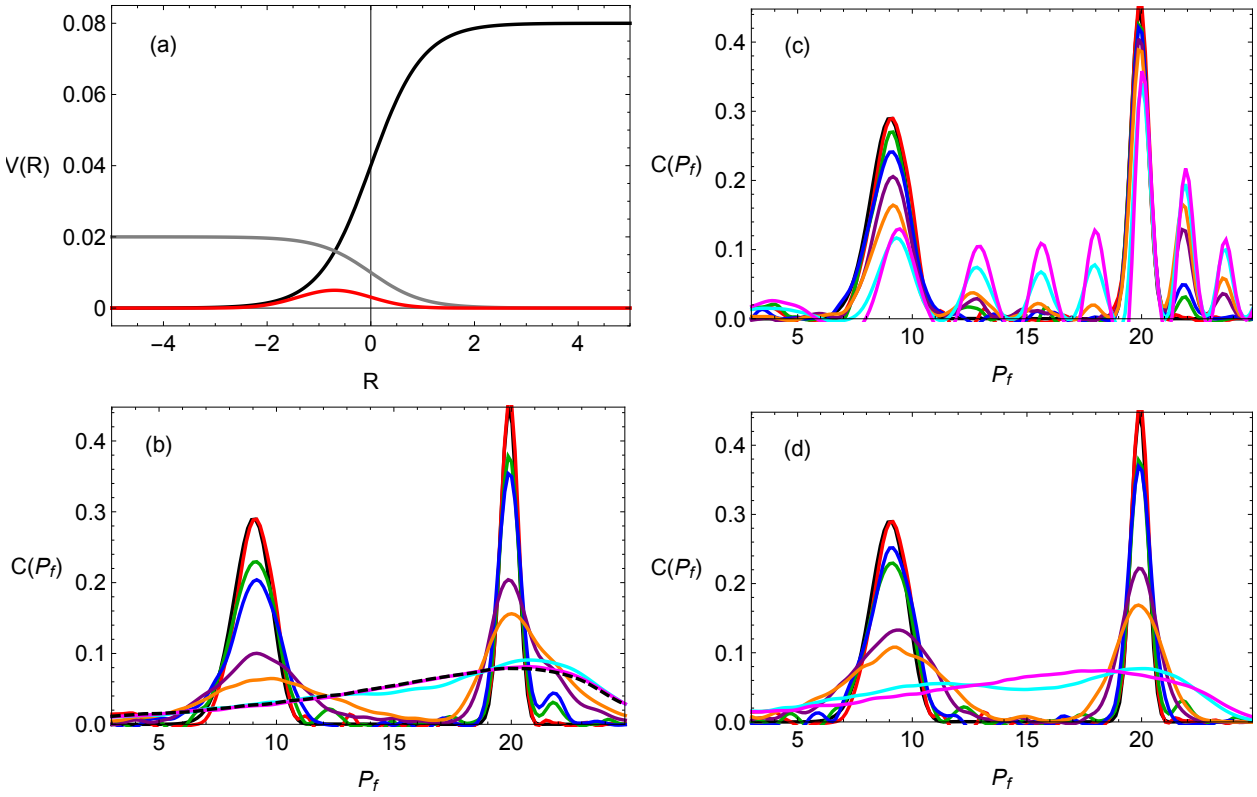

Figure 5.4: Panel (a) plots the diabatic surfaces and coupling of the model system. Panels (b)-(d) plot the nuclear momentum distribution obtained with exact quantum (black) and MQC-IVR with different sets of tuning parameters. In panel (b) we vary $c_N = c_e$, in (c) we fix $c_N = 0.01$ and vary c_e, and in (d) we fix $c_e = 0.01$ and vary c_N. Each color corresponds to a different value of the varied tuning parameter: 0.01 (red), 0.05 (green), 0.1 (blue), 0.5 (purple), 1.0 (orange), 10.0 (cyan), 100.0 (pink). Panel (b) also contains the Husimi-IVR result (black, dashed).

In Fig. 5.4(b), where each dof is treated with the same tuning parameter, it is clear that MQC-IVR smoothly interpolates between the discrete peak structure of the exact quantum result and the single broad distribution of the classical Husimi-IVR result. Furthermore, we show in Table 5.2 that an increase in the

tuning parameter coincides with computational savings, as expected.

$c_N = c_e$	N_{traj}
0.01	3×10^8
0.05	2×10^8
0.1	1×10^8
0.5	9×10^7
1.0	2×10^7
10.0	6×10^6
100.0	1.2×10^6

Table 5.2: The approximate number of trajectories needed for graphical convergence of the MQC-IVR results appearing in Fig. 5.4(b), where the nuclear and electronic dofs are treated with the same value of tuning parameter.

The MQC-IVR results of Fig. 5.4(c) and Fig. 5.4(d) were obtained by quantizing the nuclear and electronic dofs to different extents. In Fig. 5.4(c) we fix the nuclear tuning parameter near the quantum limit, $c_N = 0.01$, and vary the tuning parameter associated with the mapping variables. Reasonable results are obtained when c_e is as high as 0.1, but for $c_e > 0.1$ we see spurious peaks appear in unphysical regions of P_f. Interestingly, the envelope of these spurious peaks appears to resemble the shape of the Husimi-IVR result in Fig. 5.4(b). As was seen with the results in Fig. 5.4(b), we see in Table 5.3 that, even the though nuclear tuning parameter is fixed near the quantum limit, an increase in the value of the tuning parameter associated with the mapping variables results in computational savings.

c_e	N_{traj}
0.05	8×10^7
0.1	5×10^7
0.5	1×10^7
1.0	6×10^6
10.0	2×10^6
100.0	1×10^6

Table 5.3: The approximate number of trajectories needed for graphical convergence of the MQC-IVR results appearing in Fig. 5.4(c), where the nuclear tuning parameter is fixed near the quantum limit, $c_N = 0.01$, and the tuning parameter associated with the mapping variables are varied.

We note that the trend in Fig. 5.4(c) contrasts with some of the results of the adiabatic model systems studied in previous sections. We had previously concluded in the adiabatic systems that unobserved dofs could be treated very close to the classical limit, with very large tuning parameters, without sacrificing a significant amount of accuracy. In the current nonadiabatic model, however, the mapping variables, which are unobserved dofs, cannot be treated as close to the classical limit as we would like. This is most likely a reflection of the strong coupling between the mapping variables and the nuclear dof as defined in the MM-ST Hamiltonian. We must therefore conclude that the mapping variables of a nonadiabatic system, even when not observed with operator $\hat{B}$, must be treated near the quantum limit for an accurate quantum mechanical description of the dynamics. Despite having to make this sacrifice, though, it is clear that MQC-IVR is capable of describing the dynamics accurately, and with reasonable computational expense.

In Fig. 5.4(d) we fix the electronic tuning parameter near the quantum limit, $c_e = 0.01$, and vary the tuning parameter associated with the nuclear dof. These

results are very similar to those seen in Fig. 5.4(b), where each dof is treated with the same tuning parameter; it is clear again that MQC-IVR smoothly interpolates between the discrete peak structure of the quantum result and the broad distribution of the classical Husimi-IVR result. And again we see in Table 5.4 that any increase in value of the nuclear tuning parameter results in computational savings.

c_N	N_{traj}
0.05	9×10^8
0.1	6×10^8
0.5	4×10^8
1.0	1×10^8
10.0	7×10^7
100.0	2×10^7

Table 5.4: The approximate number of trajectories needed for graphical convergence of the MQC-IVR results appearing in Fig. 5.4(d), where the tuning parameter associated with the mapping variable is fixed near the quantum limit, $c_e = 0.01$, and the tuning parameter associated with the nuclear dof is varied.

It is clear from Tab. 5.2, Tab. 5.3, and Tab. 5.4 that the largest extent of computational savings comes from increasing the value of the tuning parameter associated with the mapping variables. This trend should, however, be system-dependent, i.e. depend upon the ratio of nuclear to electronic dofs. The current model contains more mapping variables than nuclear dofs, and so the trend is intuitive.

In Fig. 5.5 we plot the populations of each electronic state as a function of time, as computed with MQC-IVR with different sets of tuning parameters.

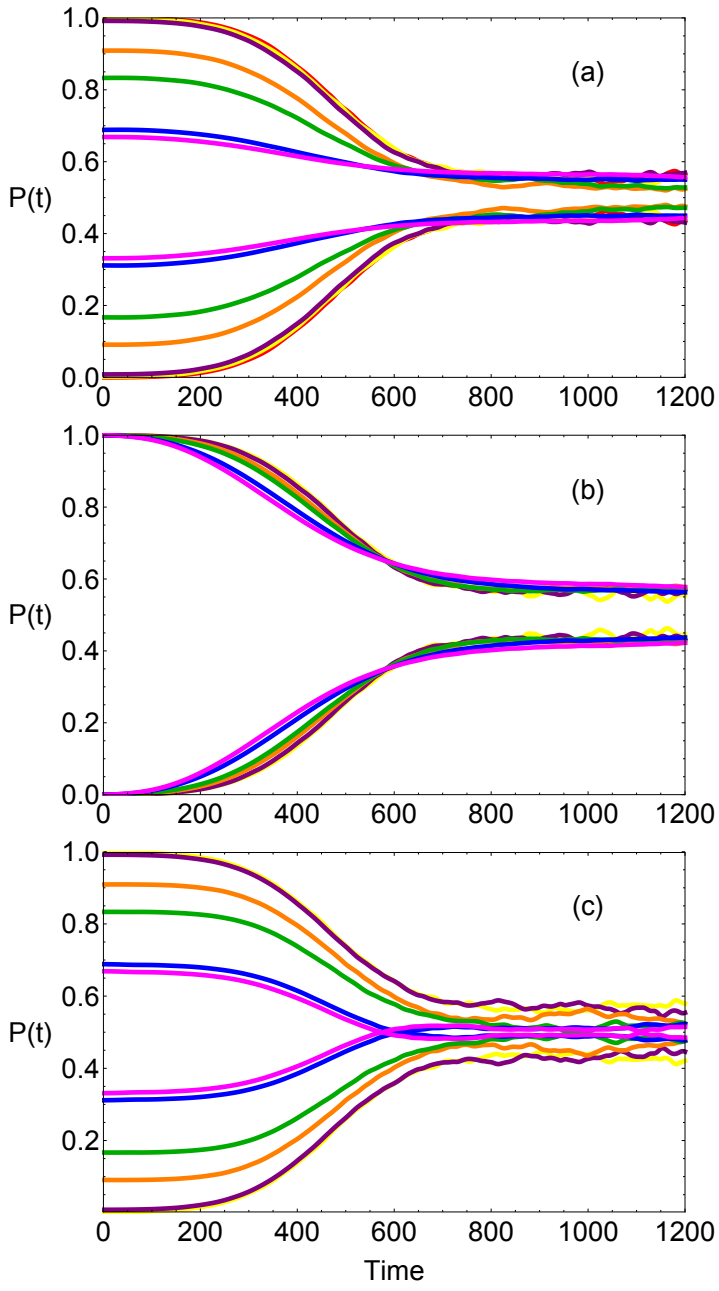

Figure 5.5: The populations of both electronic states, as computed with MQC-IVR, are plotted as a function of time. Results in panel (a) are obtained with varied $c_N = c_e$, panel (b) with $c_e = 0.01$ and varied c_N, and panel (c) with $c_N = 0.01$ and varied c_e. Each color corresponds to a different value of the varied tuning parameter: 0.01 (red), 0.05 (purple), 0.1 (yellow), 0.5 (orange), 1.0 (green), 10.0 (blue), and 100.0 (pink). The Husimi-IVR result in panel (a) rests behind the pink curve associated with $c_N = c_e = 100.0$. The exact quantum result (black) is directly beneath the quantum limit MQC-IVR results.

In Fig. 5.5(a), where each dof is treated with the same tuning parameter, we see again that MQC-IVR smoothly interpolates between the quantum and classical limits, and the long-time behavior of each result is quantitatively accurate. The short-time behavior of the more classical MQC-IVR results, however, is clearly inaccurate. We see that when $c_N = c_e$ is increased to 0.5 and higher, the particle initially occupies both electronic states, which is inconsistent with our definition of the initial state of the system. We can determine the origin of the inconsistency by looking at different sets of tuning parameters.

The MQC-IVR results of Fig. 5.5(b) are obtained by fixing the tuning parameter associated with the mapping variables near the quantum limit, and varying the tuning parameter of the nuclear dof. In this case, the short-time behavior of each result is consistent with the definition of the initial state of the system: unit population of one electronic state, and zero population in the other. Furthermore, the long-time limit of the MQC-IVR results in Fig. 5.5(b) are all quantitatively accurate, even when the nuclear dof is treated close to the classical limit. The biggest discrepancy between these results, though fairly subtle, exist when the particle traverses the interaction region around $t = 100$ to $t = 600$. Here, the classical limit offers an underestimation of the population of the initially occupied state, and an overestimation of the population of the initially unoccupied state.

The MQC-IVR results of Fig. 5.5(c) are obtained by fixing the tuning parameter associated with the nuclear dof near the quantum limit, and varying the tuning parameter associated with the mapping variables. Here we see the same short-time inconsistencies in the classical limit results as observed in Fig. 5.5(a). Given this, and given the accurate short-time results of Fig. 5.5(b), we can con-

clude that inconsistencies in the initial electronic state populations arise when the mapping variables are treated closer to the classical limit. This conclusion supplements the conclusion drawn from Fig. 5.4; that treating the mapping variables near the quantum limit is required for an accurate description of the problem.

CHAPTER 6

THE SC CORR-CODE PACKAGE

6.1 Introduction

The SC Corr-Code Package [160] is an open source FORTRAN-based program that computes the real-time correlation function under a variety of SC-IVR approximations for both adiabatic and nonadiabatic model systems. In this chapter we offer an overview of the program and explain how it can be modified, but detailed documentation is provided elsewhere [160]. The main purpose of the program is to provide base-line code for implementing SC-IVRs on general complex chemical systems with analytical forces; but the code itself and the available model systems are simple enough for beginners to understand and learn from.

The available SC-IVRs are DHK-IVR (within the DF implementation),

$$C_{AB}(t) = \frac{1}{(2\pi)^{2N}} \int d\mathbf{z}_0 \int d\mathbf{z}_0' \, \langle \mathbf{z}_0 | \hat{A} | \mathbf{z}_0' \rangle \, \langle \mathbf{z}_t' | \hat{B} | \mathbf{z}_t \rangle \, e^{i[S_t(\mathbf{z}_0) - S_t(\mathbf{z}_0')]} C_t(\mathbf{z}_0; \gamma_0) \, C_t^*(\mathbf{z}_0'; \gamma_0) \,, \tag{6.1}$$

Husimi-IVR,

$$C_{AB}(t) = \frac{1}{(2\pi)^{N}} \int d\mathbf{z}_0 \, \langle \mathbf{z}_0 | \hat{A} | \mathbf{z}_0 \rangle \, \langle \mathbf{z}_t | \hat{B} | \mathbf{z}_t \rangle \,, \tag{6.2}$$

LSC-IVR,

$$C_{AB}(t) = \frac{1}{(2\pi)^{N}} \int d\mathbf{z}_0 \, A_W(\mathbf{z}_0) \, B_W(\mathbf{z}_t) \tag{6.3}$$

(see Eq. 1.63 for the Wigner transform $\Omega_W\left(\mathbf{z}_0\right)$ of a general operator $\hat{\Omega}$), MQC-

IVR,

$$C_{AB}(t) = \frac{1}{(2\pi)^{2N}} \int d\mathbf{z}_0 \int d\mathbf{z}'_0 \, \langle \mathbf{z}_0 | \hat{A} | \mathbf{z}'_0 \rangle \, \langle \mathbf{z}'_t | \hat{B} | \mathbf{z}_t \rangle \, e^{i[S_t(\mathbf{z}_0) - S_t(\mathbf{z}'_0)]} D_t^{DF}(\mathbf{z}_0, \mathbf{z}'_0; \gamma_0, \mathbf{c}) \, e^{-\frac{1}{2}\boldsymbol{\Delta}^{\mathrm{T}} \mathbf{c} \boldsymbol{\Delta}}, \tag{6.4}$$

FB MQC-IVR,

$$C_{AB}(t) = \frac{1}{(2\pi)^{2N}} \int d\mathbf{z}_0 \int d\mathbf{z}'_t \, \langle \mathbf{z}_0 | \hat{A} | \mathbf{z}'_0 \rangle \, \langle \mathbf{z}'_t | \hat{B} | \mathbf{z}_t \rangle \, e^{i[S_t(\mathbf{z}_0) + S_{-t}(\mathbf{z}'_t)]} D_t^{FB}(\mathbf{z}_0, \mathbf{z}'_t; \gamma_0, \mathbf{c}) \, e^{-\frac{1}{2}\boldsymbol{\Delta}_t^{\mathrm{T}} \mathbf{c} \boldsymbol{\Delta}_t}, \tag{6.5}$$

and AMQC-IVR,

$$\begin{aligned} C_{AB}(t) = & \frac{1}{(2\pi)^{N+F}} \int d\mathbf{z}_0 \int dz'_1 \ldots \int dz'_F \, \langle \mathbf{z}_0 | \hat{A} | z'_1 \ldots z'_F z_{F+1} \ldots z_N \rangle \, B_{\mathbf{z}'_t \mathbf{z}_t} \\ & \times C_t(\mathbf{z}_0) \, C_t^*(z'_1, \ldots, z'_F, z_{F+1}, \ldots, z_N) \, e^{i[S_t(\mathbf{z}_0) - S_t(z'_1, \ldots, z'_F, z_{F+1}, \ldots, z_N)]} \\ & \times \Lambda_t(\mathbf{z}_0, z'_1, \ldots, z'_F) \, . \end{aligned} \tag{6.6}$$

Three adiabatic model systems are available. The 1D harmonic oscillator,

$$\hat{H} = \frac{1}{2m}\hat{p}^2 + \frac{1}{2}m\omega^2\hat{x}^2, \tag{6.7}$$

with a default frequency $\omega = \sqrt{2}$; a 1D anharmonic oscillator,

$$\hat{H} = \frac{1}{2m}\hat{p}^2 + \frac{1}{2}m\omega^2\hat{x}^2 - cx^3 + cx^4, \tag{6.8}$$

with default parameters $\omega = \sqrt{2}$ and $c = 0.1$; and a 2D system of coupled oscillators,

$$\hat{H} = \frac{1}{2m_1}\hat{p_1}^2 + \frac{1}{2m_2}\hat{p_2}^2 + \frac{1}{2}m_1\omega_1^2\hat{x}_1^2 - cx_1^3 + cx_1^4 + \frac{1}{2}m_2\omega_2^2x_2^2 + kx_1x_2, \tag{6.9}$$

with default parameters $\omega_1 = \sqrt{2}$, $c = 0.1$, $\omega_2 = \frac{1}{3}$, and $k = 1.0$. Each of the aforementioned default parameters are hard-coded into the program, but are easily changed, as will be described below. The mass of each dof, the coherent state width parameters, and the tuning parameters (if necessary) are specified in

the input file, as will be described below as well. The initial state of each dof in each model system is a coherent state, whose centers are specified in the input file.

One nonadiabatic model system with two electronic states and one nuclear dof is provided as well. The elements of the diabatic electronic potential energy matrix for this model are given by

$$V_{11}(R) = V_1(1 + \tanh[aR]), \tag{6.10}$$

$$V_{22}(R) = V_2(1 - \tanh[aR]), \tag{6.11}$$

$$V_{12}(R) = ge^{-b(R+f)^2}. \tag{6.12}$$

All system parameters for this model are specified in the input file. The initial state of the nuclear dof is a coherent state, and the mapping variables are initialized with a single excitation in state 1 and a ground state configuration in state 2. The program also uses the MInt algorithm of Chapter 5 to evolve trajectories and their associated monodromy matrix.

6.2 Generating and Running a Simulation

In the parent directory there is an input file named `theory.in` whose contents resembles what follows.

```
Degrees of freedom ( ...
1
Level of theory ( ...
2
```

```
Implementation ( ...
1
Type of observable ( ...
1
Model Potentials ( ...
2
List the diagonal ...
1.0
List the coherent state and ...
1.0     0.0     1.414     1.414     10.0     10.0
Timestep, number of timesteps, ...
0.05     1400     1e-5
Number of trajectories
120000
```

Within this file the user specifies the system dimensionality, the SC-IVR methodology, the model system, the implementation, the observable $\hat{B}$ (default options are position and momentum operators), and other general system/convergence parameters such as the mass, time grid, number of trajectories, etc. After specifying each of these details, running the command `sh execute.sh` in the parent directory will then generate a new directory named `EXPERIMENT`, in which is the specified program. Note that the command `sh execute.sh` will overwrite an existing `EXPERIMENT` directory, so care should be taken to rename the `EXPERIMENT` directory with the command `mv EXPERIMENT new_name`. Within the `EXPERIMENT` directory, the command `make` will compile the program, and the subsequent command `./dyn.x` will start the simulation. The script named `jobrun.sh` can be used for parallelized jobs, but see the docu-

mentation [160] for more details.

In order to generate a program that simulates a system outside of the default options, we recommend that the user first uses the default options to generate an `EXPERIMENT` directory, and subsequently edit the appropriate `.f90` files within that directory (such as the `potential.f90` file to edit the potential energy function, the `supply.f90` file to edit the coherent state matrix element of operator $\hat{B}$, the `MonteCarlo.f90` file to edit the sampling routine, and etc.). We strongly suggest that the user does not edit or move any file or directory outside of a given `EXPERIMENT` directory. Please visit the documentation manual [160] for a detailed description of the contents of a general `EXPERIMENT` directory, and for helpful tutorials as well.

CHAPTER 7

ONGOING PROJECTS AND CONCLUDING REMARKS

7.1 Nonadiabatic Energy Transfer at Metal Surfaces

Computational approaches to elucidating complex chemistry at metal surfaces can potentially be an effective avenue for screening new and useful materials, or the design and optimization of effective new catalysts. The high dimensionality of such systems, however, prohibits an exact quantum mechanical treatment, and the necessity of an accurate description of quantum effects (for example, the inclusion of vibrational quanta and/or the breakdown of the BO approximation) renders classical MD an unviable approach. Leading computational models therefore rely on a set of assumptions to reduce the dimensionality of the problem, such as neglecting the motion of surface atoms, restricting the region of adsorbate dynamics, considering the motion of a select-few important reactant dofs, and simplifying the complexity of nonadiabatic effects (if applicable) [8]. In this section we summarize ongoing work in applying SC-IVR methodologies to a well-studied example of nonadiabatic chemistry at a metal surface: the multi-quantum transfer of vibrational energy from NO into electronic excitations on an Au(111) surface during a collision [8,161–167].

A number of promising theoretical treatments of the problem have been developed over the past few decades. Of those, MD with electronic frictions [168,169] and independent electron surface hopping [170–172] have done well in reproducing certain experimental results, but have also been shown to fail in, for example, predicting certain vibrational state-to-state branching ratios [8]. It is therefore clear that a consistent and efficient theoretical approach to prob-

lems in surface chemistry is still wanting. And given the dynamical consistency of SC-IVR methods, and the ability of SC-IVR methods to include an accurate description of virtually all quantum effects in both adiabatic and nonadiabatic systems, SC-IVRs are an appealing, yet un-tested, approach to these problems.

7.1.1 The Model

The model we use is that of Fuemmeler [173], which we briefly summarize here. Three terms are used in the ground-state Hamiltonian of the NO/Au(111) system:

$$H = H_{Newns} + H_{NO} + H_{nuc}. \tag{7.1}$$

The first term in Eq. 7.1 is a Newns Hamiltonian [174] describing the effective orbital energy of the incoming NO molecule, the second term includes the full potential energy surface of a free NO molecule, and the third term describes nuclear repulsions between the NO molecule and the metal surface. The model contains two nuclear dofs: the NO bond length R and the metal-molecule distance Z. The ground state energy and wavefunction are obtained by diagonalizing the total Hamiltonian on a grid of the two nuclear coordinates. Subsequently, a clever use of the Schmidt decomposition [175] is used to construct two localized diabatic electronic states and their coupling [173]:

$$V_{11}(R,Z) = D_1 f_1(R)^2 + g_1(Z), \tag{7.2}$$

$$V_{22}(R,Z) = D_2 f_2(R)^2 + g_2(Z) - c(R,Z), \tag{7.3}$$

$$V_{12}(R,Z) = b(R,Z), \tag{7.4}$$

with

$$f_i(R) = \left(1 - e^{-A_i(R-R_{ei})}\right), \tag{7.5}$$

$$g_i(Z) = \frac{\alpha_i}{Z} e^{-\beta_i Z}, \tag{7.6}$$

$$c(R,Z) = \frac{1}{4\left(\Delta(R,Z) - \gamma_2\right)} \left(1 - e^{-\epsilon_2(\Delta(R,Z)-\gamma_2)}\right) \zeta_2 - \delta_2 \tag{7.7}$$

$$\Delta(R,Z) = \eta_1 Z + \eta_2 (Z + R), \tag{7.8}$$

$$b(R,Z) = \alpha_c e^{-\beta_c Z - \gamma_c R} + \delta_c, \tag{7.9}$$

$\forall\, i \in [1,2]$. Numerical parameters for each state and their coupling are provided in Table C.1 in Appendix C.

7.1.2 Numerical Tests

Here we consider classical limit versions of the SC-IVR time-correlation function, in tandem with the MM-ST Hamiltonian and the MInt algorithm, with which to test on this model: LSC-IVR and Husimi-IVR. In each case, we initialize the R-coordinate of the NO molecule in a particular vibrational eigenstate n within its ground-state electronic configuration. For the free NO molecule, these vibrational eigenstates are those of the Morse potential:

$$\begin{aligned}\langle R|n\rangle =& 2^{\lambda-n-\frac{1}{2}} \sqrt{A_1} e^{-\lambda e^{-A_1(R-R_{e1})}} \left(\lambda e^{-A_1(R-R_{e1})}\right)^{\lambda-n-\frac{1}{2}} \\ & \sqrt{\frac{(2\lambda - 2n - 1)\,\Gamma(n+1)}{\Gamma(2\lambda - n)}} L_n^{2\lambda-2n-1}\left(2\lambda e^{-A_1(R-R_{e1})}\right),\end{aligned} \tag{7.10}$$

with dimensionless parameter λ given by

$$\lambda = \frac{\sqrt{2\mu D_1}}{A_1 \hbar} = 48.03, \tag{7.11}$$

$\Gamma(x)$ is the gamma function of x, and $L_n^{\alpha}(x)$ is the n^{th} associated Laguerre polynomial in x. The translational coordinate Z is initialized in a coherent state centered

around the point (Z_i, P_{Zi}),

$$\langle Z|P_{Zi}Z_i\rangle = \left(\frac{\gamma_Z}{\pi}\right)^{\frac{1}{4}} e^{-\frac{\gamma_Z}{2}(Z-Z_i)^2+iP_{Zi}(Z-Z_i)}, \tag{7.12}$$

with $\gamma_Z = 4.4$, $Z_i = 5.0$, and $P_{Zi} = -20.5$ or $P_{Zi} = -28.3$ (so that the initial translation energy is approximately 0.1 eV or 0.2 eV, respectively). The total initial wave function therefore is a product of Eq. 7.10 and Eq. 7.12 that completely populates the ground electronic state,

$$\Psi_0(R, Z, x_1, x_2) = \langle R|n\rangle \langle Z|P_{Zi}Z_i\rangle \langle x_1 x_2|1_1 0_2\rangle, \tag{7.13}$$

with (x_1, p_1) and (x_2, p_2) being the mapping variables associated with ground and first excited electronic states, respectively. We take operator $\hat{A}$ to be a projector of the initial state,

$$\hat{A} = |n, P_{Zi}Z_i, 1_1 0_2\rangle \langle n, P_{Zi}Z_i, 1_1 0_2|. \tag{7.14}$$

When using LSC-IVR, initial conditions for the nuclear dofs are sampled directly from the Wigner transform of $\hat{A}$. The Wigner transform of the Morse eigenstate projector is evaluated by quadrature, and an analytical form of the Wigner transform of the coherent state projector is known to be

$$\mathcal{P}_{CS}(Z_0, P_{Z0}) \propto e^{-\gamma_Z Z_0^2 - \frac{1}{\gamma_Z}P_{Z0}^2}. \tag{7.15}$$

When using Husimi-IVR, the Husimi transform of the Morse eigenstate projector is evaluated by expanding the Morse eigenstates in a truncated basis of harmonic oscillator states; sixty terms were more than sufficient in each case.

The reliability of the classical trajectories in this model (with respect to conservation of energy and symplecticity) is very sensitive to sampling of the mapping variables' initial conditions. We have found, however, that the dynamics are stabilized when the mapping variables are sampled from a distribution that

constrains the initial population estimators of the ground and first excited states, $\mathcal{P}_j = \frac{1}{2}\left(x_j^2 + p_j^2 - 1\right) \forall\ j \in [1, 2]$, to one and zero, respectively. Therefore the initial conditions of the mapping variables are sampled from

$$\Omega_1(x_{10}, p_{10}) = \mathcal{P}_1\left(x_{10}, p_{10}\right) \delta\left(x_{10}^2 + p_{10}^2 - 3\right), \tag{7.16}$$

$$\Omega_2(x_{20}, p_{20}) = \mathcal{P}_2\left(x_{20}, p_{20}\right) \delta\left(x_{20}^2 + p_{20}^2 - 1\right), \tag{7.17}$$

where $\mathcal{P}_1\left(x_{10}, p_{10}\right)$ is the Wigner (or Husimi) transform of $|1_1\rangle\langle 1_1|$ and $\mathcal{P}_2\left(x_{20}, p_{20}\right)$ is the Wigner (or Husimi) transform of $|0_2\rangle\langle 0_2|$. We also take $\hat{B} = \hat{R}$ to compute the expectation value of the NO bond length, $\hat{B} = \hat{Z}$ to compute the average NO-metal distance, and $\hat{B} = |n\rangle\langle n|$ to compute the survival probability of the initial vibrational state, and $\hat{B} = |1_j 0_k\rangle\langle 1_j 0_k|$ to compute the population of the j^{th} electronic state, each as a function of time.

In Fig. 7.1 we plot $\langle\hat{R}\rangle_t$, $\langle\hat{Z}\rangle_t$, the survival probability of the initial vibrational eigenstate $P_S\left(t\right)$, and the electronic state populations $P_e\left(t\right)$ as a function of time with three different initial vibrational states ($n = 0$, $n = 3$, and $n = 15$) and with an initial translational energy of 0.1 eV. Fig. 7.2 plots the same quantities as in Fig. 7.1 but with an initial translational energy of 0.2 eV.

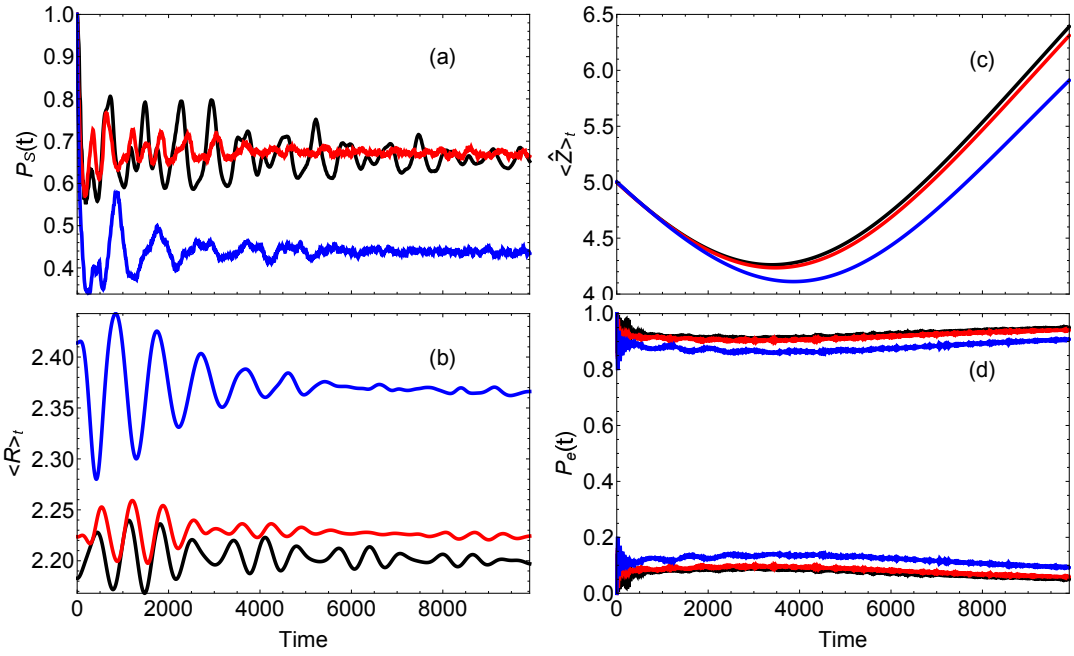

Figure 7.1: The LSC-IVR results of the (a) survival amplitude of the initial vibrational eigenstate, (b) the average NO bond length, (c) the average NO-metal distance, and (d) the electronic state populations. Each color corresponds to a different initial vibrational eigenstate: $n = 0$ (black), $n = 3$ (red), and $n = 15$ (blue).

Each vibrational survival probability in Fig. 7.1(a) and Fig. 7.2(a) quickly falls from unity at very short times, which suggests that LSC-IVR is not correctly capturing the quantum mechanical vibrational state of the NO molecule. Given that the NO molecule is prepared in an eigenstate of the vibrational Hamiltonian in the ground electronic state, and given that, in the ground electronic state, the translational coordinate Z is separated from the vibrational coordinate R, one would expect $P_S\ (t)$ to be equal to unity until the molecule nears the interaction region, rather than fall from unity as quickly as it does in the case of LSC-IVR.

A comparison of the expectation value of the NO bond length in Fig. 7.1(b) and Fig. 7.2(b) with the exact quantum results of Fuemmeler [173] also suggests that LSC-IVR is not correctly capturing the vibrational structure of the

NO molecule, which should oscillate around the equilibrium bond length of its initial eigenstate, then stretch in the interaction region, and return to its equilibrium bond length after the collision [173].

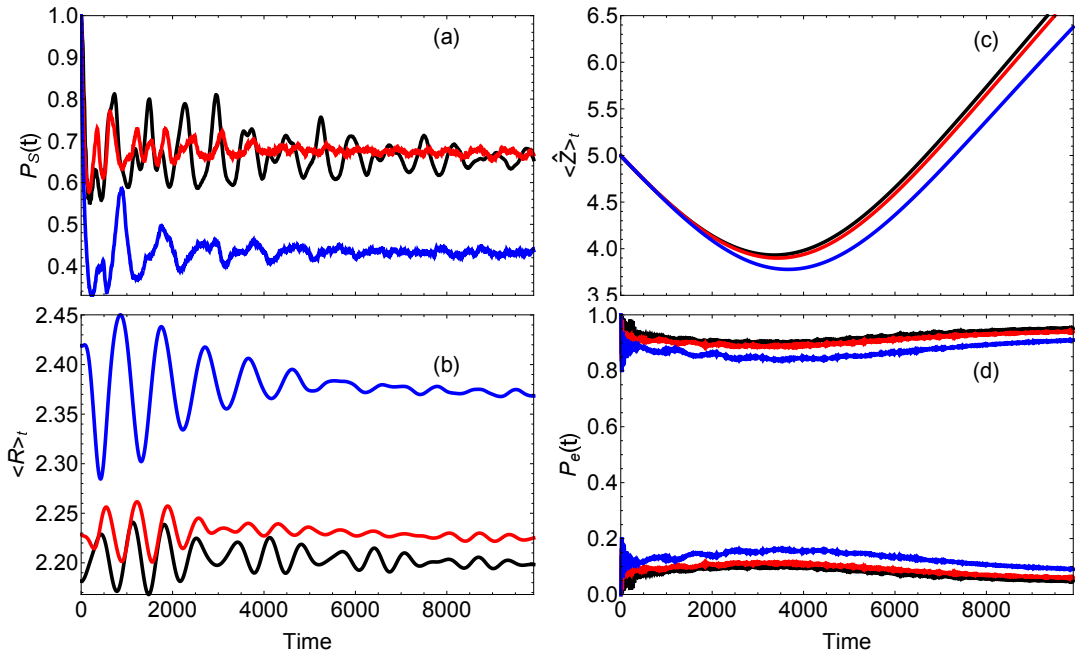

Figure 7.2: The LSC-IVR results of the (a) survival amplitude of the initial vibrational eigenstate, (b) the average NO bond length, (c) the average NO-metal distance, and (d) the electronic state populations. Each color corresponds to a different initial vibrational eigenstate: $n = 0$ (black), $n = 3$ (red), and $n = 15$ (blue).

The LSC-IVR results for the expectation value of the translational coordinate in Fig. 7.1(c) and Fig. 7.2(c), however, appear to be physically reasonable, and qualitatively similar to the exact quantum results of Fuemmeler [173]. Note that the minimum distances of the $\langle \hat{Z} \rangle_t$ results (around $t = 4000$) associated with the highest initial vibrational state in Fig. 7.1(c) and Fig. 7.2(c) are smaller than those associated with the lower initial vibrational states. This feature is seen in the exact quantum results [173], and, since the coupling between the two electronic states is stronger as molecule is closer to the metal surface, it likely agrees

with the experimental observation that more initial vibrational quanta stored in the NO molecule coincides with a higher probability of electronic excitation. This is further supported by the electronic state populations of Fig. 7.1(d) and Fig. 7.2(d), in which a larger transfer of state population is observed with more initial vibrational quanta. However, the results in Fig. 7.1(d) and Fig. 7.2(d) are not in quantitative agreement with the exact quantum results [173], which shows a larger transfer of population when the NO molecule is initially prepared in the $n = 15$ vibrational state.

The above analysis is now repeated with Husimi-IVR, the results of which are plotted in Fig. 7.3 and Fig. 7.4.

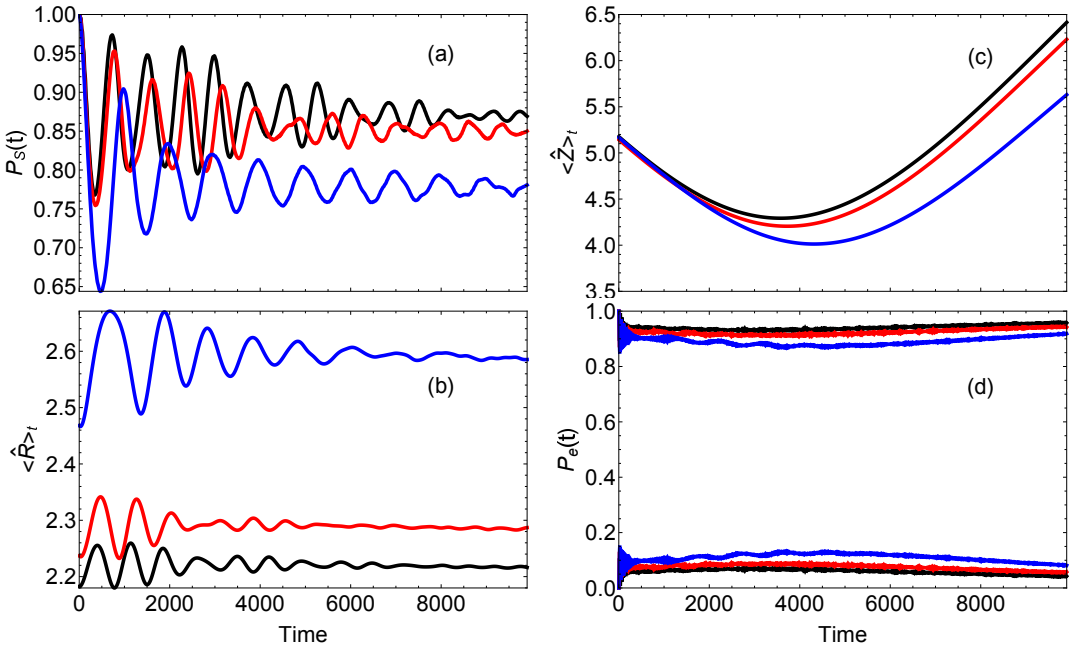

Figure 7.3: The Husimi-IVR results of the (a) survival amplitude of the initial vibrational eigenstate, (b) the average NO bond length, (c) the average NO-metal distance, and (d) the electronic state populations. Each color corresponds to a different initial vibrational eigenstate: $n = 0$ (black), $n = 3$ (red), and $n = 15$ (blue).

The Husimi-IVR and LSC-IVR results appear to be qualitatively similar in

each case, save that the initial drop in vibrational survival probability contained in the Husimi-IVR results is less drastic than that in the LSC-IVR results. As in the case of LSC-IVR, we see from the $\langle \hat{Z} \rangle_t$ results that an NO molecule that is prepared in the largest initial vibrational eigenstate gives rise to further penetration into the metal surface during the collision and, consequently, a larger transfer of electronic state population. The Husimi-IVR results for $\langle \hat{R} \rangle_t$ and the electronic state populations are not, however, in quantitative agreement with the exact results [173].

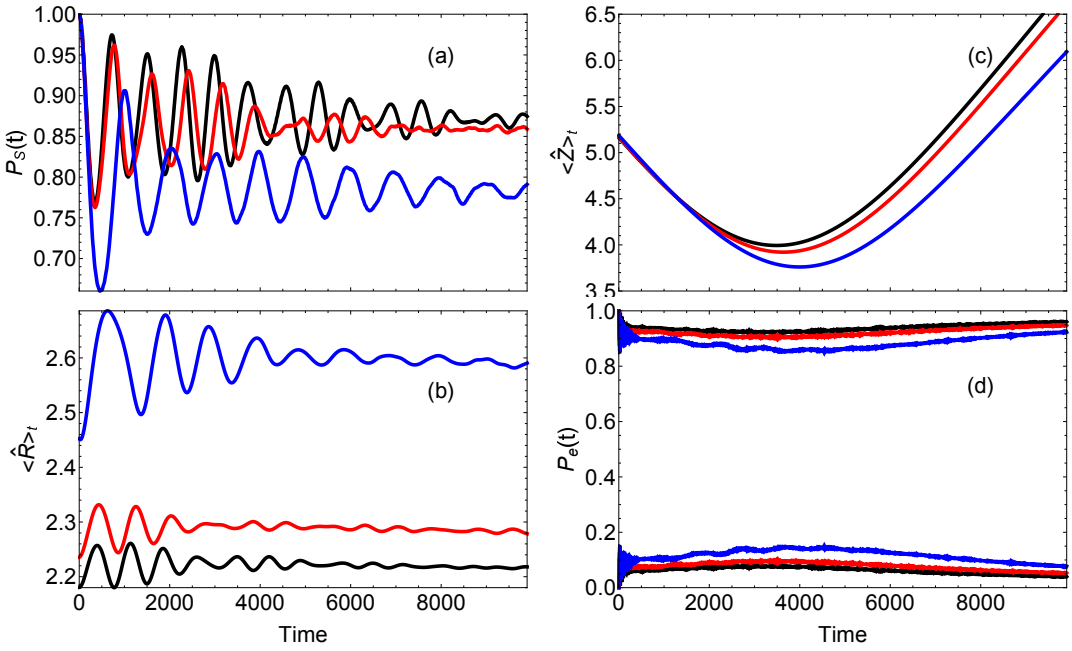

Figure 7.4: The Husimi-IVR results of the (a) survival amplitude of the initial vibrational eigenstate, (b) the average NO bond length, (c) the average NO-metal distance, and (d) the electronic state populations. Each color corresponds to a different initial vibrational eigenstate: $n = 0$ (black), $n = 3$ (red), and $n = 15$ (blue).

We can conclude from this analysis that classical limit SC-IVR time-correlation functions are not sufficient for an accurate description of the dynamics in this model. It is therefore likely that the phase information of other

SC-IVR methods, such as MQC-IVR and AMQC-IVR, could give rise to more accurate results, particularly those associated with NO vibrations. And since LSC-IVR and Husimi-IVR produce reasonable results for the expectation value of the NO-metal distance, it may be sufficient to treat the Z-coordinate in the classical limit when using MQC-IVR and AMQC-IVR.

As for other the future directions of this project, we first note that the current model is not sufficient to reproduce experimental results, regardless of the applicability of exact quantum methods. There currently does not exist a mechanism in this model by which the NO molecule can dissipate vibrational energy into the metal surface; i.e. the current model is that of an elastic collision. Therefore, one feasible avenue to make the model more sophisticated is to include a dissipative bath of oscillators close to the metal surface, one with a spectral density that mimics the band structure of the gold surface. Given that SC-IVR methods are exact for the harmonic oscillator, and given the success of AMQC-IVR (and likely MQC-IVR) in describing the dynamics of the system-bath models of Chapter 4, MQC-IVR-based methods may prove particularly useful in such a system.

7.2 Zero-Point Energy Leakage in MQC-IVR Methods

As mentioned in the introduction, zero-point energy leakage can be a significant problem when simulating vibrational motion with classical MD, or with classical limit SC-IVRs such as LSC-IVR [16]. Given that the classical limit of MQC-IVR-based methods, i.e. Husimi-IVR, is a similar methodology to that of LSC-IVR, and given that Bucholz et al. [83] have verified that the quantum limit

of MQC-IVR based-methods, i.e. DHK-IVR, does not exhibit zero-point energy leakage, it is worth examining the extent to which MQC-IVR and AMQC-IVR conserve zero-point energy when different dofs of a multidimensional system are quantized to different extents. In this section we summarize the ongoing work to address this problem.

7.2.1 The Model

We consider a 2D system of weakly coupled harmonic oscillators [83], the Hamiltonian of which is given by

$$H = \sum_{j=1}^{2} \left\{ \frac{1}{2} p_j^2 + \frac{1}{2} \omega_j^2 q_j^2 \right\} + c \left(q_1 - q_2 \right)^3 , \tag{7.18}$$

with $\omega_1 = 0.01$, $\omega_2 = 0.005$, and $c = 10^{-8}$. Each oscillator is initialized in its ground state, and operator $\hat{A}$ is taken to be a projector of the initial state,

$$\hat{A} = |0_1 0_2\rangle \langle 0_1 0_2| . \tag{7.19}$$

The extent of zero-point energy leakage associated with the j^{th} dof is quantified by,

$$\delta E_{jt} = 1 - \langle E_j \rangle_t / \langle E_j \rangle_0, \tag{7.20}$$

with energy expectation value $\langle E_j \rangle_t$ given by

$$\langle E_j \rangle_t = \frac{1}{2} \langle p_j^2 \rangle_t + \frac{1}{2} \omega_j \langle q_j^2 \rangle_t, \tag{7.21}$$

$\forall\ j \in [1, 2]$. When using MQC-IVR with tuning parameters $c_{jj} \leq 0.01$, initial conditions of the j^{th} dof are sampled from the following distribution,

$$\rho_1 \left(p_{0j}, q_{0j}, p'_{0j}, q'_{0j} \right) = \mathcal{N}_1 \left| \langle p_{0j} q_{0j} | 0_j \rangle \langle 0_j | p'_{0j} q'_{0j} \rangle \right| , \tag{7.22}$$

and when using tuning parameters $c_{jj} > 0.01$, initial conditions of the j^{th} dof are sampled from a correlated distribution of mean ($\bar{x} = \frac{1}{2}(x + x')$) and difference ($\Delta_x = x' - x$) variables,

$$\rho_2\left(p_{0j}, q_{0j}, p'_{0j}, q'_{0j}\right) = \mathcal{N}_2 \left|\langle \bar{p}_{0j}\bar{q}_{0j}|0_j\rangle\right| e^{-\frac{c_{jj}}{2}\Delta^2_{q_{0j}} - \frac{c_{jj}}{2}\Delta^2_{p_{0j}}}. \tag{7.23}$$

When using AMQC-IVR the initial conditions of the quantum dof are sampled from Eq. 7.22, and the initial conditions of the classical dof are sampled from the Husimi distribution of the ground state projector,

$$\rho_3\left(p_{0j}, q_{0j}\right) = \mathcal{N}_3 \left|\langle p_{0j}q_{0j}|0_j\rangle\right|^2. \tag{7.24}$$

The set of constants $\{\mathcal{N}_k\}\ \forall\ k \in [1,3]$ are for normalization. The coherent state matrix elements of $\hat{B} = \hat{x}^2$ and $\hat{B} = \hat{p}^2$ are given by

$$\langle p'_j q'_j|\hat{x}^2_j|p_j q_j\rangle = \frac{1}{2\gamma_j}\left[1 + \frac{1}{2\gamma_j}\mathcal{D}^2_{j+}\right]\langle p'_j q'_j|p_j q_j\rangle, \tag{7.25}$$

$$\langle p'_j q'_j|\hat{p}^2_j|p_j q_j\rangle = \frac{\gamma_j}{2}\left[1 - \frac{1}{2\gamma_j}\mathcal{D}^2_{j-}\right]\langle p'_j q'_j|p_j q_j\rangle, \tag{7.26}$$

with $\mathcal{D}_j = \gamma_j q_j + i p_j$ and $\mathcal{D}_{j\pm} = \mathcal{D}_j \pm \left(\mathcal{D}'_j\right)^*$. We also take $\gamma_j = \omega_j\ \forall\ j$.

7.2.2 Numerical Tests

Fig. 7.5 plots δE_{jt} for each oscillator as computed with MQC-IVR and AMQC-IVR, and with different combinations of quantized dofs. As expected of MQC-IVR with very small tuning parameters, we see in Fig. 7.5 that the energy of each mode does not drift over time. This agrees very well with the DHK-IVR results reported by Bucholz et al. [83] Also as expected, since Husimi-IVR is a similar level of SC theory to that of LSC-IVR, we see in Fig. 7.5 that the Husimi-IVR results drastically drift away from the true value over time. Furthermore,

since Husimi-IVR is the classical limit of MQC-IVR, we see that the MQC-IVR results with large tuning parameters in Fig. 7.5(a) agree well with the Husimi-IVR results for each mode.

The dashed curves in Fig. 7.5(b) and Fig. 7.5(c) correspond to the treatment of each oscillator in a different limit. In the former case the limit is determined numerically with very small and very large tuning parameters of MQC-IVR, and in the latter case we treat each oscillator in the extreme quantum or classical limit with AMQC-IVR. As expected, these methods yield similar results. The interesting feature of Fig. 7.5(b) and Fig. 7.5(c) is, however, that, in each of the four simulations, the energy of the quantized oscillator does not increasingly drift away from its true value. There is a slight deviation from the true value, which approaches a maximum around $t = 10000 - 12000$, but, in each case, the deviation approaches zero again at later times. Moreover, it also interesting to note that, in each of the four simulations, the oscillator that is treated in the classical limit exhibits energy drifting that is even more drastic than the drifting seen in the Husimi-IVR results.

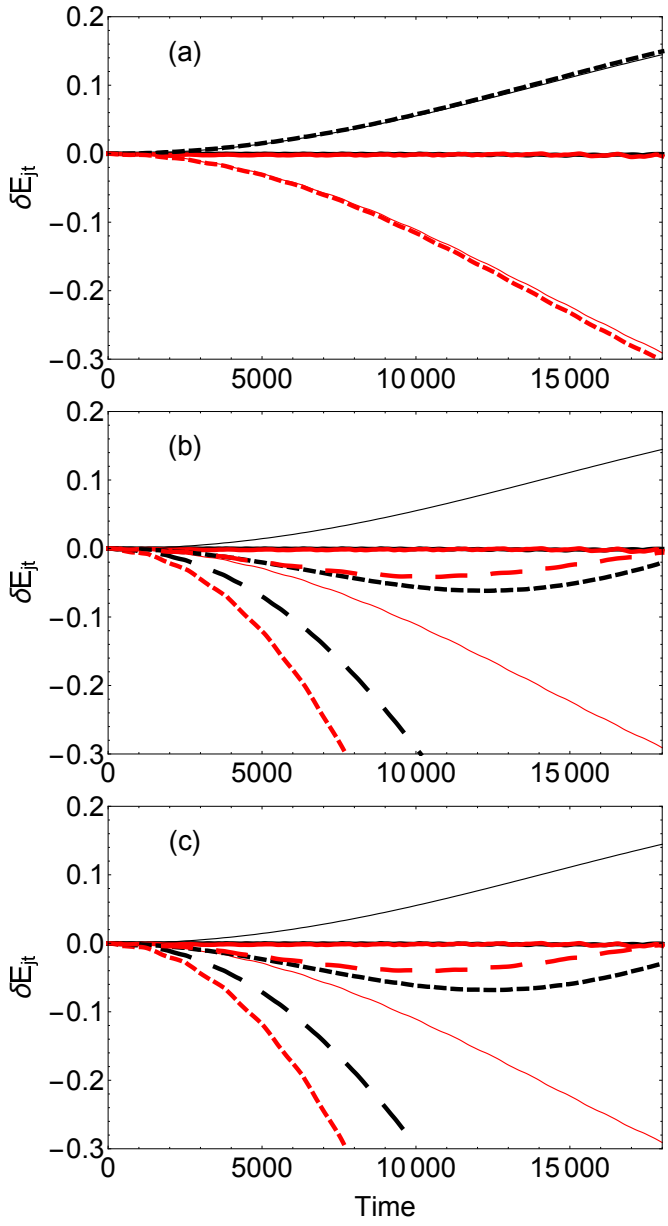

Figure 7.5: The extent of energy drift δE_{jt} as a function of time in the high frequency mode (black) and the low frequency mode (red). Each panel contains MQC-IVR results with small tuning parameters $c_{high} = c_{low} = 10^{-5}$ (solid, thick) and Husimi-IVR results (solid, thin). Panel (a) also contains MQC-IVR results with large tuning parameters $c_{high} = c_{low} = 10^{5}$ (dashed). Panel (b) also contains MQC-IVR results with a quantized low frequency mode $c_{low} = 10^{-5}$ and a classical high frequency mode $c_{high} = 10^{5}$ (long, dashed), as well as the reverse (short, dashed). Panel (c) contains the AMQC-IVR result after quantizing only low frequency mode (long, dashed), and after only quantizing the high frequency mode (short, dashed).

This analysis appears to suggest that quantized dofs in MQC-IVR and AMQC-IVR do not exhibit significant zero-point energy leakage, even when the quantized dof is coupled to a mode that is treated in the classical limit. However, there are several avenues of research to consider before this statement is fully verified. The slight deviations in energy associated with the quantized modes, as discussed in the previous paragraph, may be system-dependent. For example, a more strongly coupled system could potentially give rise to a less favorable result. It will also be worth considering longer time-scales in order to determine whether the energies of the quantized modes are either oscillating about the true value or, eventually, drifting away as they do in the classical limit.

As for other future considerations, in the case of MQC-IVR, it will be worth determining the domain of tuning parameters at which point the energy begins to drift unfavorably. Furthermore, a detailed convergence analysis should be conducted in order to determine whether or not AMQC-IVR is more computationally efficient than MQC-IVR with an optimal choice of tuning parameters.

7.3 General Conclusions

In this dissertation we have shown that MFF can be used on the DHK-IVR time-correlation function to derive some very powerful and efficient methodologies (namely MQC-IVR and AMQC-IVR) for the simulation of complex multidimensional chemical systems that exhibit strong nuclear quantum effects like zero-point energy and interference. Each of these methods offer mode-specific quantization in a dynamically uniform framework, and are readily extendable to nonadiabatic systems. Furthermore, given that these methods exploit the DF

implementation of propagating trajectory pairs, AMQC-IVR and MQC-IVR are perhaps the most computationally efficient avenues for computing the SC-IVR time-correlation function. We have also shown that these methods are most efficient when the classical subsystem is larger than the quantum subsystem, and when the coupling between quantum and classical subsystems is weak. Finally, we provided an overview of the SC Corr-Code Package, which offers a variety of approximations to the SC-IVR time-correlation function, including the new methodologies introduced in this dissertation. Now that these methods have proved to be accurate and efficient in describing the dynamics of a number of multidimensional model systems, they should prove very powerful in the study of a variety of true molecular systems in future work.

APPENDIX A

FB MQC-IVR PREFACTORS

A.1 Simplification of the FB MQC-IVR Prefactor

Here we simplify the FB MQC-IVR prefactor,

$$D_t^{FB}\left(\mathbf{p}_0,\mathbf{q}_0,\mathbf{p}_t',\mathbf{q}_t';\gamma_0,\gamma_t,\mathbf{c}_p,\mathbf{c}_q\right)=C_t\left(\mathbf{p}_0,\mathbf{q}_0,\mathbf{p}_t,\mathbf{q}_t;\gamma_0,\gamma_t\right)C_{-t}\left(\mathbf{p}_t',\mathbf{q}_t',\mathbf{p}_0',\mathbf{q}_0';\gamma_t,\gamma_0\right)\frac{\det\left[\mathbf{K}^{\mathrm{T}}+i\tilde{\mathbf{c}}^{\mathrm{T}}\mathbf{J}\right]^{\frac{1}{2}}}{\det\left[\mathbf{K}^{\mathrm{T}}\right]^{\frac{1}{2}}},\tag{A.1}$$

to an $N\times N$ determinant containing a combination of forward and backward monodromy matrix elements. We first show that the denominator on the right-hand side of Eq. A.1 is proportional to the product of forward and backward HK-IVR prefactors. We begin by considering the following determinant,

$$\det\left[\mathbf{K}^{\mathrm{T}}\right]=\det\begin{bmatrix}-\frac{1}{2}\left(\mathbf{M}_{pq}^{(b)}-i\gamma_0\mathbf{M}_{qq}^{(b)}\right) & -\frac{1}{2}\left(\mathbf{M}_{pp}^{(b)}-i\gamma_0\mathbf{M}_{qp}^{(b)}\right) & -\frac{i}{2}\gamma_0 & -\frac{1}{2}\mathbb{I}\\ \frac{1}{2}\left(\mathbf{M}_{qq}^{(b)}+i\gamma_0^{-1}\mathbf{M}_{pq}^{(b)}\right) & \frac{1}{2}\left(\mathbf{M}_{qp}^{(b)}+\gamma_0^{-1}i\mathbf{M}_{pp}^{(b)}\right) & \frac{1}{2}\mathbb{I} & -\frac{i}{2}\gamma_0^{-1}\\ \frac{i}{2}\gamma_t & \frac{1}{2}\mathbb{I} & \frac{1}{2}\left(\mathbf{M}_{pq}^{(f)}-i\gamma_t\mathbf{M}_{qq}^{(f)}\right) & \frac{1}{2}\left(\mathbf{M}_{pp}^{(f)}-i\gamma_t\mathbf{M}_{qp}^{(f)}\right)\\ -\frac{1}{2}\mathbb{I} & \frac{i}{2}\gamma_t^{-1} & -\frac{1}{2}\left(\mathbf{M}_{qq}^{(f)}+i\gamma_t^{-1}\mathbf{M}_{pq}^{(f)}\right) & -\frac{1}{2}\left(\mathbf{M}_{qp}^{(f)}+i\gamma_t^{-1}\mathbf{M}_{pp}^{(f)}\right)\end{bmatrix},\tag{A.2}$$

and proceed by adding a multiple of the second row ($i\gamma_0$ from the left) to the first row, add a multiple of the resulting first row ($\frac{i}{2}\gamma_0^{-1}$ from the left) to the second row, then add a multiple of the fourth row ($i\gamma_t$ from the left) to the third row, and, finally, permute rows 2-3-4 to the order 4-2-3 to obtain

$$\det\left[\mathbf{K}^{\mathrm{T}}\right]=\det\begin{bmatrix}-\mathbf{M}_{pq}^{(b)}+i\gamma_0\mathbf{M}_{qq}^{(b)} & -\mathbf{M}_{pp}^{(b)}+i\gamma_0\mathbf{M}_{qp}^{(b)} & \mathbb{O} & \mathbb{O}\\ -\frac{1}{2}\mathbb{I} & \frac{i}{2}\gamma_t^{-1} & -\frac{1}{2}\left(\mathbf{M}_{qq}^{(f)}+i\gamma_t^{-1}\mathbf{M}_{pq}^{(f)}\right) & -\frac{1}{2}\left(\mathbf{M}_{qp}^{(f)}+i\gamma_t^{-1}\mathbf{M}_{pp}^{(f)}\right)\\ \mathbb{O} & \mathbb{O} & \frac{1}{2}\mathbb{I} & -\frac{i}{2}\gamma_0^{-1}\\ \mathbb{O} & \mathbb{O} & \mathbf{M}_{pq}^{(f)}-i\gamma_t\mathbf{M}_{qq}^{(f)} & \mathbf{M}_{pp}^{(f)}-i\gamma_t\mathbf{M}_{qp}^{(f)}\end{bmatrix}.\tag{A.3}$$

We now make use of the following block matrix identity,

$$\det\begin{bmatrix}\mathbf{A} & \mathbf{B}\\ \mathbf{C} & \mathbf{D}\end{bmatrix}=\begin{cases}\det\left[\mathbf{AD}-\mathbf{BC}\right], & [\mathbf{C},\mathbf{D}]=0\\ \det\left[\mathbf{DA}-\mathbf{CB}\right], & [\mathbf{A},\mathbf{B}]=0.\end{cases}\tag{A.4}$$

The determinant of $\mathbf{K}^{\mathrm{T}}$ then reduces to

$$\begin{aligned}\det\left[\mathbf{K}^{\mathrm{T}}\right] &= \det\begin{bmatrix} -\mathbf{M}^{(b)}_{pq} + i\gamma_0\mathbf{M}^{(b)}_{qq} & -\mathbf{M}^{(b)}_{pp} + i\gamma_0\mathbf{M}^{(b)}_{qp} \\ -\frac{1}{2}\mathbb{I} & \frac{i}{2}\gamma_t^{-1} \end{bmatrix} \det\begin{bmatrix} \frac{1}{2}\mathbb{I} & -\frac{i}{2}\gamma_0^{-1} \\ \mathbf{M}^{(f)}_{pq} - i\gamma_t\mathbf{M}^{(f)}_{qq} & \mathbf{M}^{(f)}_{pp} - i\gamma_t\mathbf{M}^{(f)}_{qp} \end{bmatrix} \\ &= \det\left[-\mathbb{I}\right] C_t(\mathbf{p}_0, \mathbf{q}_0, \mathbf{p}_t, \mathbf{q}_t; \gamma_0, \gamma_t)^2 C_{-t}(\mathbf{p}'_t, \mathbf{q}'_t, \mathbf{p}'_0, \mathbf{q}'_0; \gamma_t, \gamma_0)^2. \end{aligned} \tag{A.5}$$

We therefore have

$$D_t^{FB}\left(\mathbf{p}_0, \mathbf{q}_0, \mathbf{p}'_t, \mathbf{q}'_t; \gamma_0, \gamma_t, \mathbf{c}_p, \mathbf{c}_q\right) = \det\left[-\mathbb{I}\right]^{\frac{1}{2}} \det\left[\mathbf{K}^{\mathrm{T}} + i\tilde{\mathbf{c}}^{\mathrm{T}}\mathbf{J}\right]^{\frac{1}{2}}. \tag{A.6}$$

Now we simplify the remaining determinant on the right-hand side of Eq. A.6. We have

$$\begin{aligned} &\det\left[\mathbf{K}^{\mathrm{T}} + i\tilde{\mathbf{c}}\mathbf{J}\right] \\ &= \det\begin{bmatrix} -\mathbf{M}^{(b)}_{pq} + i\gamma_0\mathbf{M}^{(b)}_{qq} & -\mathbf{M}^{(b)}_{pp} + i\gamma_0\mathbf{M}^{(b)}_{qp} & \mathbb{O} & \mathbb{O} \\ \mathbb{O} & \mathbb{O} & \frac{1}{2}\mathbb{I} & -\frac{i}{2}\gamma_0^{-1} \\ \frac{i}{2}\gamma_t + i\mathbf{c}_q & \frac{1}{2}\mathbb{I} & \frac{1}{2}\mathbf{M}^{(f)}_{pq} - (\frac{i}{2}\gamma_t + i\mathbf{c}_q)\mathbf{M}^{(f)}_{qq} & \frac{1}{2}\mathbf{M}^{(f)}_{pp} - (\frac{i}{2}\gamma_t + i\mathbf{c}_q)\mathbf{M}^{(f)}_{qp} \\ -\frac{1}{2}\mathbb{I} & \frac{i}{2}\gamma_t^{-1} + i\mathbf{c}_p & -\frac{1}{2}\mathbf{M}^{(f)}_{qq} - (\frac{i}{2}\gamma_t^{-1} + i\mathbf{c}_p)\mathbf{M}^{(f)}_{pq} & -\frac{1}{2}\mathbf{M}^{(f)}_{qp} - (\frac{i}{2}\gamma_t^{-1} + i\mathbf{c}_p)\mathbf{M}^{(f)}_{pp} \end{bmatrix} \\ &= \det\begin{bmatrix} \mathbf{X}\mathbf{M}^{(b)} & \mathbf{Y} \\ \mathbf{Z} & -\mathbf{Z}^{\mathrm{T}}\mathbf{M}^{(f)} \end{bmatrix} \\ &= \det\begin{bmatrix} \mathbf{Y} & \mathbf{X}\mathbf{M}^{(b)} \\ -\mathbf{Z}^{\mathrm{T}}\mathbf{M}^{(f)} & \mathbf{Z} \end{bmatrix} \end{aligned} \tag{A.7}$$

with

$$\mathbf{X} = \begin{pmatrix} i\gamma_0 & -\mathbb{I} \\ \mathbb{O} & \mathbb{O} \end{pmatrix}, \tag{A.8}$$

$$\mathbf{Y} = \begin{pmatrix} \mathbb{O} & \mathbb{O} \\ \frac{1}{2}\mathbb{I} & -\frac{i}{2}\gamma_0^{-1} \end{pmatrix}, \tag{A.9}$$

$$\mathbf{Z} = \begin{pmatrix} \frac{i}{2}\gamma_t + i\mathbf{c}_q & \frac{1}{2}\mathbb{I} \\ -\frac{1}{2}\mathbb{I} & \frac{i}{2}\gamma_t^{-1} + i\mathbf{c}_p \end{pmatrix}. \tag{A.10}$$

Note that the sign of the determinant is unchanged in Eq. A.7 after swapping columns since each block is of even dimensionality. We now use the following identity for the determinant of a general block matrix,

$$\det\begin{bmatrix}\mathbf{A} & \mathbf{B}\\ \mathbf{C} & \mathbf{D}\end{bmatrix} = \det[\mathbf{D}]\det\left[\mathbf{A}-\mathbf{B}\mathbf{D}^{-1}\mathbf{C}\right], \tag{A.11}$$

assuming $\mathbf{D}$ is invertible. Applying Eq. A.11 to Eq. A.7 gives

$$\det\left[\mathbf{K}^{\mathrm{T}} + i\tilde{\mathbf{c}}\mathbf{J}\right] = \det[\mathbf{Z}]\det\left[\mathbf{Y} + \mathbf{X}\mathbf{M}^{(b)}\mathbf{Z}^{-1}\mathbf{Z}^{\mathrm{T}}\mathbf{M}^{(f)}\right]. \tag{A.12}$$

Since $\mathbf{Z}$ is made of commuting diagonal blocks we can apply Eq. A.4 to obtain the following,

$$\begin{aligned}\det[\mathbf{Z}] &= \det\left[\left(\frac{i}{2}\gamma_t + i\mathbf{c}_q\right)\left(\frac{i}{2}\gamma_t^{-1} + i\mathbf{c}_p\right) + \frac{1}{4}\mathbb{I}\right]\\ &= \det\left[-\frac{1}{2}\left[\left(\mathbf{c}_q + \gamma_t\right)\mathbf{c}_p + \mathbf{c}_q\left(\gamma_t^{-1} + \mathbf{c}_p\right)\right]\right]\\ &= \det\left[-\frac{1}{2}\mathbf{G}\right].\end{aligned} \tag{A.13}$$

Consequently, the inverse of $\mathbf{Z}$ is given by

$$\mathbf{Z}^{-1} = \begin{pmatrix}-2\left(\frac{i}{2}\gamma_t^{-1} + i\mathbf{c}_p\right)\mathbf{G}^{-1} & \mathbf{G}^{-1}\\ -\mathbf{G}^{-1} & -2\left(\frac{i}{2}\gamma_t + i\mathbf{c}_q\right)\mathbf{G}^{-1}\end{pmatrix}. \tag{A.14}$$

Now we build up and simplify the matrix products within the right-most determinant on the right-hand side of Eq. A.12,

$$\mathbf{X}\mathbf{M}^{(b)} = \begin{pmatrix} -\mathbf{M}^{(b)}_{pq} + i\gamma_0\mathbf{M}^{(b)}_{qq} & -\mathbf{M}^{(b)}_{pp} + i\gamma_0\mathbf{M}^{(b)}_{qp} \\ \mathbb{O} & \mathbb{O} \end{pmatrix} \tag{A.15}$$

$$= \begin{pmatrix} \tilde{\mathbf{A}} & \tilde{\mathbf{B}} \\ \mathbb{O} & \mathbb{O} \end{pmatrix} \tag{A.16}$$

$$\mathbf{X}\mathbf{M}^{(b)}\mathbf{Z}^{-1} = \begin{pmatrix} -2\tilde{\mathbf{A}}\left(\frac{i}{2}\gamma_t^{-1} + i\mathbf{c}_p\right)\mathbf{G}^{-1} - \tilde{\mathbf{B}}\mathbf{G}^{-1} & \tilde{\mathbf{A}}\mathbf{G}^{-1} - 2\tilde{\mathbf{B}}\left(\frac{i}{2}\gamma_t + i\mathbf{c}_q\right)\mathbf{G}^{-1} \\ \mathbb{O} & \mathbb{O} \end{pmatrix}$$

$$= \begin{pmatrix} -2\tilde{\mathbf{A}}\mathbf{P}\mathbf{G}^{-1} - \tilde{\mathbf{B}}\mathbf{G}^{-1} & \tilde{\mathbf{A}}\mathbf{G}^{-1} - 2\tilde{\mathbf{B}}\mathbf{Q}\mathbf{G}^{-1} \\ \mathbb{O} & \mathbb{O} \end{pmatrix} \tag{A.17}$$

$$\mathbf{X}\mathbf{M}^{b}\mathbf{Z}^{-1}\mathbf{Z}^{\mathrm{T}} = \begin{pmatrix} \left(-2\tilde{\mathbf{A}}\mathbf{P}\mathbf{G}^{-1} - \tilde{\mathbf{B}}\mathbf{G}^{-1}\right)\mathbf{Q} + \frac{1}{2}\tilde{\mathbf{A}}\mathbf{G}^{-1} - \tilde{\mathbf{B}}\mathbf{Q}\mathbf{G}^{-1} & \tilde{\mathbf{A}}\mathbf{P}\mathbf{G}^{-1} + \frac{1}{2}\tilde{\mathbf{B}}\mathbf{G}^{-1} + \left(\tilde{\mathbf{A}}\mathbf{G}^{-1} - 2\tilde{\mathbf{B}}\mathbf{Q}\mathbf{G}^{-1}\right)\mathbf{P} \\ \mathbb{O} & \mathbb{O} \end{pmatrix}$$

$$= \begin{pmatrix} \tilde{\mathbf{R}} & \tilde{\mathbf{S}} \\ \mathbb{O} & \mathbb{O} \end{pmatrix}. \tag{A.18}$$

We now have

$$\det\left[\mathbf{Y} + \mathbf{X}\mathbf{M}^{(b)}\mathbf{Z}^{-1}\mathbf{Z}^{\mathrm{T}}\mathbf{M}^{(f)}\right] = \det\begin{bmatrix} \tilde{\mathbf{T}}_{11} & \tilde{\mathbf{T}}_{12} \\ \frac{1}{2}\mathbb{I} & -\frac{i}{2}\gamma_0^{-1} \end{bmatrix}$$

$$= \det\left[-\frac{1}{2}\left(i\tilde{\mathbf{T}}_{11}\gamma_0^{-1} + \tilde{\mathbf{T}}_{12}\right)\right], \tag{A.19}$$

where we have used Eq. A.4 and defined the following,

$$\tilde{\mathbf{T}}_{11} = \tilde{\mathbf{R}}\mathbf{M}^{(f)}_{qq} + \tilde{\mathbf{S}}\mathbf{M}^{(f)}_{pq} \tag{A.20}$$

$$\tilde{\mathbf{T}}_{12} = \tilde{\mathbf{R}}\mathbf{M}^{(f)}_{qp} + \tilde{\mathbf{S}}\mathbf{M}^{(f)}_{pp}. \tag{A.21}$$

After noting the commutators $\left[\mathbf{Q}, \mathbf{G}^{-1}\right] = \left[\mathbf{P}, \mathbf{G}^{-1}\right] = 0$, and after recognizing that $\mathbf{PQG}^{-1} = -\frac{1}{4}\mathbf{G}^{-1} - \frac{1}{2}\mathbb{I}$, we have

$$
\begin{aligned}
i\tilde{\mathbf{T}}_{11}\gamma_0^{-1} + \tilde{\mathbf{T}}_{12} = &\left[\tilde{\mathbf{A}}\left(\mathbf{G}^{-1} + \mathbb{I}\right) - 2\tilde{\mathbf{B}}\mathbf{G}^{-1}\mathbf{Q}\right]\left(\mathbf{M}_{qp}^{(f)} + i\mathbf{M}_{qq}^{(f)}\gamma_0^{-1}\right) \\
&+ \left[\tilde{\mathbf{B}}\left(\mathbf{G}^{-1} + \mathbb{I}\right) + 2\tilde{\mathbf{A}}\mathbf{G}^{-1}\mathbf{P}\right]\left(\mathbf{M}_{qq}^{(f)} + i\mathbf{M}_{pq}^{(f)}\gamma_0^{-1}\right) \\
&= \left(\gamma_0\mathbf{M}_{qq}^{(b)} + i\mathbf{M}_{pq}^{(b)}\right)\left(\mathbf{G}^{-1} + \mathbb{I}\right)\left(\mathbf{M}_{qq}^{(f)} - i\mathbf{M}_{qp}^{(f)}\gamma_0\right)\left(-\gamma_0^{-1}\right) \\
&+2\left(\mathbf{M}_{pp}^{(b)} - i\gamma_0\mathbf{M}_{qp}^{(b)}\right)\mathbf{G}^{-1}\left(\frac{1}{2}\gamma_t + \mathbf{c}_q\right)\left(\mathbf{M}_{qq}^{(f)} - i\mathbf{M}_{qp}^{(f)}\gamma_0\right)\left(-\gamma_0^{-1}\right) \\
&- \left(\mathbf{M}_{pp}^{(b)} - i\gamma_0\mathbf{M}_{qp}^{(b)}\right)\left(\mathbf{G}^{-1} + \mathbb{I}\right)\left(\mathbf{M}_{pp}^{(f)}\gamma_0 + i\mathbf{M}_{pq}^{(f)}\right)\left(\gamma_0^{-1}\right) \\
&-2\left(\gamma_0\mathbf{M}_{qq}^{(b)} + i\mathbf{M}_{pq}^{(b)}\right)\left(\frac{1}{2}\gamma_t^{-1} + \mathbf{c}_p\right)\mathbf{G}^{-1}\left(\mathbf{M}_{pp}^{(f)}\gamma_0 + i\mathbf{M}_{pq}^{(f)}\right)\left(\gamma_0^{-1}\right). \qquad \text{(A.22)}
\end{aligned}
$$

Substituting everything back into Eq. A.6 then gives our final expression for the FB MQC-IVR prefactor,

$$
\begin{aligned}
D_t^{FB}\left(\mathbf{p}_0, \mathbf{q}_0, \mathbf{p}_t', \mathbf{q}_t'; \gamma_0, \gamma_t, \mathbf{c}_p, \mathbf{c}_q\right) = &\det\left[\frac{1}{2}\gamma_0^{-1}\mathbf{G}\right]^{\frac{1}{2}} \\
\times \det\Bigg[&\frac{1}{2}\left(\gamma_0\mathbf{M}_{qq}^{(b)} + i\mathbf{M}_{pq}^{(b)}\right)\left(\mathbf{G}^{-1} + \mathbb{I}\right)\left(\mathbf{M}_{qq}^{(f)} - i\mathbf{M}_{qp}^{(f)}\gamma_0\right) \\
&+ \left(\mathbf{M}_{pp}^{(b)} - i\gamma_0\mathbf{M}_{qp}^{(b)}\right)\left(\frac{1}{2}\gamma_t + \mathbf{c}_q\right)\mathbf{G}^{-1}\left(\mathbf{M}_{qq}^{(f)} - i\mathbf{M}_{qp}^{(f)}\gamma_0\right) \\
&+ \left(\gamma_0\mathbf{M}_{qq}^{(b)} + i\mathbf{M}_{pq}^{(b)}\right)\left(\frac{1}{2}\gamma_t^{-1} + \mathbf{c}_p\right)\mathbf{G}^{-1}\left(\mathbf{M}_{pp}^{(f)}\gamma_0 + i\mathbf{M}_{pq}^{(f)}\right) \\
&+ \frac{1}{2}\left(\mathbf{M}_{pp}^{(b)} - i\gamma_0\mathbf{M}_{qp}^{(b)}\right)\left(\mathbf{G}^{-1} + \mathbb{I}\right)\left(\mathbf{M}_{pp}^{(f)}\gamma_0 + i\mathbf{M}_{pq}^{(f)}\right)\Bigg]^{\frac{1}{2}}. \qquad \text{(A.23)}
\end{aligned}
$$

A.2 FB MQC-IVR with Reduced Dimensionality

Antipov et al. [78] have shown that the dimensionality of the FB MQC-IVR integral can be reduced from $4N$ to $3N$ without significant loss of accuracy if operator $\hat{B}$ is strictly a function of the position operator or strictly a function of the momentum operator. If operator $\hat{B}$ is a function of the position operator,

evaluating the limit in which $\gamma_t \to \infty$ results in collapsing the coherent states at time t to position states. To show this, take the γ_t dependence of the FB MQC-IVR integrand and insert identity in the form of a complete set of position states,

$$\begin{aligned} D_t^{FB} \langle \mathbf{p}_t' \mathbf{q}_t' | \hat{B}(\hat{\mathbf{x}}) | \mathbf{p}_t \mathbf{q}_t \rangle =& D_t^{FB} \int d\bar{\mathbf{x}} \langle \mathbf{p}_t' \mathbf{q}_t' | \bar{\mathbf{x}} \rangle B(\bar{\mathbf{x}}) \langle \bar{\mathbf{x}} | \mathbf{p}_t \mathbf{q}_t \rangle \\ =& D_t^{FB} \left(\frac{\det[\gamma_t]}{\pi^N} \right)^{\frac{1}{2}} \int d\bar{\mathbf{x}} e^{-\frac{1}{2}(\bar{\mathbf{x}}-\mathbf{q}_t')^{\mathrm{T}} \gamma_t (\bar{\mathbf{x}}-\mathbf{q}_t') - i\mathbf{p}_t'(\bar{\mathbf{x}}-\mathbf{q}_t')} B(\bar{\mathbf{x}}) e^{-\frac{1}{2}(\bar{\mathbf{x}}-\mathbf{q}_t)^{\mathrm{T}} \gamma_t (\bar{\mathbf{x}}-\mathbf{q}_t) + i\mathbf{p}_t(\bar{\mathbf{x}}-\mathbf{q}_t)}. \end{aligned} \tag{A.24}$$

We now use an identity of the δ-function,

$$\delta(x) = \lim_{\alpha \to \infty} \left(\frac{\alpha}{2\pi} \right)^{\frac{1}{2}} e^{-\frac{\alpha}{2}x^2}, \tag{A.25}$$

to evaluate Eq. A.24 in the limit that $\gamma_t \to \infty$,

$$\begin{aligned} \lim_{\gamma_t \to \infty} D_t^{FB} \langle \mathbf{p}_t' \mathbf{q}_t' | \hat{B}(\hat{\mathbf{x}}) | \mathbf{p}_t \mathbf{q}_t \rangle =& 2^N \pi^{\frac{N}{2}} \left[\lim_{\gamma_t \to \infty} \frac{D_t^{FB}}{\det[\gamma_t]^{\frac{1}{2}}} \right] \int d\bar{\mathbf{x}} \delta(\bar{\mathbf{x}} - \mathbf{q}_t') \delta(\bar{\mathbf{x}} - \mathbf{q}_t) e^{-i\mathbf{p}_t'(\bar{\mathbf{x}}-\mathbf{q}_t') + i\mathbf{p}_t(\bar{\mathbf{x}}-\mathbf{q}_t)} B(\bar{\mathbf{x}}) \\ =& 2^N \pi^{\frac{N}{2}} \left[\lim_{\gamma_t \to \infty} \frac{D_t^{FB}}{\det[\gamma_t]^{\frac{1}{2}}} \right] \delta(\mathbf{q}_t' - \mathbf{q}_t) e^{i\mathbf{p}_t(\mathbf{q}_t'-\mathbf{q}_t)} B(\mathbf{q}_t') \\ =& 2^N \pi^{\frac{N}{2}} \bar{D}_t^{FB} \delta(\mathbf{q}_t' - \mathbf{q}_t) e^{i\mathbf{p}_t(\mathbf{q}_t'-\mathbf{q}_t)} B(\mathbf{q}_t'). \end{aligned} \tag{A.26}$$

We now have

$$\begin{aligned} \bar{D}_t^{FB} =& \lim_{\gamma_t \to \infty} \frac{D_t^{FB}}{\det[\gamma_t]^{\frac{1}{2}}} \\ =& \lim_{\gamma_t \to \infty} \det\left[\frac{1}{2} \gamma_0^{-1} \mathbf{G} \gamma_t^{-1} \right]^{\frac{1}{2}} \\ & \times \det\left[\frac{1}{2} \left(\gamma_0 \mathbf{M}_{qq}^{(b)} + i\mathbf{M}_{pq}^{(b)} \right) \left(\mathbf{G}^{-1} + \mathbb{I} \right) \left(\mathbf{M}_{qq}^{(f)} - i\mathbf{M}_{qp}^{(f)} \gamma_0 \right) \right. \\ & + \left(\mathbf{M}_{pp}^{(b)} - i\gamma_0 \mathbf{M}_{qp}^{(b)} \right) \left(\frac{1}{2} \gamma_t + \mathbf{c}_q \right) \mathbf{G}^{-1} \left(\mathbf{M}_{qq}^{(f)} - i\mathbf{M}_{qp}^{(f)} \gamma_0 \right) \\ & + \left(\gamma_0 \mathbf{M}_{qq}^{(b)} + i\mathbf{M}_{pq}^{(b)} \right) \left(\frac{1}{2} \gamma_t^{-1} + \mathbf{c}_p \right) \mathbf{G}^{-1} \left(\mathbf{M}_{pp}^{(f)} \gamma_0 + i\mathbf{M}_{pq}^{(f)} \right) \\ & \left. + \frac{1}{2} \left(\mathbf{M}_{pp}^{(b)} - i\gamma_0 \mathbf{M}_{qp}^{(b)} \right) \left(\mathbf{G}^{-1} + \mathbb{I} \right) \left(\mathbf{M}_{pp}^{(f)} \gamma_0 + i\mathbf{M}_{pq}^{(f)} \right) \right]^{\frac{1}{2}}. \end{aligned} \tag{A.27}$$

Using the following identities,

$$\lim_{\gamma_t\to\infty} \mathbf{G}\boldsymbol{\gamma}_t^{-1}\mathbf{M}\mathbf{G}^{-1}\mathbf{M}' = \mathbb{O} \tag{A.28}$$

$$\lim_{\gamma_t\to\infty} \mathbf{G}\boldsymbol{\gamma}_t^{-1}\mathbf{M}\mathbf{M}' = \mathbf{c}_p\mathbf{M}\mathbf{M}' \tag{A.29}$$

$$\lim_{\gamma_t\to\infty} \mathbf{G}\boldsymbol{\gamma}_t^{-1}\mathbf{M}\boldsymbol{\gamma}_t\mathbf{G}^{-1}\mathbf{M}' = \mathbf{c}_p\mathbf{M}\mathbf{c}_p^{-1}\mathbf{M}' \tag{A.30}$$

$$\lim_{\gamma_t\to\infty} \mathbf{G}\boldsymbol{\gamma}_t^{-1}\mathbf{M}\mathbf{c}_q\mathbf{G}^{-1}\mathbf{M}' = \mathbb{O} \tag{A.31}$$

$$\lim_{\gamma_t\to\infty} \mathbf{G}\boldsymbol{\gamma}_t^{-1}\mathbf{M}\boldsymbol{\gamma}_t^{-1}\mathbf{G}^{-1}\mathbf{M}' = \mathbb{O} \tag{A.32}$$

$$\lim_{\gamma_t\to\infty} \mathbf{G}\boldsymbol{\gamma}_t^{-1}\mathbf{M}\mathbf{c}_p\mathbf{G}^{-1}\mathbf{M}' = \mathbb{O}, \tag{A.33}$$

where $\mathbf{M}$ and $\mathbf{M}'$ are arbitrary $N \times N$ complex matrices, the limit reduces to

$$\begin{aligned}\bar{D}_t^{FB} = \det\left[\frac{1}{4}\boldsymbol{\gamma}_0^{-1}\right]^{\frac{1}{2}} \det\Big[&\mathbf{c}_p\left(\boldsymbol{\gamma}_0\mathbf{M}_{qq}^{(b)} + i\mathbf{M}_{pq}^{(b)}\right)\left(\mathbf{M}_{qq}^{(f)} - i\mathbf{M}_{qp}^{(f)}\boldsymbol{\gamma}_0\right)\\ &+\mathbf{c}_p\left(\mathbf{M}_{pp}^{(b)} - i\boldsymbol{\gamma}_0\mathbf{M}_{qp}^{(b)}\right)\left(\mathbf{M}_{pp}^{(f)}\boldsymbol{\gamma}_0 + i\mathbf{M}_{pq}^{(f)}\right)\\ &+\mathbf{c}_p\left(\mathbf{M}_{pp}^{(b)} - i\boldsymbol{\gamma}_0\mathbf{M}_{qp}^{(b)}\right)\mathbf{c}_p^{-1}\left(\mathbf{M}_{qq}^{(f)} - i\mathbf{M}_{qp}^{(f)}\boldsymbol{\gamma}_0\right)\Big]^{\frac{1}{2}}.\end{aligned} \tag{A.34}$$

After substituting Eq. B.6 into Eq. A.26, then substituting Eq. A.26 into FB MQC-IVR and after evaluating the integral over $\mathbf{q}_t'$ we get FB MQC-IVR in the $\gamma_t \to \infty$ limit,

$$\begin{aligned}\bar{C}_{AB}^{FB}(t) = &\frac{1}{\left(2\pi^{\frac{3}{2}}\right)^N}\int d\mathbf{p}_0\int d\mathbf{q}_0\int d\mathbf{p}_t'\,\langle\mathbf{p}_0\mathbf{q}_0|\hat{A}|\mathbf{p}_0'\mathbf{q}_0'\rangle\, B(\mathbf{q}_t)\\ &\times\bar{D}_t^{FB}\left(\mathbf{p}_0,\mathbf{q}_0,\mathbf{p}_t';\boldsymbol{\gamma}_0,\mathbf{c}_p\right)e^{i\left[S_t(\mathbf{p}_0,\mathbf{q}_0)+S_{-t}(\mathbf{p}_t',\mathbf{q}_t)\right]}e^{-\frac{1}{2}\boldsymbol{\Delta}_{p_t}^{\mathrm{T}}\mathbf{c}_p\boldsymbol{\Delta}_{p_t}}.\end{aligned} \tag{A.35}$$

The double phase space average of FB MQC-IVR is now reduced from $4N$ to $3N$ in Eq. A.35, potentially easing the computational demand; since the forward and backward trajectories now share their final and initial coordinates, respectively, one would expect more phase cancellation as compared to Eq. 2.18.

A similar result can be derive when $\hat{B}$ is strictly a function of the momentum operator, $\hat{\mathbf{p}}$. Begin by taking the γ_t-dependent terms of the integrand in Eq. 2.18

and insert a complete set of momentum states in the coherent state matrix element of operator $\hat{B}$,

$$\begin{aligned} D_t^{FB} \langle \mathbf{p}_t' \mathbf{q}_t' | B(\hat{\mathbf{p}}) | \mathbf{p}_t \mathbf{q}_t \rangle =& D_t^{FB} \int d\bar{\mathbf{p}} \langle \mathbf{p}_t' \mathbf{q}_t' | \bar{\mathbf{p}} \rangle B(\bar{\mathbf{p}}) \langle \bar{\mathbf{p}} | \mathbf{p}_t \mathbf{q}_t \rangle \\ =& D_t^{FB} \left(\frac{\det[\gamma_t]^{-1}}{\pi^N} \right)^{\frac{1}{2}} \int d\bar{\mathbf{p}} e^{-\frac{1}{2}(\bar{\mathbf{p}}-\mathbf{p}_t')^{\mathrm{T}} \gamma_t^{-1} (\bar{\mathbf{p}}-\mathbf{p}_t') + i\mathbf{p}_t'\mathbf{q}_t'} B(\bar{\mathbf{p}}) e^{-\frac{1}{2}(\bar{\mathbf{p}}-\mathbf{p}_t)\gamma_t^{-1}(\bar{\mathbf{p}}-\mathbf{p}_t) - i\mathbf{p}_t\mathbf{q}_t}. \end{aligned} \tag{A.36}$$

Then use Eq. 4.3 to evaluate Eq. A.36 in the limit that $\gamma_t \to 0$,

$$\begin{aligned} \lim_{\gamma_t \to 0} D_t^{FB} \langle \mathbf{p}_t' \mathbf{q}_t' | \hat{B}(\hat{\mathbf{x}}) | \mathbf{p}_t \mathbf{q}_t \rangle =& 2^N \pi^{\frac{N}{2}} \left[\lim_{\gamma_t \to 0} \frac{D_t^{FB}}{\det[\gamma_t]^{-\frac{1}{2}}} \right] \int d\bar{\mathbf{p}} \delta(\bar{\mathbf{p}} - \mathbf{p}_t') \delta(\bar{\mathbf{p}} - \mathbf{p}_t) e^{i\mathbf{p}_t'\mathbf{q}_t' - i\mathbf{p}_t\mathbf{q}_t} B(\bar{\mathbf{p}}) \\ =& 2^N \pi^{\frac{N}{2}} \left[\lim_{\gamma_t \to \infty} \frac{D_t^{FB}}{\det[\gamma_t]^{-\frac{1}{2}}} \right] \delta(\mathbf{p}_t' - \mathbf{p}_t) e^{i\mathbf{p}_t'\mathbf{q}_t' - i\mathbf{p}_t\mathbf{q}_t} B(\mathbf{p}_t') \\ =& 2^N \pi^{\frac{N}{2}} \tilde{D}_t^{FB} \delta(\mathbf{p}_t' - \mathbf{p}_t) e^{i\mathbf{p}_t'\mathbf{q}_t' - i\mathbf{p}_t\mathbf{q}_t} B(\mathbf{q}_t'). \end{aligned} \tag{A.37}$$

The limit of the remaining prefactor is given by,

$$\begin{aligned} \tilde{D}_t^{FB} &= \lim_{\gamma_t \to 0} D_t^{FB} \det[\gamma_t]^{\frac{1}{2}} \\ &= \lim_{\gamma_t \to 0} \det\left[\frac{1}{2} \gamma_0^{-1} \mathbf{G} \gamma_t \right]^{\frac{1}{2}} \\ &\quad \times \det\left[\frac{1}{2} \left(\gamma_0 \mathbf{M}_{qq}^{(b)} + i\mathbf{M}_{pq}^{(b)} \right) \left(\mathbf{G}^{-1} + \mathbb{I} \right) \left(\mathbf{M}_{qq}^{(f)} - i\mathbf{M}_{qp}^{(f)} \gamma_0 \right) \right. \\ &\quad + \left(\mathbf{M}_{pp}^{(b)} - i\gamma_0 \mathbf{M}_{qp}^{(b)} \right) \left(\frac{1}{2} \gamma_t + \mathbf{c}_q \right) \mathbf{G}^{-1} \left(\mathbf{M}_{qq}^{(f)} - i\mathbf{M}_{qp}^{(f)} \gamma_0 \right) \\ &\quad + \left(\gamma_0 \mathbf{M}_{qq}^{(b)} + i\mathbf{M}_{pq}^{(b)} \right) \left(\frac{1}{2} \gamma_t^{-1} + \mathbf{c}_p \right) \mathbf{G}^{-1} \left(\mathbf{M}_{pp}^{(f)} \gamma_0 + i\mathbf{M}_{pq}^{(f)} \right) \\ &\quad \left. + \frac{1}{2} \left(\mathbf{M}_{pp}^{(b)} - i\gamma_0 \mathbf{M}_{qp}^{(b)} \right) \left(\mathbf{G}^{-1} + \mathbb{I} \right) \left(\mathbf{M}_{pp}^{(f)} \gamma_0 + i\mathbf{M}_{pq}^{(f)} \right) \right]^{\frac{1}{2}}. \end{aligned} \tag{A.38}$$

Using the following identities,

$$\lim_{\gamma_t \to 0} \mathbf{G}\boldsymbol{\gamma}_t \mathbf{M}\mathbf{G}^{-1}\mathbf{M}' = \mathbb{O} \tag{A.39}$$

$$\lim_{\gamma_t \to 0} \mathbf{G}\boldsymbol{\gamma}_t \mathbf{M}\mathbf{M}' = \mathbf{c}_q \mathbf{M}\mathbf{M}' \tag{A.40}$$

$$\lim_{\gamma_t \to 0} \mathbf{G}\boldsymbol{\gamma}_t \mathbf{M}\boldsymbol{\gamma}_t^{-1}\mathbf{G}^{-1}\mathbf{M}' = \mathbf{c}_q \mathbf{M}\mathbf{c}_q^{-1}\mathbf{M}' \tag{A.41}$$

$$\lim_{\gamma_t \to 0} \mathbf{G}\boldsymbol{\gamma}_t \mathbf{M}\mathbf{c}_q\mathbf{G}^{-1}\mathbf{M}' = \mathbb{O} \tag{A.42}$$

$$\lim_{\gamma_t \to 0} \mathbf{G}\boldsymbol{\gamma}_t \mathbf{M}\boldsymbol{\gamma}_t\mathbf{G}^{-1}\mathbf{M}' = \mathbb{O} \tag{A.43}$$

$$\lim_{\gamma_t \to 0} \mathbf{G}\boldsymbol{\gamma}_t \mathbf{M}\mathbf{c}_p\mathbf{G}^{-1}\mathbf{M}' = \mathbb{O}, \tag{A.44}$$

the limit reduces to

$$\begin{aligned}\tilde{D}_t^{FB} = \det\left[\frac{1}{4}\gamma_0^{-1}\right]^{\frac{1}{2}} \det\Big[&\mathbf{c}_q\left(\gamma_0\mathbf{M}_{qq}^{(b)} + i\mathbf{M}_{pq}^{(b)}\right)\left(\mathbf{M}_{qq}^{(f)} - i\mathbf{M}_{qp}^{(f)}\gamma_0\right)\\ &+\mathbf{c}_q\left(\mathbf{M}_{pp}^{(b)} - i\gamma_0\mathbf{M}_{qp}^{(b)}\right)\left(\mathbf{M}_{pp}^{(f)}\gamma_0 + i\mathbf{M}_{pq}^{(f)}\right)\\ &+\mathbf{c}_q\left(\gamma_0\mathbf{M}_{qq}^{(b)} + i\mathbf{M}_{pq}^{(b)}\right)\mathbf{c}_q^{-1}\left(\mathbf{M}_{pp}^{(f)}\gamma_0 + i\mathbf{M}_{pq}^{(f)}\right)\Big]^{\frac{1}{2}}.\end{aligned} \tag{A.45}$$

After substituting Eq. A.45 into Eq. A.37, substituting Eq. A.37 into FB MQC-IVR, and after evaluating the integral over $\mathbf{p}_t'$ we have

$$\begin{aligned}\tilde{C}_{AB}^{FB}(t) =& \frac{1}{\left(2\pi^{\frac{3}{2}}\right)^N}\int d\mathbf{p}_0 \int d\mathbf{q}_0 \int d\mathbf{q}_t' \,\langle \mathbf{p}_0\mathbf{q}_0|\hat{A}|\mathbf{p}_0'\mathbf{q}_0'\rangle\, B\left(\mathbf{p}_t\right)\\ &\times e^{i\mathbf{p}_t\boldsymbol{\Delta}_{q_t}}\tilde{D}_t^{FB}\left(\mathbf{p}_0, \mathbf{q}_0, \mathbf{q}_t'; \gamma_0, \mathbf{c}_q\right) e^{i\left[S_t(\mathbf{p}_0,\mathbf{q}_0)+S_{-t}(\mathbf{p}_t,\mathbf{q}_t')\right]} e^{-\frac{1}{2}\boldsymbol{\Delta}_{q_t}^{\mathrm{T}}\mathbf{c}_q\boldsymbol{\Delta}_{q_t}},\end{aligned} \tag{A.46}$$

which, like Eq. A.35, involves more phase cancellation than FB MQC-IVR and a phase space integral of smaller dimensionality.

APPENDIX B

SIMPLIFICATION OF THE MQC-IVR PREFACTOR

Here we simplify the MQC-IVR prefactor,

$$D_t^{DF}\left(\mathbf{p}_0,\mathbf{q}_0,\mathbf{p}_0',\mathbf{q}_0';\gamma_0,\gamma_t,\mathbf{c}_p,\mathbf{c}_q\right) = C_t\left(\mathbf{p}_0,\mathbf{q}_0,\mathbf{p}_t,\mathbf{q}_t;\gamma_0,\gamma_t\right) C_t^*\left(\mathbf{p}_0',\mathbf{q}_0',\mathbf{p}_t',\mathbf{q}_t';\gamma_0,\gamma_t\right) \times \frac{\det\left[\mathbf{K}^{\mathrm{T}}+i\tilde{\mathbf{c}}^{\mathrm{T}}\mathbf{J}\right]^{\frac{1}{2}}}{\det\left[\mathbf{K}^{\mathrm{T}}\right]^{\frac{1}{2}}}, \tag{B.1}$$

to an $N\times N$ determinant containing a combination of forward and backward monodromy matrix elements. We first show that the denominator on the right-hand side of Eq. B.1 is proportional to the product of HK prefactors. We begin with

$$\det\left[\mathbf{K}^{\mathrm{T}}\right] = \det\begin{bmatrix} \frac{i}{2}\gamma_0 & -\frac{1}{2}\mathbb{I} & -\frac{i}{2}\gamma_0 & -\frac{1}{2}\mathbb{I} \\ \frac{1}{2}\mathbb{I} & \frac{i}{2}\gamma_0^{-1} & \frac{1}{2}\mathbb{I} & -\frac{i}{2}\gamma_0^{-1} \\ \frac{1}{2}\left(\mathbf{M}_{pq}'+i\gamma_t\mathbf{M}_{qq}'\right) & \frac{1}{2}\left(\mathbf{M}_{pp}'+i\gamma_t\mathbf{M}_{qp}'\right) & \frac{1}{2}\left(\mathbf{M}_{pq}-i\gamma_t\mathbf{M}_{qq}\right) & \frac{1}{2}\left(\mathbf{M}_{pp}-i\gamma_t\mathbf{M}_{qp}\right) \\ -\frac{1}{2}\left(\mathbf{M}_{qq}'-i\gamma_t^{-1}\mathbf{M}_{pq}'\right) & -\frac{1}{2}\left(\mathbf{M}_{qp}'-i\gamma_t^{-1}\mathbf{M}_{pp}'\right) & -\frac{1}{2}\left(\mathbf{M}_{qq}+i\gamma_t^{-1}\mathbf{M}_{pq}\right) & -\frac{1}{2}\left(\mathbf{M}_{qp}+i\gamma_t^{-1}\mathbf{M}_{pp}\right) \end{bmatrix}. \tag{B.2}$$

Now we add a multiple of the second row ($i\gamma_0$) to the first row, add a multiple of the third row ($i\gamma_t^{-1}$ from the left) to the fourth, then permute rows $2-3-4$ to the order $4-2-3$ to get

$$\det\left[\mathbf{K}^{\mathrm{T}}\right] = \det\begin{vmatrix} i\gamma_0 & -\mathbb{I} & \mathbb{O} & \mathbb{O} \\ -\left(\mathbf{M}_{qq}'-i\gamma_t^{-1}\mathbf{M}_{pq}'\right) & -\left(\mathbf{M}_{qp}'-i\gamma_t^{-1}\mathbf{M}_{pp}'\right) & \mathbb{O} & \mathbb{O} \\ \frac{1}{2}\mathbb{I} & \frac{i}{2}\gamma_0^{-1} & \frac{1}{2}\mathbb{I} & -\frac{i}{2}\gamma_0^{-1} \\ \frac{1}{2}\left(\mathbf{M}_{pq}'+i\gamma_t\mathbf{M}_{qq}'\right) & \frac{1}{2}\left(\mathbf{M}_{pp}'+i\gamma_t\mathbf{M}_{qp}'\right) & \frac{1}{2}\left(\mathbf{M}_{pq}-i\gamma_t\mathbf{M}_{qq}\right) & \frac{1}{2}\left(\mathbf{M}_{pp}-i\gamma_t\mathbf{M}_{qp}\right) \end{vmatrix}. \tag{B.3}$$

After noting the following block matrix identity,

$$\det\begin{vmatrix} \mathbf{A} & \mathbb{O} \\ \mathbf{C} & \mathbf{D} \end{vmatrix} = \det\left[\mathbf{A}\right]\det\left[\mathbf{D}\right], \tag{B.4}$$

we have

$$\det\left[\mathbf{K}^{\mathrm{T}}\right] = \det\begin{vmatrix} i\gamma_0 & -\mathbb{I} \\ -\left(\mathbf{M}_{qq}'-i\gamma_t^{-1}\mathbf{M}_{pq}'\right) & -\left(\mathbf{M}_{qp}'-i\gamma_t^{-1}\mathbf{M}_{pp}'\right) \end{vmatrix} \det\begin{vmatrix} \frac{1}{2}\mathbb{I} & -\frac{i}{2}\gamma_0^{-1} \\ \frac{1}{2}\left(\mathbf{M}_{pq}-i\gamma_t\mathbf{M}_{qq}\right) & \frac{1}{2}\left(\mathbf{M}_{pp}-i\gamma_t\mathbf{M}_{qp}\right) \end{vmatrix}. \tag{B.5}$$

Using Eq. A.4 on each term on the right-hand side of Eq. B.5 gives

$$\begin{aligned}\det\left[\mathbf{K}^{\mathrm{T}}\right] &= \det\left[-i\mathbf{M}'_{qp}\gamma_0 - \gamma_t^{-1}\mathbf{M}'_{pp}\gamma_0 - \mathbf{M}'_{qq} + i\gamma_t^{-1}\mathbf{M}'_{pq}\right] \\ &\times \det\left[\frac{1}{4}\mathbf{M}_{pp} - \frac{i}{4}\gamma_t\mathbf{M}_{qp} + \frac{i}{4}\mathbf{M}_{pq}\gamma_0^{-1} + \frac{1}{4}\gamma_t\mathbf{M}_{qq}\gamma_0^{-1}\right] \\ &= \det\left[-\mathbb{I}\right] C_t^2(\mathbf{p}_0, \mathbf{q}_0, \mathbf{p}_t, \mathbf{q}_t; \gamma_0, \gamma_t) C_t^{*2}(\mathbf{p}'_0, \mathbf{q}'_0, \mathbf{p}'_t, \mathbf{q}'_t; \gamma_0, \gamma_t), \end{aligned} \tag{B.6}$$

resulting in the following,

$$D_t^{DF}\left(\mathbf{p}_0, \mathbf{q}_0, \mathbf{p}'_0, \mathbf{q}'_0; \gamma_0, \gamma_t, \mathbf{c}_p, \mathbf{c}_q\right) = \det\left[-\mathbb{I}\right]^{\frac{1}{2}} \det\left[\mathbf{K}^{\mathrm{T}} + i\tilde{\mathbf{c}}^{\mathrm{T}}\mathbf{J}\right]^{\frac{1}{2}}. \tag{B.7}$$

Now we proceed to simplify the remaining determinant on the right-hand side of Eq. B.24,

$$\det\left[\mathbf{K}^{\mathrm{T}} + i\tilde{\mathbf{c}}\mathbf{J}\right] = \det\begin{bmatrix} \frac{i}{2}\gamma_0 + i\mathbf{c}_q & -\frac{1}{2}\mathbb{I} & -\left(\frac{i}{2}\gamma_0 + i\mathbf{c}_q\right) & -\frac{1}{2}\mathbb{I} \\ \frac{1}{2}\mathbb{I} & \frac{i}{2}\gamma_0^{-1} + i\mathbf{c}_p & \frac{1}{2}\mathbb{I} & -\left(\frac{i}{2}\gamma_0^{-1} + i\mathbf{c}_p\right) \\ \frac{1}{2}\left(\mathbf{M}'_{pq} + i\gamma_t\mathbf{M}'_{qq}\right) & \frac{1}{2}\left(\mathbf{M}'_{pp} + i\gamma_t\mathbf{M}'_{qp}\right) & \frac{1}{2}\left(\mathbf{M}_{pq} - i\gamma_t\mathbf{M}_{qq}\right) & \frac{1}{2}\left(\mathbf{M}_{pp} - i\gamma_t\mathbf{M}_{qp}\right) \\ -\frac{1}{2}\left(\mathbf{M}'_{qq} - i\gamma_t^{-1}\mathbf{M}'_{pq}\right) & -\frac{1}{2}\left(\mathbf{M}'_{qp} - i\gamma_t^{-1}\mathbf{M}'_{pp}\right) & -\frac{1}{2}\left(\mathbf{M}_{qq} + i\gamma_t^{-1}\mathbf{M}_{pq}\right) & -\frac{1}{2}\left(\mathbf{M}_{qp} + i\gamma_t^{-1}\mathbf{M}_{pp}\right) \end{bmatrix}. \tag{B.8}$$

First add a multiple of the third row ($-i\gamma_t^{-1}$ from the left) to the fourth row, then add a multiple of the new fourth row ($-\frac{i}{2}\gamma_t$ from the left) to the third row and obtain

$$\begin{aligned}\det\left[\mathbf{K}^{\mathrm{T}} + i\tilde{\mathbf{c}}\mathbf{J}\right] &= \det\begin{bmatrix} \mathbf{Z} & -\mathbf{Z}^{\mathrm{T}} \\ \mathbf{X}\mathbf{M}' & \mathbf{Y}\mathbf{M} \end{bmatrix} \\ &= \det\begin{bmatrix} -\mathbf{Z}^{\mathrm{T}} & \mathbf{Z} \\ \mathbf{Y}\mathbf{M} & \mathbf{X}\mathbf{M}' \end{bmatrix}, \end{aligned} \tag{B.9}$$

with

$$\mathbf{X} = \begin{pmatrix} \frac{i}{2}\gamma_t & \frac{1}{2}\mathbb{I} \\ \mathbb{O} & \mathbb{O} \end{pmatrix}, \tag{B.10}$$

$$\mathbf{Y} = \begin{pmatrix} \mathbb{O} & \mathbb{O} \\ -\mathbb{I} & -i\gamma_t^{-1} \end{pmatrix}, \tag{B.11}$$

$$\mathbf{Z} = \begin{pmatrix} \frac{i}{2}\gamma_0 + i\mathbf{c}_q & -\frac{1}{2}\mathbb{I} \\ \frac{1}{2}\mathbb{I} & \frac{i}{2}\gamma_0^{-1} + i\mathbf{c}_p \end{pmatrix}. \tag{B.12}$$

We now use the following block matrix identity,

$$\det\begin{bmatrix}\mathbf{A} & \mathbf{B}\\ \mathbf{C} & \mathbf{D}\end{bmatrix} = \det[\mathbf{A}]\det\left[\mathbf{D}-\mathbf{C}\mathbf{A}^{-1}\mathbf{B}\right], \tag{B.13}$$

assuming $\mathbf{A}$ is invertible, so that Eq. B.9 becomes

$$\begin{aligned}\det\left[\mathbf{K}^{\mathrm{T}}+i\tilde{\mathbf{c}}\mathbf{J}\right] &= \det\left[-\mathbf{Z}^{\mathrm{T}}\right]\det\left[\mathbf{X}\mathbf{M}'+\mathbf{Y}\mathbf{M}\left(\mathbf{Z}^{\mathrm{T}}\right)^{-1}\mathbf{Z}\right]\\ &= \det[\mathbf{Z}]\det\left[\mathbf{X}+\mathbf{Y}\mathbf{M}\left(\mathbf{Z}^{\mathrm{T}}\right)^{-1}\mathbf{Z}\left(\mathbf{M}'\right)^{-1}\right].\end{aligned} \tag{B.14}$$

On the right-hand side of Eq. B.14 we have multiplied by unity in the form of $\det\left[(\mathbf{M}')^{-1}\right] = 1$, and removed the leading minus sign since $\mathbf{Z}$ is of even dimensionality. The blocks of matrix $\mathbf{Z}^{\mathrm{T}}$ are diagonal so the determinant and inverse of $\mathbf{Z}^{\mathrm{T}}$ are easily found,

$$\begin{aligned}\det[\mathbf{Z}] &= \det\left[-\frac{1}{2}\left\{\mathbf{c}_q\left(\gamma_0^{-1}+\mathbf{c}_p\right)+\left(\gamma_0+\mathbf{c}_q\right)\mathbf{c}_p\right\}\right]\\ &= \det\left[-\frac{1}{2}\mathbf{G}\right],\end{aligned} \tag{B.15}$$

$$\left(\mathbf{Z}^{\mathrm{T}}\right)^{-1} = \begin{pmatrix}-2\left(\frac{i}{2}\gamma_0^{-1}+i\mathbf{c}_p\right)\mathbf{G}^{-1} & \mathbf{G}^{-1}\\ -\mathbf{G}^{-1} & -2\left(\frac{i}{2}\gamma_0+i\mathbf{c}_q\right)\mathbf{G}^{-1}\end{pmatrix}. \tag{B.16}$$

Now expand the matrix products on the right-hand side of Eq. B.14,

$$\mathbf{Y}\mathbf{M} = \begin{pmatrix}\mathbb{O} & \mathbb{O}\\ -\mathbf{\Gamma} & -i\mathbf{\Xi}\end{pmatrix} \tag{B.17}$$

$$\left(\mathbf{Z}^{\mathrm{T}}\right)^{-1}\mathbf{Z} = \begin{pmatrix}\mathbf{G}^{-1}+\mathbb{I} & 2\mathbf{P}\mathbf{G}^{-1}\\ -2\mathbf{Q}\mathbf{G}^{-1} & \mathbf{G}^{-1}+\mathbb{I}\end{pmatrix} \tag{B.18}$$

$$\mathbf{Y}\mathbf{M}\left(\mathbf{Z}^{\mathrm{T}}\right)^{-1}\mathbf{Z} = \begin{pmatrix}\mathbb{O} & \mathbb{O}\\ -\mathbf{\Gamma}\left(\mathbf{G}^{-1}+\mathbb{I}\right)+2i\mathbf{\Xi}\mathbf{Q}\mathbf{G}^{-1} & -i\mathbf{\Xi}\left(\mathbf{G}^{-1}+\mathbb{I}\right)-2\mathbf{\Gamma}\mathbf{P}\mathbf{G}^{-1}\end{pmatrix}, \tag{B.19}$$

with $\mathbf{\Gamma} = \left(\mathbf{M}_{qq} + i\gamma_t^{-1}\mathbf{M}_{pq}\right)$, $\mathbf{\Xi} = \left(\gamma_t^{-1}\mathbf{M}_{pp} - i\mathbf{M}_{qp}\right)$, $\mathbf{Q} = \left(\frac{i}{2}\gamma_0 + i\mathbf{c}_q\right)$, and $\mathbf{P} = \left(\frac{i}{2}\gamma_0^{-1} + i\mathbf{c}_p\right)$. Using Eq. 2.27 we then have

$$\mathbf{YM}\left(\mathbf{Z}^{\mathrm{T}}\right)^{-1}\mathbf{ZM}^b = \begin{pmatrix} \mathbb{O} & \mathbb{O} \\ \mathbf{T}_{21} & \mathbf{T}_{22} \end{pmatrix}, \tag{B.20}$$

with

$$\mathbf{T}_{12} = \left[-\mathbf{\Gamma}\left(\mathbf{G}^{-1} + \mathbb{I}\right) + 2i\mathbf{\Xi}\mathbf{Q}\mathbf{G}^{-1}\right]\mathbf{M}_{qq}^{(b)} + \left[-i\mathbf{\Xi}\left(\mathbf{G} + \mathbb{I}\right) - 2\mathbf{\Gamma}\mathbf{P}\mathbf{G}^{-1}\right]\mathbf{M}_{pq}^{(b)}, \tag{B.21}$$

$$\mathbf{T}_{22} = \left[-\mathbf{\Gamma}\left(\mathbf{G}^{-1} + \mathbb{I}\right) + 2i\mathbf{\Xi}\mathbf{Q}\mathbf{G}^{-1}\right]\mathbf{M}_{qp}^{(b)} + \left[-i\mathbf{\Xi}\left(\mathbf{G} + \mathbb{I}\right) - 2\mathbf{\Gamma}\mathbf{P}\mathbf{G}^{-1}\right]\mathbf{M}_{pp}^{(b)}. \tag{B.22}$$

We now have

$$\begin{aligned} \det\left[\mathbf{K}^{\mathrm{T}} + i\tilde{\mathbf{c}}\mathbf{J}\right] &= \det\left[-\frac{1}{2}\mathbf{G}\right]\det\begin{bmatrix} \frac{i}{2}\gamma_t & \frac{1}{2}\mathbb{I} \\ \mathbf{T}_{21} & \mathbf{T}_{22} \end{bmatrix} \\ &= \det\left[-\frac{1}{2}\mathbf{G}\right]\det\left[\frac{i}{2}\mathbf{T}_{22}\gamma_t - \frac{1}{2}\mathbf{T}_{21}\right]. \end{aligned} \tag{B.23}$$

Substituting Eq. B.23 back into Eq. B.24 gives the final expression for the general MQC-IVR prefactor,

$$\begin{aligned} D_t^{DF}\left(\mathbf{p}_0, \mathbf{q}_0, \mathbf{p}_0', \mathbf{q}_0'; \gamma_0, \gamma_t, \mathbf{c}_p, \mathbf{c}_q\right) &= \det\left[\frac{1}{2}\mathbf{G}\gamma_t^{-1}\right]^{\frac{1}{2}} \\ &\times \det\left[\frac{1}{2}\left(\gamma_t\mathbf{M}_{qq} + i\mathbf{M}_{pq}\right)\left(\mathbf{G}^{-1} + \mathbb{I}\right)\left(\mathbf{M}_{qq}^{(b)} - i\mathbf{M}_{qp}^{(b)}\gamma_t\right)\right. \\ &\left(\mathbf{M}_{pp} - i\gamma_t\mathbf{M}_{qp}\right)\left(\frac{1}{2}\gamma_0 + \mathbf{c}_q\right)\mathbf{G}^{-1}\left(\mathbf{M}_{qq}^{(b)} - i\mathbf{M}_{qp}^{(b)}\gamma_t\right) \\ &\left(\gamma_t\mathbf{M}_{qq} + i\mathbf{M}_{pq}\right)\left(\frac{1}{2}\gamma_0^{-1} + \mathbf{c}_p\right)\mathbf{G}^{-1}\left(\mathbf{M}_{pp}^{(b)}\gamma_t + i\mathbf{M}_{pq}^{(b)}\right) \\ &\left.\frac{1}{2}\left(\mathbf{M}_{pp} - i\gamma_t\mathbf{M}_{qp}\right)\left(\mathbf{G}^{-1} + \mathbb{I}\right)\left(\mathbf{M}_{pp}^{(b)}\gamma_t + i\mathbf{M}_{pq}^{(b)}\right)\right]^{\frac{1}{2}}. \end{aligned} \tag{B.24}$$

APPENDIX C

NUMERICAL PARAMETERS FOR NO/AU SYSTEM

α_1	1.5847	$E_h \cdot a_0$
α_2	2.36982	$E_h \cdot a_0$
α_c	0.1837	E_h
β_1	0.684374	a_0^{-1}
β_2	1.07367	a_0^{-1}
β_c	0.23573	a_0^{-1}
γ_2	0.283317	a_0
γ_c	0.0858976	a_0^{-1}
δ_2	0.245288	E_h
δ_c	−0.00179693	E_h
ϵ_2	1.24999	a_0^{-1}
ζ_2	1.8897	$E_h \cdot a_0$
D_1	0.225005	E_h
D_2	0.188997	E_h
A_1	1.69337	a_0^{-1}
A_2	1.27003	a_0^{-1}
R_{e1}	2.17507	a_0
R_{e2}	2.40203	a_0
η_1	$1 - 3/6.5$	Dimensionless
η_2	$1 - 3.5/6.5$	Dimensionless

Table C.1: Numerical parameters for NO/Au system.

BIBLIOGRAPHY

[1] M. D. Newton and N. Sutin. Electron transfer reactions in condensed phases. *Ann. Rev. Phys. Chem.*, 35:437–480, 1984.

[2] S. Hammes-Schiffer and A. A. Stuchebrukhov. Theory of coupled electron and proton transfer reactions. *Chem. Rev.*, 110:6939–6960, 2010.

[3] M. H. V. Huynh and T. J. Meyer. Proton-coupled electron transfer. *Chem. Rev.*, 107:5004–5064, 2007.

[4] Y. R. Reese and D. G. Nocera. Proton-coupled electron transfer in biology: Results from synergistic studies in natural and model systems. *Annu. Rev. Biochem.*, 78:673–699, 2009.

[5] H. B. Gray and J. R. Winkler. Electron transfer in proteins. *Annu. Rev. Biochem.*, 65:537–561, 1996.

[6] M. Gratzel. Photoelectrochemical cells. *Nature*, 414:338, 2001.

[7] M. Gratzel. Dye-sensitized solar cells. *J. Photochem. Photobiol. C*, 4:145–153, 2003.

[8] K. Golibrzuch, N. Bartels, D. J. Auerbach, and A. M. Wodtke. The dynamics of molecular interactions and chemical reactions at metal surfaces: Testing the foundations of theory. *Annu. Rev. Phys. Chem.*, 66:399, 2015.

[9] N. S. Lewis and D. G. Nocera. Powering the planet: Chemical challenges in solar energy utilization. *Proc. Natl. Acad. Sci.*, 103(43):15729–15735, 2006.

[10] B. Kippelen and J-L Bredas. Organic photovoltaics. *Energy Environ. Sci.*, 2:251–261, 2009.

[11] Y. Tachibana, L. Vayssieres, and J. R. Durrant. Artificial photosynthesis for solar water-splitting. *Nat. Photon.*, 6:511–518, 2012.

[12] O. Kruse, J. Rupprecht, J. H. Mussgnug, G. C. Dismukes, and B. Hankamer. Photosynthesis: a blueprint for solar energy capture and biohydrogen production technologies. *Photochem. Photobiol. Sci.*, 4:957–969, 2005.

[13] D. Sen. The uncertainty relations in quantum mechanics. *Curr. Sci.*, 107(2):203, 2014.

[14] M. E. Tuckerman. *Statistical Mechanics: Theory and Molecular Simulation*. Oxford University Press, 2010.

[15] W. H. Miller. Quantum dynamics of complex molecular systems. *Proc. Natl. Acad. Sci.*, 102(19):6660–6664, 2005.

[16] S. Habershon and D. E. Manolopoulos. Zero point energy leakage in condensed phase dynamics: An assessment of quantum simulation methods for liquid water. *J. Chem. Phys.*, 131:244518, 2009.

[17] M. S. Child. *Semiclassical Mechanics with Molecular Applications*. Oxford University Press, 2014.

[18] E. Schrodinger. *Collected Papers on Wave Mechanics*. AMS Chelsea Publishing, 1982.

[19] G. Wentzel. Eine verallgemeinerung der quantenbedingungen fur die zwecke der wellenmechanik. *Z. Phys.*, 38:518, 1926.

[20] H. A. Kramers. Wellenmechanik und halbzahlige quantisierung. *Z. Phys.*, 39:828, 1926.

[21] L. Brillouin. Schrodinger's wave mechanics; a general solution method by successive approximation. *CR Acad. Sci., Paris*, 183:24–26, 1926.

[22] H. Jeffreys. On certain approximate solutions of linear differential equations of the second order. *Proc. London Math. Soc.*, 23:428, 1925.

[23] J. H. Van Vleck. The correspondence principle in the statistical interpretation of quantum mechanics. *Proc. Natl. Acad. Sci. U.S.A.*, 14:178, 1928.

[24] R. E. Langer. On the connection formulas and the solutions of the wave equation. *Phys. Rev.*, 51:669, 1937.

[25] L. D. Landau. A theory of energy transfer ii. *PHys. Z. Sowjet.*, 2:46, 1932.

[26] C. Zener. Non-adiabatic crossing of energy levels. *Proc. Roys. Soc. A*, 137:696, 1932.

[27] K. W. Ford and J. A. Wheeler. Semiclassical description of scattering. *Ann. Phys.*, 7:259–286, 1959.

[28] M. V. Berry and K. E. Mount. Semiclassical approximations in wave mechanics. *Rep. Prog. Phys.*, 35:315, 1972.

[29] P. Pechukas. Time-dependent semiclassical scattering theory. ii. atomic collisions. *Phys. Rev.*, 181(1):174–185, 1969.

[30] R. A. Marcus. Extension of the wkb method to wave functions and transition probability amplitudes (s-matrix) for inelastic or reactive collisions. *Chem. Phys. Lett.*, 7:525, 1970.

[31] M. C. Gutzwiller. Energy spectrum according to classical mechanics. *J. Math. Phys.*, 11:1791, 1970.

[32] M. C. Gutzwiller. *Chaos in Classical and Quantum Mechanics*. Springer-Verlag, 1990.

[33] W. H. Miller. Classical-limit quantum mechanics and the theory of molecular collisions. *Adv. Chem. Phys.*, 25:69, 1974.

[34] D. J. Tannor. *Introduction to Quantum Mechanics: A Time-Dependent Perspective*. University Science Books, 2007.

[35] E. J. Heller. Frozen gaussians: A very simple semiclassical approximation. *J. Chem. Phys.*, 75:2923, 1981.

[36] E. J. Heller. Celluar dynamics: A new semiclassical approach to time-dependent quantum mechanics. *J. Chem. Phys.*, 94:2723, 1991.

[37] M. F. Herman and E. Kluk. A semiclasical justification for the use of non-spreading wavepackets in dynamics calculations. *Chemical Physics*, 91:27, 1984.

[38] W. H. Miller. The semiclassical initial value representation: a potentially practical way for adding quantum effects to classical molecular dynamics simulations. *J. Phys. Chem. A*, 105:2942–2955, 2001.

[39] R. P. Feynman. Space-time approach to non-relativistic quantum mechanics. *Rev. Mod. Phys.*, 20:367, 1948.

[40] R. P. Feynman and A. R. Hibbs. *Quantum Mechanics and Path Integrals*. Dover, 1965.

[41] V. I. Arnold. *Mathematical Methods of Classical Mechanics*. Springer-Verlag, 1989.

[42] M. C. Gutzwiller. Phase-integral approximation in momentum space and the bound states of an atom. *J. Math. Phys.*, 8:1979, 1967.

[43] R. G. Littlejohn. The van vleck formula, maslov theory, and phase space geometry. *J. Stat. Phys.*, 68:7, 1992.

[44] W. H. Miller. Classical s matrix: Numerical application to inelastic collisions. *J. Chem. Phys.*, 53:3578, 1970.

[45] C. Venkataraman and W. H. Miller. Chemical reaction rates using the semiclassical van vleck initial value representation. *J. Chem. Phys.*, 126:094104, 2007.

[46] K. G. Kay. Integral expressions for the semiclassical timedependent propagator. *J. Chem. Phys.*, 100:4377–4392, 1994.

[47] F. Grossmann and A. L. Xavier Jr. From the coherent state path integral to a semiclassical initial value representation of the quantum mechanical propagator. *Phys. Lett. A*, 243:243–248, 1998.

[48] W. H. Miller. An alternate derivation of the herman-kluk (coherent state) semiclassical initial value representation of the time evolution operator. *Mol. Phys.*, 100(4):397–400, 2002.

[49] S. A. Deshpande and G. S. Ezra. On the derivation of the herman-kluk propagator. *J. Phys. A: Math. Gen.*, 39:5067–5078, 2006.

[50] R. J. Glauber. Coherent and incoherent states of the radiation field. *Phys. Rev.*, 131(6):2766, 1963.

[51] K. G. Kay. Numerical study of semiclassical initial value methods for dynamics. *J. Chem. Phys.*, 100:4432, 1994.

[52] K. G. Kay. Semiclassical propagation for multidimensional systems by an initial value method. *J. Chem. Phys.*, 100:2250, 1994.

[53] G. Stock and M. Thoss. Semiclassical description of nonadiabatic quantum dynamics. *Phys. Rev. Lett.*, 78:578, 1997.

[54] X. Sun and W. H. Miller. Semiclassical initial value representation for electronically nonadiabatic molecular dynamics. *J. Chem. Phys.*, 106:6346–6353, 1997.

[55] X. Sun and W. H. Miller. Semiclassical initial value representation for rotational degrees of freedom: The tunneling dynamics of hcl dimer. *J. Chem. Phys.*, 108:8870–8877, 1998.

[56] D. E. Skinner and W. H. Miller. Application of the forward-backward initial value representation to molecular energy transfer. *J. Chem. Phys.*, 111:10787, 1999.

[57] V. S. Batista, M. T. Zanni, B. J. Greenblatt, D. M. Neumark, and W. H. Miller. Femtosecond photoelectron spectroscopy of the i2- anion: A semiclassical molecular dynamics simulation method. *J. Chem. Phys.*, 110:3736, 1999.

[58] H. Wang, M. Thoss, and W. H. Miller. Forward–backward initial value representation for the calculation of thermal rate constants for reactions in complex molecular systems. *J. Chem. Phys.*, 112:47–55, 2000.

[59] E. A. Coronado, V. S. Batista, and W. H. Miller. Nonadiabatic photodissociation dynamics of icn in the a continuum: A semiclassical initial value representation study. *J. Chem. Phys.*, 112:5566–5575, 2000.

[60] V. Guallar, V. S. Batista, and W. H. Miller. Semiclassical molecular dynamics simulations of intramolecular proton transfer in photoexcited 2-(2'-hydroxyphenyl)-oxazole. *J. Chem. Phys.*, 113:9510, 2000.

[61] M. Thoss, W. H. Miller, and G. Stock. Semiclassical description of nonadiabatic quantum dynamics: Application to the s1-s2 conical intersection in pyrazine. *J. Chem. Phys.*, 112:10282, 2000.

[62] H. Wang, D. E. Manolopoulos, and W. H. Miller. Generalized filinov transformation of the semiclassical initial value representation. *J. Chem. Phys.*, 115(14):6317, 2001.

[63] H. Wang, M. Thoss, K. L. Sorge, R. Gelabert, X. Gimenez, and W. H. Miller. Semiclassical description of quantum coherence effects and their quenching: A forward-backward initial value representation study. *J. Chem. Phys.*, 114:2562, 2001.

[64] R. Gelavert, X. Gimenez, M. Thoss, H. Wang, and W. H. Miller. Semiclassical description of diffraction and its quenching by the forward–backward version of the initial value representation. *J. Chem. Phys.*, 114:2572–2579, 2001.

[65] M. Thoss, H. Wang, and W. H. Miller. Generalized forward–backward initial value representation for the calculation of correlation functions in complex systems. *J. Chem. Phys.*, 114:9220–9235, 2001.

[66] J. Ankerhold, M. Saltzer, and E. Pollak. A study of the semiclassical initial value representation at short times. *J. Chem. Phys.*, 116:5925, 2002.

[67] L. Torres, R. Gelabert, X. Gimenez, M. Moreno, and J. M. Lluch. Semiclassical initial value representation description of molecular structure problems: An elongated dihydrogen ruthenium complex. *J. Chem. Phys.*, 117:7094, 2002.

[68] A. L. Kaledin and W. H. Miller. Time averaging the semiclassical initial value representation for the calculation of vibrational energy levels. *J. Chem. Phys.*, 118:7174, 2003.

[69] A. L. Kaledin and W. H. Miller. Time averaging the semiclassical initial value representation for the calculation of vibrational energy levels. ii. application to h2co, nh3, ch4, ch2d2. *J. Chem. Phys.*, 119:3078, 2003.

[70] S. Zhang and E. Pollak. Optimization of the semiclassical initial value representation of the exact quantum-mechanical real time propagator. *J. Chem. Phys.*, 119:11058, 2003.

[71] E. Pollak and J. Shao. Systematic improvement of initial value representations of the semiclassical propagator. *J. Phys. Chem. A*, 107:7112–7117, 2003.

[72] S. Zhang and E. Pollak. A prefactor free semiclassical initial value series representation of the propagator. *J. Chem. Phys.*, 121:3384, 2004.

[73] C. Harabati, J. M. Rost, and F. Grossmann. Long-time and unitary properties of semiclassical initial value representations. *J. Chem. Phys.*, 120:26, 2004.

[74] Y. Wu and M. F. Herman. Nonadiabatic surface hopping herman-kluk

semiclassical initial value representation method revisited: applications to tully's three model systems. *J. Chem. Phys.*, 123:144106, 2005.

[75] N. Ananth, C. Venkataraman, and W. H. Miller. Semiclassical description of electronically nonadiabatic dynamics via the initial value representation. *J. Chem. Phys.*, 127:084114, 2007.

[76] C. Harabati and K. G. Kay. Semiclassical initial value calculations of the collinear helium atom. *J. Chem. Phys.*, 127:084104, 2007.

[77] J. M. Moix and E. Pollak. Semiclassical initial-value-representation study of helium scattering from cu(110). *Phys. Rev. A*, 79:062507, 2009.

[78] S. V. Antipov, Z. Ye, and N. Ananth. Dynamically consistent method for mixed quantum-classical simulations: A semiclassical approach. *J. Chem. Phys.*, 142:184102, 2015.

[79] M. Buchholz, F. Grossmann, and M. Ceotto. Mixed semiclassical initial value representation time-averaging propagator for spectroscopic calculations. *J. Chem. Phys.*, 144:094102, 2016.

[80] M. Buchholz, F. Grossmann, and M. Ceotto. Application of the mixed-time averaging semiclassical initial value representation method to complex molecular spectra. *J. Chem. Phys.*, 147:164110, 2017.

[81] M. S. Church, S. V. Antipov, and N. Ananth. Validating and implementing modified filinov phase filtration in semiclassical dynamics. *J. Chem. Phys.*, 146:234104, 2017.

[82] M. S. Church, T. J. H. Hele, G. S. Ezra, and N. Ananth. Nonadiabatic semiclassical dynamics in the mixed quantum-classical initial value representation. *J. Chem. Phys.*, 148:102326, 2018.

[83] M. Buchholz, E. Fallacara, F. Gottwald, M. Ceotto, F. Grossmann, and S. D. Ivanov. Herman-kluk propagator is free from zero-point energy leakage. *Chem. Phys.*, 515:231–235, 2018.

[84] M. Buchholz, F. Grossmann, and M. Ceotto. Simplified approach to the mixed time-averaging semiclassical initial value representation for the calculation of dense vibrational spectra. *J. Chem. Phys.*, 148:114107, 2018.

[85] N. Makri and K. Thompson. Semiclassical influence functionals for quantum systems in anharmonic environments. *Chem. Phys. Lett.*, 291:101–109, 1998.

[86] K. Thompson and N. Makri. Influence functionals with semiclassical propagators in combined forward-backward time. *J. Chem. Phys.*, 110:1343, 1999.

[87] K. Thompson and N. Makri. Rigorous forward-backward semiclassical formulation of many-body dynamics. *Phys. Rev. E*, 59(5):R4729, 1999.

[88] V. S. Filinov. Calculation of the feynman integrals by means of the monte carlo method. *Nuc. Phys. B*, 271:717–725, 1986.

[89] N. Makri and W. H. Miller. Monte carlo integration with oscillatory integrands: implications for feynman path integration in real time. *Chem. Phys. Lett.*, 139:10–14, 1987.

[90] H. Wang and M. Thoss. Semiclassical simulation of absorption spectra for a chromophore coupled to an anharmonic bath. *Chem. Phys.*, 304:121–131, 2004.

[91] N. T. Maitra. Semiclassical maps: A study of classically forbidden transitions, sub-h structure, and dynamical localization. *J. Chem. Phys.*, 112(2):531, 2000.

[92] M. L. Brewer, J. S. Hulme, and D. E. Manolopoulos. Semiclassical dynamics in up to 15 coupled vibrational degrees of freedom. *J. Chem. Phys.*, 106:4832, 1997.

[93] V. S. Batista and W. H. Miller. Semiclassical molecular dynamics simulations of ultrafast photodissociation dynamics associated with the chappuis band of ozone. *J. Chem. Phys.*, 108:498, 1998.

[94] I. R. Craig and D. E. Manolopoulos. Quantum statistics and classical mechanics: Real time correlation functions from ring polymer molecular dynamics. *J. Chem. Phys.*, 121(8):3368–3373, 2004.

[95] A. R. Menzeleev, N. Ananth, and T. F. Miller III. Direct simulation of electron transfer using ring polymer molecular dynamics: Comparison with semiclassical instanton theory and exact quantum methods. *J. Chem. Phys.*, 135:074106, 2011.

[96] S. Habershon, D. E. Manolopoulos, T. E. Markland, and T. F. Miller III. Ring-polymer molecular dynamics: Quantum effects in chemical dynamics from classical trajectories in an extended phase space. *Ann. Rev. Phys. Chem.*, 64(1):387–413, 2013.

[97] A. R. Menzeleev, F. Bell, and T. F. Miller III. Kinetically constrained ring-polymer molecular dynamics for non-adiabatic chemical reactions. *J. Chem. Phys.*, 140:064103, 2014.

[98] J. Cao and G. A. Voth. The formulation of quantum statistical mechanics based on the feynman path centroid density. ii. dynamical properties. *J. Chem. Phys.*, 100:5106, 1994.

[99] S. Jang and G. A. Voth. A derivation of centroid molecular dynamics and other approximate time evolution methods for path integral centroid variables. *J. Chem. Phys.*, 111:2371, 1999.

[100] H. Wang, X. Sun, and W. H. Miller. Semiclassical approximations for the calculation of thermal rate constants for chemical reactions in complex molecular systems. *J. Chem. Phys.*, 108:9726–9736, 1998.

[101] X. Sun, H. Wang, and W. H. Miller. Semiclassical theory of electronically nonadiabatic dynamics: results of a linearized approximation to the initial value representation. *J. Chem. Phys.*, 109:7064, 1998.

[102] J. Liu. Recent advances in the linearized semiclassical initial value representation/classical wigner model for the thermal correlation function. *Int. J. Quantum Chem.*, 115:657–670, 2015.

[103] Q. Shi and E. Geva. A relationship between semiclassical and centroid correlation functions. *J. Chem. Phys.*, 118:8173, 2003.

[104] M. K. Lee, P. Huo, and D. F. Coker. Semiclassical path integral dynamics: Photosynthetic energy transfer with realistic environment interactions. *Annu. Rev. Phys. Chem.*, 67:639, 2016.

[105] S. J. Cotton and W. H. Miller. Symmetrical windowing for quantum states in quasi-classical trajectory simulations. *J. Phys. Chem. A*, 117:7190, 2013.

[106] R. F. Loring. Mean-trajectory approximation for the electronic and vibrational-electronic nonlinear spectoscopy. *J. Chem. Phys.*, 146:144106, 2017.

[107] B. C. Kruger, N. Bartels, C. Bartels, A. Kandratsenka, J. C. Tully, and A. M. Wodtke. No vibrational energy transfer on a metal surface: Still a challenge to first-principles theory. *J. Phys. Chem. C*, 119:3268, 2015.

[108] T. Uzer and W. H. Miller. Theories of intramolecular vibrational energy transfer. *Phys. Rep.*, 199:73, 1991.

[109] W. Domcke and D. R. Yarkony. Role of conical intersections in molecular spectroscopy and photoinduced chemical dynamics. *Annu. Rev. Phys. Chem.*, 63:325–352, 2012.

[110] J. Caro and L. L. Salcedo. Impediments to mixing classical and quantum dynamics. *Phys. Rev. A*, 60(2):842, 1999.

[111] H. D. Meyer and W. H. Miller. A classical analog for electronic degrees of freedom in nonadiabatic collision processes. *J. Chem. Phys.*, 70:3214–3223, 1979.

[112] M. Thoss and G. Stock. Mapping approach to the semiclassical description of nonadiabatic quantum dynamics. *Phys. Rev. A*, 59(1):64, 1999.

[113] N. Ananth. *Quantum Dynamical Behaviour in Complex Systems - A Semiclassical Approach*. PhD thesis, UC, Berkeley, San Franscisco, CA, 2008.

[114] B. E. Guerin and M. F. Herman. A numerical test of different integral conditioning approximations for a semiclassical initial value representation for wavepacket propagation. *Chem. Phys. Lett.*, 286:361–368, 1998.

[115] M. F. Herman. Improving the accuracy of semiclassical wavepacket propagation using integral conditioning techniques. *Chem. Phys. Lett.*, 275:445–452, 1997.

[116] A. R. Walton and D. E. Manolopoulos. A new semiclassical initial value method for franck-condon spectra. *Mol. Phys.*, 87:961–978, 1996.

[117] R. L. Kenion-Hanrath. *Toward Simulating Complex Systems with Quantum Effects*. PhD thesis, Cornell University, 2017.

[118] F. Pan and G. Tao. Communication: Importance sampling including path correlation in semiclassical initial value representation calculations for time correlation functions. *J. Chem. Phys.*, 138:091101, 2013.

[119] N. Makri and W. H. Miller. Monte carlo path integration for the real time propagator. *J. Chem. Phys.*, 89:2170–2177, 1988.

[120] B. W. Spath and W. H. Miller. Semiclassical calculation of cumulative reaction probabilities. *J. Chem. Phys.*, 104:95–99, 1996.

[121] B. W. Spath and W. H. Miller. Semiclassical calculation of franck-condon intensities for reactive systems. *Chem. Phys. Lett.*, 262:486–494, 1996.

[122] E. A. Coronado, J. Xing, and W. H. Miller. Ultrafast non-adiabatic dynamics of systems with multiple surface crossings: a test of the meyerâmiller hamiltonian with semiclassical initial value representation methods. *Chem. Phys. Lett.*, 349:521 – 529, 2001.

[123] M. Spanner, V. S. Batista, and P. Brumer. Is the filinov integral conditioning technique useful in semiclassical initial value representation methods? *J. Chem. Phys.*, 122:084111, 2005.

[124] R. Gelabert, X. Gimenez, M. Thoss, H. Wang, and W. H. Miller. A log-derivative formulation of the prefactor for the semiclassical herman-kluk propagator. *J. Phys. Chem. A*, 104:10321–10327, 2000.

[125] G. Di Liberto and M. Ceotto. The importance of the pre-exponential factor in semiclassical molecular dynamics. *J. Chem. Phys.*, 145:144107, 2016.

[126] I. R. Craig and D. E. Manolopoulos. Chemical reaction rates from ring polymer molecular dynamics. *J. Chem. Phys.*, 122:084106, 2005.

[127] W. H. Miller. Beyond transition-state theory: A rigorous quantum theory of chemical reaction rates. *Acc. Chem. Res.*, 26:174, 1993.

[128] M. Born and E. Oppenheimer. Zur quantentheorie der molekeln. *Ann. Phys.*, 84:457, 1927.

[129] J. C. Tully. Perspective: Nonadiabatic dynamics theory. *J. Chem. Phys.*, 137(22):22A301, 2012.

[130] G. A. Worth and L. S. Cederbaum. Beyond born-oppenheimer: Molecular dynamics though a conical intersection. *Annu. Rev. Phys. Chem.*, 55:127–158, 2004.

[131] H. B. Gray and J. R. Winkler. Long-range electron transfer. *Proc. Natl. Acad. Sci. U.S.A.*, 102(10):3534–3539, 2005.

[132] M. Topaler and N. Makri. Path integral calculation of quantum nonadiabatic rates in model condensed phase reactions. *J. Phys. Chem.*, 100(11):4430–4436, 1996.

[133] M. H. Beck, A. Jäckle, G. A. Worth, and H. D. Meyer. The multiconfiguration time-dependent hartree (mctdh) method: a highly efficient algorithm for propagating wavepackets. *Phys. Rep.*, 324(1):1–105, 1 2000.

[134] T. J. H. Hele and N. Ananth. Deriving the exact nonadiabatic quantum propagator in the mapping variable representation. *Faraday Discuss.*, 195:269–289, 2016.

[135] S. M. Greene and V. S. Batista. Tensor-train split-operator fourier transform (tt-soft) method: Multidimensional nonadiabatic quantum dynamics. *J. Chem. Theor. Comput.*, 13:4034–4042, 2017.

[136] S. J. Cotton and W. H. Miller. Classical molecular dynamics simulation of electronically non-adiabatic processes. *Faraday Discuss.*, 195:9, 2016.

[137] A. Donoso and C. C. Martens. Simulation of coherent nonadiabatic dynamics using classical trajectories. *J. Phys. Chem. A*, 102(23):4291–4300, 1998.

[138] R. Kapral. Progress in the theory of mixed progress in the theory of mixed quantum-classical dynamics. *Annu. Rev. Phys. Chem.*, 57:129–157, 2006.

[139] C. C. Martens. Nonadiabatic dynamics in the semiclassical liouville representation: Locality, transformation theory, and the energy budget. *Chem. Phys.*, 481:60–68, 2016.

[140] P. V. Parandekar and J. C. Tully. Detailed balance in ehrenfest mixed quantum-classical dynamics. *J. Chem. Theor. Comput.*, 2:229–235, 2006.

[141] J. C. Tully. Molecular dynamics with electronic transitions. *J. Chem. Phys.*, 93:1061–1071, 1990.

[142] O. V. Prezhdo and P. J. Rossky. Mean-field molecular dynamics with surface hopping. *J. Chem. Phys.*, 107(3):825–834, 1997.

[143] A. W. Jasper, S. N. Stechmann, and D. G. Truhlar. Fewest-switches with time uncertainty: A modified trajectory surface-hopping algorithm with better accuracy for classically forbidden electronic transitions. *J. Chem. Phys.*, 116(13):5424–5431, 2002.

[144] M. F. Herman. A semiclassical surface hopping propagator for nonadiabatic problems. *J. Chem. Phys.*, 103(18):8081–8097, 1995.

[145] Y. Wu and M. F. Herman. On the properties of a primitive semiclassical surface hopping propagator for nonadiabatic quantum dynamics. *J. Chem. Phys.*, 127:044109–1, 2007.

[146] B. R. Landry and J. E. Subotnik. How to recover marcus theory with fewest switches surface hopping: Add just a touch of decoherence. *J. Chem. Phys.*, 137:22A513, 2012.

[147] P. Huo and D. F. Coker. Communication: Partial linearized density matrix dynamics for dissipative, non-adiabatic quantum evolution. *J. Chem. Phys.*, 135:201101, 2011.

[148] P. Shushkov, R. Li, and J. C. Tully. Ring polymer molecular dynamics with surface hopping. *J. Chem. Phys.*, 137:22A549/1–22A549/13, 2012.

[149] N. Ananth. Mapping variable ring polymer molecular dynamics: A path-integral based method for nonadiabatic processes. *J. Chem. Phys.*, 139:124102, 2013.

[150] J. R. Duke and N. Ananth. Simulating excited state dynamics in systems with multiple avoided crossings using mapping variable ring polymer molecular dynamics. *J. Phys. Chem. Lett.*, 6:4219, 2015.

[151] J. R. Duke and N. Ananth. Mean field ring polymer molecular dynamics for electronically nonadiabatic reaction rates. *Faraday Discuss.*, 195:253, 2016.

[152] J-L Liao and G. A. Voth. A centroid molecular dynamics approach for nonadiabatic dynamical processes in condensed phases: the spin-boson case. *J. Phys. Chem. B*, 106(33):8449–8455, 2002.

[153] N. Ananth and T. F. Miller III. Exact quantum statistics for electronically nonadiabatic systems using continuous path variables. *J. Chem. Phys.*, 133:234103, 2010.

[154] W. H. Miller. Electronically nonadiabatic dynamics via semiclassical initial value methods. *J. Phys. Chem. A*, 113:1405–1415, 2009.

[155] G. Tao. Electronically nonadiabatic dynamics in complex molecular systems: An efficient and accurate semiclassical solution. *J. Phys. Chem. A*, 117:5821–5825, 2013.

[156] F. Agostini, S. K. Min, and E. K. U. Gross. Semiclassical analysis of the electron-nuclear coupling in electronic non-adiabatic processes. *Ann. Phys. (Berlin) 527*, 527:546–555, 2015.

[157] A. Kelly, R. van Zon, J. Schofield, and R. Kapral. Mapping quantum-classical liouville equation: Projectors and trajectories. *J. Chem. Phys.*, 136:084101, 2012.

[158] B. Leimkuhler and S. Reich. *Simulating Hamiltonian Dynamics*. Cambridge University Press, 2004.

[159] J. O. Richardson, P. Meyer, M.-O. Pleinert, and M. Thoss. An analysis of nonadiabatic ring-polymer molecular dynamics and its application to vibronic spectra. *Chem. Phys.*, 482:124–134, 2016.

[160] See https://github.com/ananthgroup/sc-ivr-code-package to access the open source program.

[161] Y. Huang, C. T. Rettner, D. J. Auerbach, and A. M. Wodtke. Vibrational promotion of electron transfer. *Science*, 290:111, 2000.

[162] E. Hasselbrink. How non-adiabatic are surface dynamical processes? *Curr. Opin. Solid State Mater. Sci.*, 10:192–204, 2006.

[163] N. Hendrik Nahler and A. M. Wodtke. Dynamics of molecule-induced electron emission from surfaces. *Mol. Phys.*, 106:2227–2244, 2008.

[164] I. Rahinov, R. Cooper, D. Matsiev, C. Bartels, D. J. Auerbach, and A. M. Wodtke. Quantifying the breakdown of the born-oppenheimer approximation in surface chemistry. *Phys. Chem. Chem. Phys.*, 13:12680–12692, 2011.

[165] C. Bartels, R. Cooper, D. J. Auerbach, and A. M. Wodtke. Energy transfer at metal surfaces: the need to go beyond the electronic friction picture. *Chem. Sci.*, 2:1647, 2011.

[166] J. LaRue, T. Schafer, D. Matsiev, L. Velarde, N. Hendrik Nahler, D. J. Auerbach, and A. M. Wodtke. Vibrationally promoted electron emission at a metal surface: electron kinetic energy distributions. *Phys. Chem. Chem. Phys.*, 13:97–99, 2011.

[167] J. L. LaRue, T. Schafer, D. Matsiev, L. Velarde, N. Hendrik Nahler, D. J. Auerbach, and A. M. Wodtke. Electron kinetic energies from vibrationally promoted surface exoemission: Evidence for a vibrationally autodetachment mechanism. *J. Phys. Chem. A*, 115:14306–14314, 2011.

[168] M. Head-Gordon and J. C. Tully. Molecular dynamics with electronic frictions. *J. Chem. Phys.*, 103:10137, 1995.

[169] S. Monturet and P. Saalfrank. Role of electronic friction during the scattering of vibrationally excited nitric oxide molecules from au(111). *Phys. Rev. B*, 82:075404, 2010.

[170] N. Shenvi, S. Roy, and J. C. Tully. Nonadiabatic dynamics at metal surfaces: Independent-electron surface hopping. *J. Chem. Phys.*, 130:174107, 2009.

[171] N. Shenvi, S. Roy, and J. C. Tully. Dynamical steering and electronic excitation in no scattering from a gold surface. *Science*, 326:829, 2009.

[172] S. Roy, N. Shenvi, and J. C. Tully. Model hamiltonian for the interaction of no with the au(111) surface. *J. Chem. Phys.*, 130:174716, 2009.

[173] E. G. Fuemmeler. *Quantum Mechanical Studies of Nonadiabatic Systems*. PhD thesis, Cornell University, 2018.

[174] D. M. Newns. Self-consistent model of hydrogen chemisorption. *Phys. Rev.*, 178(3):1123, 1969.

[175] S. Wouters, C. A. Jimenez-Hoyos, Q. Sun, and H. G.-L. Chan. A practical guide to density matrix embedding theory in quantum chemistry. *J. Chem. Theor. Comput.*, 12:2706–2719, 2016.